

**Numerical Simulation of Feedback Control of Aerodynamic
Configurations In Steady and Unsteady Ground Effects**

by

Abdullah O. Nuhait

Dissertation submitted to the Faculty of the
Virginia Polytechnic Institute and State University
In partial fulfillment of the requirements for the degree of

DOCTOR OF PHILOSOPHY

in

Engineering Mechanics

APPROVED:

Dean T. Mook, Chairman

Saad A. Ragab

Scott L. Hendricks

Demetri P. Telionis

John K. Shaw

October, 1988

Blacksburg, Virginia

**Numerical Simulation of Feedback Control of Aerodynamic
Configurations in Steady and Unsteady Ground Effects**

by

Abdullah O. Nuhait

Dean T. Mook, Chairman

Engineering Mechanics

(ABSTRACT)

A general numerical simulation of closely coupled lifting surfaces in steady and unsteady ground effects was developed. This model was coupled with the equations of motion to simulate aerodynamic-dynamic interaction. The resulting model was then coupled with a feedback-control law to form a general nonlinear unsteady numerical simulation of control of an aircraft in and out of ground effect.

The aerodynamic model is based on the general unsteady vortex-lattice method and the method of images. It is not restricted by planform, angle of attack, sink rate, dihedral angle, twist, camber, etc. as long as stall or vortex bursting does not occur. In addition, it has the versatility to model steady and unsteady aerodynamic interference. The present model can be used to simulate any prescribed flare and to model the effects of cross and/or head winds near the ground.

The present results show the influences of various parameters on the aerodynamic coefficients for both steady and unsteady flows. Generally, the ground increases the aerodynamic coefficients; the greater the sink rates, the stronger the effects. Increasing the aspect ratio increases both the steady and unsteady ground effects. An exception is a large aspect-ratio wing with large camber. The present results are generally in close agreement with limited exact solutions and experimental data.

In the aerodynamic-dynamic simulation, the equations of motion were solved by Hamming's predictor-corrector method. The aircraft, air stream, and control surfaces were treated as a single dynamic system. The entire set of governing equations was solved simultaneously and interactively. The aerodynamic-dynamic model was used to study a configuration that resembles a Cessna 182 airplane. The ground lowers the effectiveness of the tail in controlling pitch, increases the lift and drag, and makes the hinge-moment less negative. Proportional and rate control laws were used in a feedback system to control pitch. One set of gains was used in and out of ground effect. For the same control input, the pitch angle responds faster and overshoots more near the ground than it does far from the ground. The present results demonstrate the feasibility of using the current simulation to model more complicated motions and the importance of including the unsteady ground effects when analyzing the performance of an airplane during a landing maneuver.

Acknowledgements

I wish to express my gratitude and appreciation to my advisor Dr. Dean T. Mook for his advice, guidance, patience, understanding and encouragement throughout the development of this dissertation. I would like to thank Drs. Saad A. Ragab, Scott L. Hendricks, Demetri P. Telionis and John K. Shaw for spending their valuable time in reading this manuscript. Also, I wish to thank Dr. Frederick H. Lutze, Jr. for his help and guidance in the numerical simulation of the feedback control.

I wish to express my deep appreciation to my wife Hessa O. Almedlej and to my children Norah, Hend and Muhammad for their patience, understanding encouragement and love. Also, I wish to express my gratitude to my parents Othman and Munir-ah, to my brothers and to my sisters for their love and support.

Last but not least, I would like to express my appreciation to the Kingdom of Saudi Arabia in general and King Saud University in particular for giving me the opportunity to pursue my higher education. Without their support, this work would not have been possible.

Table of Contents

Introduction	1
1.1 General	1
1.2 Literature Review	2
1.2.1 Steady Ground Effect	2
1.2.2 Unsteady Ground Effect	11
1.2.3 Feedback Control	12
1.3 Motivation For Present Work	13
1.4 Objectives	14
Description of the Numerical Model of the Flowfield	16
2.1 General	16
2.2 Coordinate systems	18
2.3 The General Unsteady Vortex-Lattice Method	24
2.4 Computation of the Aerodynamic Loads	43
2.5 Computation Procedure	55
2.5.1 Unsteady Ground Effect	55
2.5.2 Velocity of Wind	56

2.5.3 Flight Path	57
Numerical Examples	63
3.1 General	63
3.2 Two-Dimensional Airfoils	65
3.3 Wake Plots	68
3.4 Tapered Wing	73
3.5 Flat Rectangular Wings	76
3.6 Rectangular Wings with Dihedral Angles	80
3.7 Swept Wings	83
3.8 Delta Wings	87
3.9 Wind Effect	95
3.10 Flight-Path Effect	101
3.11 Concluding Remarks	105
Dynamics and Control	106
4.1 General	106
4.2 Coordinate System	107
4.3 Dynamics	111
4.3.1 Equations of Motion	111
4.3.2 Method of Solution	113
4.3.3 Aerodynamic-Dynamic model	125
4.3.4 Numerical Examples	125
4.4 Feedback Control	136
Conclusions and Recommendations	152
References	155

Orientation of the Lifting Surface	159
Velocity Induced by a Straight Vortex Segment	167
Vita	173

List of Illustrations

Figure 1.	A wing, its wake, and their images near the ground	17
Figure 2.	The two coordinate systems	18
Figure 3.	Wing orientation	19
Figure 4.	A typical rectangular and leading-edge elements.	26
Figure 5.	Velocity field due to a finite strength vortex filament.	27
Figure 6.	A vortex segment and its image to the left of the x-z plane.	31
Figure 7.	A vortex segment and its image below the ground plane.	33
Figure 8.	A vortex segment and its three images for the symmetric case.	35
Figure 9.	Circulation around the closed loops and individual vortex segments of delta wing	40
Figure 10.	An actual computed wake of a delta wing near the ground	43
Figure 11.	Two-dimensional discrete point vortices.	47
Figure 12.	A rectangular and leading-edge elements of a delta wing for pressure calculations.	49
Figure 13.	A grid used to compute pressure jumps across a rectangular wing of unit aspect ratio.	52
Figure 14.	Pressure jumps across a rectangular wing of unit aspect ratio for steady flow	53
Figure 15.	A side view of a wing and its image near the ground.	56
Figure 16.	A sinusoidal flight path.	57
Figure 17.	A parabolic flight path.	59

Figure 18. A circular-arc flight path.	61
Figure 19. A two-dimensional flat plate wing in a steady ground effect	66
Figure 20. A two-dimensional circular-arc airfoil (camber = 0.022) in a steady ground effect	66
Figure 21. A two-dimensional circular-arc airfoil (camber = 0.053) in a steady ground effect	67
Figure 22. A two-dimensional circular-arc airfoil (camber = 0.097) in a steady ground effect	67
Figure 23. Actual computed wakes for a low-aspect-ratio tapered wing (AR = 1.9) in and out of ground effect for steady flow	69
Figure 24. Actual computed wakes for a low-aspect-ratio tapered wing (AR = 3.8) in and out of ground effect for steady flow	70
Figure 25. Actual computed wakes for a delta wing (AR = 1.5) in and out of ground effect for steady flow	71
Figure 26. Dimension of the model of an F-104A wing	73
Figure 27. A comparison of the computed and experimental results in steady flow for an F-104A wing	74
Figure 28. Computed results for a rectangular wing of unit aspect ratio in ground effect	77
Figure 29. Computed results for a rectangular wing of unit aspect ratio in ground effect	78
Figure 30. Computed results for a rectangular wing of unit aspect ratio in ground effect	79
Figure 31. Computed results for a rectangular wing of aspect ratio 4 in ground effect	81
Figure 32. Computed results for a rectangular wing of aspect ratio 4 in ground effect for unsteady flow	82
Figure 33. Computed results for a swept wing of aspect ratio 4 in ground effect	84
Figure 34. Computed results for a swept wing of aspect ratio 4 in ground effect for steady flow	85
Figure 35. Computed results for a swept wing of aspect ratio 4 in ground effect for unsteady flow	86

Figure 36. Numerical and experimental results for a thin flat delta wing (AR = 1.5) out of ground effect for steady flow	88
Figure 37. Numerical and experimental results for a thin flat delta wing (AR = 1.5) in ground effect for steady flow	89
Figure 38. A comparison of the computed and experimental results for delta wing (AR = 1.5) in steady ground effect	91
Figure 39. A comparison of the computed and experimental results for delta wing (AR = 1.5) in steady ground effect	91
Figure 40. A comparison of the computed and experimental results for delta wing (AR = 1.5) in unsteady ground effect	92
Figure 41. Computed results for a delta wing of aspect ratio 1.5 in ground effect	93
Figure 42. Computed results for delta wings in ground effect for unsteady flow	94
Figure 43. Computed results for a rectangular wing of aspect ratio 1 in ground effect with cross and head winds for steady flow	96
Figure 44. Computed results for a rectangular wing of aspect ratio 1 in ground effect with head wind	97
Figure 45. Computed results for a rectangular wing of aspect ratio 1 in ground effect with head wind	98
Figure 46. Computed results for a rectangular wing of aspect ratio 1 in ground effect with cross and head winds	99
Figure 47. Computed results for a rectangular wing of aspect ratio 1 in ground effect with cross wind	100
Figure 48. Computed results for a rectangular wing (AR = 1) flying along a sinusoidal flight path in and out of ground effects	102
Figure 49. Computed results for a rectangular wing (AR = 1) flying along a sinusoidal flight path in and out of ground effects	103
Figure 50. Computed results for a rectangular wing (AR = 1) flying along a sinusoidal flight path in and out of ground effects	103
Figure 51. Computed results for a rectangular wing (AR = 1) flying along a parabolic flight path in and out of ground effects	104
Figure 52. Computed results for a rectangular wing (AR = 1) flying along a circular flight path in and out of ground effects	104
Figure 53. Coordinate systems of the wing and control surface.	107

Figure 54. Actual computed wakes for a wing and tail configuration	110
Figure 55. Flow Chart for the First-Predictor-Corrector Method	117
Figure 56. Flow chart for the general-predictor-corrector method	124
Figure 57. Aerodynamic characteristic at trim in and out of ground effect for steady flows	129
Figure 58. Pitch change out of ground effect	130
Figure 59. Pitch change in ground effect	132
Figure 60. Pitch change in ground effect	134
Figure 61. Pitch change out of ground effect for various gains of the feedback-control system	142
Figure 62. Pitch change with feedback control out of ground effect	144
Figure 63. Pitch change with feedback control out of ground effect	146
Figure 64. Pitch change with feedback control in ground effect	148
Figure 65. Pitch change with feedback control in ground effect	150

List of Tables

Table 1. Physical quantities used for the simulation of Cessna 182 airplane taken from Smetana (1984). 126

Table 2. The stability derivatives 139

Nomenclature

- A** = the area of an element
- A_{ij}** = the matrix of influence coefficients, the normal component of the velocity induced at the control point of element i by a unit-circulation vortex loop around element j
- AR** = the aspect-ratio, $\frac{b^2}{area}$
- b** = the span
- C** = the root chord
- C_D** = the drag coefficient in ground effect
- C_{D_∞}** = the drag coefficient out of ground effect
- C_h** = the hinge-moment coefficient
- C_L** = the lift coefficient in ground effect
- C_{L_∞}** = lift coefficient out of ground effect
- C_M** = the pitching-moment coefficient in ground effect
- C_{M_∞}** = pitching-moment coefficient out of ground effect
- $C_{M\theta}$** = the derivative of the pitching-moment coefficient with respect to the pitch angle

$C_{M\dot{\theta}}$	= the derivative of the pitching-moment coefficient with respect to the pitch rate
$C_{M\delta}$	= the derivative of the pitching-moment coefficient with respect to the tail deflection angle
C_R	= the rolling-moment coefficient in ground effect
$C_{R\infty}$	= the rolling-moment coefficient out of ground effect
C_Y	= the side-force coefficient in ground effect
$C_{Y\infty}$	= the side-force coefficient out of ground effect
C_n	= the normal-force coefficient
C_p	= the pressure coefficient
ΔC_p	= the pressure jump across the lifting surface
G	= the circulation of each vortex ring
H	= the height of the trailing edge above the ground
L	= the physical length of the chordwise increment of the bound lattice
\vec{n}	= a unit vector normal to the lifting surface
P	= the pressure
\vec{r}	= the position vector of any point in space relative to the B-F frame
\vec{R}	= the position vector of any point in space relative to the G-F frame
\vec{R}_A	= the position vector of the origin of the B-F frame relative to the G-F frame
t	= the time, dimensionless
Δt	= the time increment, dimensionless
U	= the characteristic speed of the wing
\vec{v}	= the velocity of any point in space relative to the B-F frame
\vec{V}	= the velocity of any point in space relative to the G-F frame
\vec{V}_A	= the dimensionless velocity of the origin of the B-F frame, its magnitude is one

V_{Ax}	= the X-component of the velocity of the origin of the B-F frame, $\cos \gamma$
V_{Az}	= the Z-component of the velocity of the origin of the B-F frame, $\sin \gamma$
$\vec{V}_{LS,i}$	= the velocity of point i on the lifting surface
$\vec{V}_{m,i}$	= the mean velocity of the fluid at point i on the lifting surface
\vec{V}_{wind}	= the velocity of the cross and/or head wind
$\Delta \vec{V}_i$	= the velocity jump of the fluid across the lifting surface at point i
x,y,z	= the body-fixed coordinates, (B-F)
X,Y,Z	= the ground-fixed coordinates, (G-F)
α	= the angle of attack, degrees, $\gamma + \theta$
β	= the leading-edge sweep-back angle, degrees
δ	= the control-surface deflection angle, degrees
η	= the angle which the velocity of the wind makes with the X-axis in the X-Y plane, degrees
γ	= the flight-path angle, degrees
Γ	= the dihedral angle, degrees
Γ	= the circulation of a straight vortex segment
$\vec{\omega}$	= the angular velocity of the wing
ϕ	= the roll angle, degrees
ϕ	= the velocity potential in terms of the B-F frame
Φ	= the velocity potential in terms of the G-F frame
ψ	= the yaw angle, degrees
θ	= the pitch angle, degrees

Chapter I

Introduction

1.1 General

During take-off and landing, the aerodynamic characteristics of an airplane are influenced by the proximity of the ground. This phenomenon is called ground effect. Because landing and take-off are critical phases in a flight, extensive research, both theoretical and experimental, has been devoted to understanding and predicting ground effect. The ultimate goal is to develop a model that can simulate control of an aircraft in ground effect. The first part of the research described here deals with the development of a general numerical simulation of configurations of lifting surfaces in steady and unsteady ground effects. The second part deals with the development of a general numerical simulation of a feedback-control system for wings in ground effect.

1.2 Literature Review

1.2.1 Steady Ground Effect

Apparently, the first basic theory was developed by Wieselsberger (1922). Wieselsberger modeled the ground effect by placing the image of the real wing below the ground plane and thereby making the ground a plane of symmetry. Then he used the lifting-line theory of Prandtl and the basic concepts of the induced drag of multiplane configurations to calculate a correction. The correction was used to modify the classical induced drag and induced angle of attack of wings out of ground effect. Wieselsberger assumed an elliptical lift distribution over the wing span. The trailing vortices were placed parallel to the flight path. Wieselsberger considered only the effect of the trailing vortices of the image wing in calculating the downwash on the real wing. He ignored the effect of the bound vortices of the image wing in reducing the longitudinal velocity at the real wing and in changing the circulation around the real wing. As a result, the theory is limited to thin wings of large aspect ratios at small angles of attack, with small sweep-back angles and at relatively high distances above the ground. The predicted trend of decreasing induced drag at constant lift of wings is in general agreement with experimental and flight tests conducted by Reid (1927), Tonnes (1932), Wetmore and Turner (1940), Fink and Lastinger (1961), and Carter (1961).

Rosenhead (1931) solved the problem of a flat plate of infinite span between parallel walls using a conformal transformation. He showed that the effect of walls is to increase the lift and that the solution of the problem of a flat plate in the

neighborhood of a single wall can be obtained from the general result by a suitable limiting process. The procedure, however, seems to be complicated. Tomotika et al. (1933) found the exact solution for a two-dimensional flat plate in the presence of a single wall by a conformal transformation similar to the one employed by Rosenhead. They found that, as the distance above the ground decreases, the lift first decreases and then increases in comparison to the lift in an unlimited medium. Pistoiesi (1935) made an interesting survey of the early theoretical and experimental work on ground effect.

Further research was done by Tani et al. (1937a,1937b) after recognizing the weakness of Wieselsberger's theory. As Wieselsberger had done, they placed an image of the real wing below the ground plane, used lifting-line theory with an elliptical lift distribution over the span, and assumed the trailing vortices were parallel to the flight path. They considered the effect of the bound vortices of the image wing in reducing the longitudinal velocity at the real wing and in changing the circulation around the real wing as well as the effect of the image trailing vortices in reducing the downwash on the real wing. They also considered the effect of thickness. These factors were incorporated into two simple equations. The influence of the ground effect on the induced angle of attack and induced drag at constant lift is given by these equations. It is clear that the theory of Tani et al. is an extension of the theory of Wieselsberger; however, the theory is still limited to wings of large aspect ratios with small sweep-back angles at small angles of attack.

Havelock (1938) obtained the exact solution for an elliptical cylinder between two parallel walls by using a conformal-mapping technique. A flat plate was treated as the limiting case. The flat plate in the neighborhood of a single wall was derived from the general solution by a limiting process. His solution for the lift of the flat plate in

the neighborhood of a single wall matches the solution of Tomotika et al. far from the ground.

Green (1940) solved for the lift and pitching moment for a circular-arc airfoil in the presence of a plane wall by using a conformal transformation. He concluded that the lift and moment coefficients are probably always decreased by the presence of the wall for all values of the angle of attack. Further, Green(1946) investigated the manner in which the ground effect influences the lift and pitching moment of two-dimensional airfoils by using a conformal-mapping technique. He concluded that for small angles of attack the effects of camber are to decrease the lift as the ground is approached. Moreover, the effects of thickness are first to decrease and then to increase the lift as the ground is approached. That is the thickness and camber work mainly in opposite directions so that the flat plate might be expected to give a reasonable approximation to actual cases.

Tomotika et al. (1951a) investigated the ground effect on the lift of Joukowski-type airfoil, by using a conformal-mapping technique. They found that the lift usually was increased by the presence of the ground, but the rate of increase becomes smaller as the thickness of the airfoil increases. Further, Tomotika et al. (1951b) studied the lift and pitching moment of a two-dimensional circular-arc airfoil in stream bounded by a plane wall by employing a conformal-mapping technique. They concluded that, when the camber and angle of attack are sufficiently small, the lift and pitching moment coefficients first decrease and then increase as the ground is approached, which is in contradiction to Green (1940, 1946). For greater values of the camber, they found that the lift and pitching moments decrease for all values of angle of attack. Clearly, the effect due to the thickness acts in the same direction as the effect due to camber, which is in contradiction to Green (1946).

Licher (1956) recognized the shortcomings of the theory of Tani et al. for wings of moderate aspect ratio with large sweep-back angles, with flaps, and at small distances above the ground. He developed a method of representing the wing by a number of horseshoe vortices distributed over the wing. He placed all the horseshoe vortices on the mean horizontal projection of the wing rather than on the actual inclined or camber line. As a result, the method is limited to small angles of attack. The method underestimated the induced drag when compared to the induced drag of an elliptical wing out of ground effect. As a result, the method cannot be used to compute the drag accurately. In addition, the method cannot be used to predict the pitching moment. The predicted ground effect increases the lift for rectangular wings at moderate angles of attack.

Buell and Tinling (1957) conducted wind-tunnel tests for two models of wings having low aspect ratio and pointed tips. They found that the ground increases the slope of the lift curve and decreases the induced drag. Moreover, the pitching moments for both models become more negative (i.e., pitch-down moment increases). The theory of Tani et al. underpredicted the ground effect for both models.

Kohlman and Glett (1958) developed a numerical method that imitates a wing with flaps and its image by a series of bound and trailing vortices. The bound vortices were distributed trigonometrically over the span. They thought of the wing as composed of two type of sections; one that did not contain the flap and another that contained the flap. They placed each bound vortex at the quarter-chord position on the wing section that did not contain the flap. On the wing section that contained the flap, they placed each bound vortex at the half-chord position. Then, they placed the first bound vortex outboard of the flap at the three-eighth-chord position. Then,

they placed the second bound vortex outboard of the flap at the quarter-chord position and so on. The trailing vortices consisted of three parts:

1. Those started from the bound vortex and ended at the leading-edge of the flap.
2. Those started from the leading-edge of the flap and ended at the trailing-edge of the flap.
3. Those started at the trailing-edge of the flap and extended to infinity parallel to the ground.

Then they computed the velocity induced by the image vortices at two chordwise locations for each of the real bound vortices. The first point was at the position of the bound vortex and the second point was at one half chord behind the first point. At the first point they computed the longitudinal velocity and at the second point they computed the vertical velocity due to the influence of the ground. They used the effects of these factors to modify the spanwise loading coefficient of a wing out of ground effect. The ground effects in general are first favorable and then unfavorable as the wing approaches the ground. Moreover, with increasing flap deflection, the effects become less favorable.

Thomas (1960) employed a method based on the extended lifting-line theory to investigate the ground effect on swept and delta wings. He concluded that the ground effects cause an increase in the slope of the lift, the maximum lift and the flap effectiveness, a decrease in the induced drag, and a small rearward movement of the aerodynamic center (i.e., increase in the pitch-down moment). However, the agreement between the theoretical and experimental results at small heights was poor. Thomas thought that this discrepancy resulted from distributing the vorticity

along a line, not over the complete surface, and from assuming the wing to be parallel to the ground.

Bagley (1961) developed a method for calculating the pressure distribution on two-dimensional airfoils of arbitrary section at moderate heights. It is an extension of Tani's method (1932). The thickness and lifting problems were represented by distributions of sources and vortices, respectively. The ground effects were reproduced by considering the influence of the images of these singularities and an additional vortex distribution. These singularities were placed on two lines parallel to the ground plane rather than on the actual camber line and its image. As a result, the method is restricted to small angles of attack.

Choliasmeons (1962) replaced a wing with an elliptical lift distribution by an equivalent-lift horseshoe-vortex system having the same value of circulation about its trailing vortices as that presented on the wing mid-span. The trailing vortices were assumed to be a straight horizontal lines and they were separated by $\frac{\pi}{4}$ times the wing span. The bound vortex was placed at the one quarter of the chord position over the new span. The effects of the image vortices were computed at the three quarter-chord position at mid-span. Choliasmeons conducted wind-tunnel tests on a straight thick rectangular wing equipped with a slat, flap, and boundary-layer control. The agreement between theoretical and experimental results was poor. The ground effect in general is favorable for a wing with low circulation and it is unfavorable for a wing with high circulation.

Saunders (1963,1965) employed a lifting-surface theory with the method of images to study the ground effect on wings of finite span. The technique is limited to small angles of attack. Saunders compared computed lift-slope coefficients to the data of Carter (1961) and Fink and Lastinger (1961). The agreement was good for the case of a rectangular wing of aspect ratio two. It was poor for rectangular wings of

aspect ratios 1 and 4, although the trends are the same. There is an increase in the lift-slope coefficients and a rearward movement of the center of pressure (i.e., a more nose-down pitching moment) as the ground was approached.

Rolls and Koenig (1966) conducted flight tests on an aircraft with a low-aspect-ratio wing at various fixed heights above the ground. They found a definite increase in lift and in the nose-down pitching moment.

Abercrombie (1967) used an extended lifting-line theory with techniques similar to the method of Choliasmenos. The rolled-up vortices were assumed to lie parallel to each other and to the ground. The trailing vortices were assumed to extend from the trailing-edge of the wing, not from the lifting line. An elliptical lift distribution was assumed near the ground. The bound vortex was placed at the quarter-chord position along the span. The effects of the images vortices were computed at the three-quarter-chord position of the mid-span. Abercrombie compared his theoretical results to the wind-tunnel tests of Choliasmeons(1962) and Fink and Lastinger(1961). The agreement was fair. The ground effect increases the lift for wings with small circulation and decreases the lift for wings with large circulation.

Fox (1969a,1969b) employed a method based on a combination of the vortex-lattice method and the leading-edge-suction analogy to determine the influence of the ground on delta wings. The technique is not capable of predicting the load distribution over the wing; consequently it cannot predict the pitching moment. The trailing vortices were assumed to be parallel to the plane of the wing and hence for positive angles of attack intercepted the ground plane and passed into the image region. Similarly, The trailing vortices of the image intercepted the ground plane and passed into the real region. These will create some errors particularly if downwash on a rear tail is computed. As a result, the technique cannot be used to investigate interference among multiple closely coupled lifting surfaces. The technique used to

form the image depends on the assumption that the wing is planar; hence the image system would be incorrect if the wing were nonplanar. Fox cited some experimental data that are not available any more. The agreement between the computed and experimental results was fair, in general, for wings with unit aspect ratios and poor for wings with aspect ratios greater than two; but the trends were the same. The model predicts an increase in the lift coefficients and a decrease in the induced drag as the ground is approached.

Baker et al. (1970) conducted flight tests on several aircraft with low-aspect-ratio wings at constant angles of attack. The ground effects caused significant changes in the lift, drag, and pitching-moment coefficients when the tested aircraft approached the ground.

Maskew (1971) used an extension of the vortex-lattice method that includes a vortex wake to model the ground effect on a swept flapped wing with aspect-ratio 4. He replaced the wing and its wake by a distribution of quadrilateral vortex rings. The method of images was used to represent the ground effect. Maskew assumed, initially, that the wake is straight and parallel to the ground and solved for the vortex strength over the wing. Then, he relaxed the trailing vortices using this solution, starting at the tip and working inboard. A second solution for the vortex strength was found after all the wake was relaxed. The procedure was continued until the wake converged. Maskew claims that there was little change in the wake shape and in the aerodynamic loads after two iterations. He concluded that a wing (and in particular a swept wing) with a large camber at constant incidence can actually lose lift near the ground and that the ground effect reduces the induced drag. Maskew obtained a forward movement of the center of pressure (i.e., pitch-up moment) for wings with large cambers in the ground effect.

Gratzer and Mahal (1972) discussed and compared theoretical and experimental results. A vortex-lattice method was used to compute the influence of the ground on a finite wing. The method ignored some of the complexities of the flow such as the roll-up of the wake. The wing and its image were replaced by a system of horseshoe vortex singularities. They used this model to compute aerodynamic coefficients of a flapped wing. The flap deflection was 50 degrees. They compared their computed lift coefficient with wind-tunnel data for STOL models. The agreement was good. The ground effect is unfavorable as the wing approaches the ground. The downwash angle is reduced at the tail position as the ground is approached.

Kobayakawa and Maeda (1978) investigated the gust response of thin flat wings passing through a vertical-gust pattern near the ground using lifting-surface theory for theoretical computation and a wind tunnel for testing. The theoretical computation was based on a sinusoidal gust. They neglected the effect of the shear flow and the oscillation of the wing. In addition, they assumed the wing was parallel with the ground and they replaced the downwash on the wing by the gust velocity. They compared the computed results to the wind-tunnel data. The agreement was fair.

Plotkin and Kennel (1981) used the higher-order thin-wing theory of Van Dyke to obtain effect of thickness on a two-dimensional airfoil near the ground. The effect of thickness decreases the lift force as the airfoil approaches the ground which is in contradiction to both Green and Tomotika et al.

Katz and Levin (1984) conducted wind-tunnel tests on a thin delta wing using the ground board method. They observed that the lift increases and the pitching moment becomes more negative as the ground is approached.

Tan and Plotkin (1986) developed an approximate solution of the problem of a thin wing in ground effect using lifting-line theory. The solution is valid for large aspect-ratio wings at large distances above the ground. The ground effect increases

the lift-slope coefficients and decreases the lift coefficients versus thickness as the ground is approached.

Er-EI and Weihs (1986) conducted wind-tunnel tests on delta wings. The overall result is an increase of the normal force and nose-down pitching moment.

1.2.2 Unsteady Ground Effect

As mentioned earlier Wieselsberger was the first to replace the ground with the image of the wing. Since then, almost all theoretical investigators have employed image techniques to simulate the ground effect with the wing height fixed in time (a situation which may be called steady ground effect) and the wake position assigned. This model has two shortcomings. First the wake position cannot be assigned because the wake deforms and rolls up into the force-free position, which must be calculated as part of the solution, and second the flow is not steady because during take off and landing the height changes with time. Indeed, for some military applications the height changes rapidly. Recently, Chen and Schweikhard (1985) solved for the unsteady ground effect in the case of a two-dimensional flat plate, assuming the wake to be straight along the flight path. They found that the increases in lift due to the unsteady ground effect are greater than those due to the steady ground effect for intermediate heights above the ground. They speculated that a similar trend of lift variations is to be obtained in the case of a finite wing in unsteady ground effect.

Steven (1985) studied the ground effect on a power-lift-STOL aircraft during landing phases. He presented a technique to separate the influence of the ground effect from the influence of other effects, namely, the pilot inputs control and

atmospheric effects on airplane dynamics during a landing approach. Steven assumed that at a height greater than the airplane wing span, the airplane was out of the ground effect. The proximity of the ground increases the lift (which in turn reduces the sink rate) even while landing at high lift coefficient, reduces the induced drag, and makes more nose down pitching moment.

Chang(1985) and Chang and Muirhead (1985,1987) tested several thin flat delta wings in both steady and unsteady ground effects. The proximity of the ground increases the aerodynamic coefficients; but in contrast to Chen and Schweikhard, these effects are weakened by the unsteadiness.

Katz (1986) used a vortex-lattice method that included a freely-deforming wake to investigate the performance of a lifting surface close to the ground as found on racing cars. Katz found that the increases in aerodynamic loads due to the unsteady ground effect are about 100 percent greater than those of the steady ground effect.

1.2.3 Feedback Control

The ultimate goal for both military and commercial aviation is all weather operation (Blakelock, 1965). This, of course, includes the possibility of landing an aircraft without visual reference to the runway. The previous work on the feedback control of an aircraft during a landing maneuver is based on the quasisteady flow and linearity assumptions and does not include the ground effect (Blakelock, 1965; Etkin, 1982; McRuer et al., 1973). Recently, Mracek (1988) developed a general, nonlinear and unsteady numerical simulation of a feedback-control system for wings out of ground effect. The model was based on coupling a vortex-panel method with the equations of motion and the resulting model was then coupled with a

feedback-control law. Mracek used his model to control the wing-rock phenomenon. Vinh et al. (1988) developed a technique to model a feedback control for trim at transonic speed. To the best of our knowledge, there has been no contribution in the unsteady and nonlinear feedback control of an aircraft near the ground. Therefore, the need for research in this field is obvious.

1.3 Motivation For Present Work

Steven (1985) reported that ground effects have a strong influence on aircraft landing performance; therefore the influence of the ground must be taken into account when calculating aircraft performance and stability and control characteristics. But exact solutions are difficult to obtain for two-dimensional airfoils with arbitrary camber (or flaps) and most-likely impossible to obtain for three-dimensional wings (Licher, 1956). Moreover, experimental work on models is very difficult and expensive in ground effect (Tuck,1978). Futhermore, the influence of the ground on a small model may not be generalized to large airplanes (Kemp et al., 1966). Consequently, it is very desirable to develop theoretical models and numerical simulations to predict the effect of the ground on an airplane. The accuracy of the numerical models can be checked by comparing the results they predict to the limited available exact solutions or/and experimental results.

Because landing and take-off can be simulated properly only by including the unsteady ground effect, as mentioned earlier, because there is a lack of theories for the unsteady ground effect, which is not yet fully understood, and because, apparently, there is no analysis which includes the unsteady ground effect and

nonlinear feedback control of an aircraft near the ground, we have undertaken the task of developing a general unsteady numerical simulation that accurately predicts and explains this phenomenon. In addition, the model should have the built-in versatility needed to simulate steady and unsteady aerodynamic interference among multiple closely coupled lifting surfaces. It should not be restricted by planform, angle of attack, sink rate, dihedral angle, twist, etc. as long as stall does not occur.

1.4 Objectives

The objectives of this research are to investigate the influence of the ground on an airplane during take-off and landing maneuvers, and to develop a numerical simulation of a feedback-control system that can be used to maneuver an airplane near the ground. Specifically, the objectives of research are sixfold:

1. Most, if not all, of the lift is generated by the wing of an airplane. As a result, a simple model of an airplane is its wing. A single lifting surface will be studied in both steady and unsteady ground effects for several planforms, dihedral angles, sweep-back angles, etc.
2. The pitch of an airplane is controlled by its horizontal tail and/or canard. As a result, the interference between two lifting surfaces will be investigated in ground effect.

3. An airplane during take-off and landing maneuvers is sometimes faced with cross wind. For this reason, the effect of cross wind on a single lifting surface near the ground will be investigated.
4. The flight path of an airplane during a landing approach is not always straight. Accordingly, both forward and vertical velocities are changing, so that the effect of the flight path on the aerodynamic characteristics of a single lifting surface will be studied.
5. During a landing approach, the control surfaces of an airplane are rotated so that the airplane may follow a specified flight path. This is usually accomplished by the use of feedback control. Consequently, a general, nonlinear and unsteady numerical simulation of a feedback-control system will be developed that can be used as a building block for achieving the goal of controlling an aircraft during landing maneuvers.
6. Finally, all the developments in 1 to 5 above will be incorporated into a single general numerical method for both steady and unsteady ground effects.

The aerodynamic model used in this study is an extension of the general unsteady subsonic vortex-lattice method of Konstadinopoulos et al. (1985). The method is fully described in chapter two. In chapter three, examples of aerodynamic simulation are given. Dynamics and control are described in chapter four. Finally, conclusions and recommendations are presented in chapter five.

Chapter II

Description of the Numerical Model of the Flowfield

2.1 General

The ground effects are simulated by the method of images. The images of the real wing and its wake are placed below the ground plane, as shown in figure 1. The concept of the present development is one of a wing moving through air instead of air blowing over a wing. The problem is posed in terms of two reference frames: one is fixed to the ground, the Ground-Fixed (G-F) frame, and the other is fixed to the wing, the Body-Fixed (B-F) frame, as shown in figure 2. A full discussion of the two systems is given in section 2.2 before introducing the general unsteady vortex-lattice method. In section 2.3, the general unsteady vortex-lattice method is introduced. Computation of the aerodynamic loads is described in section 2.4. In section 2.5, the computation procedure is described.

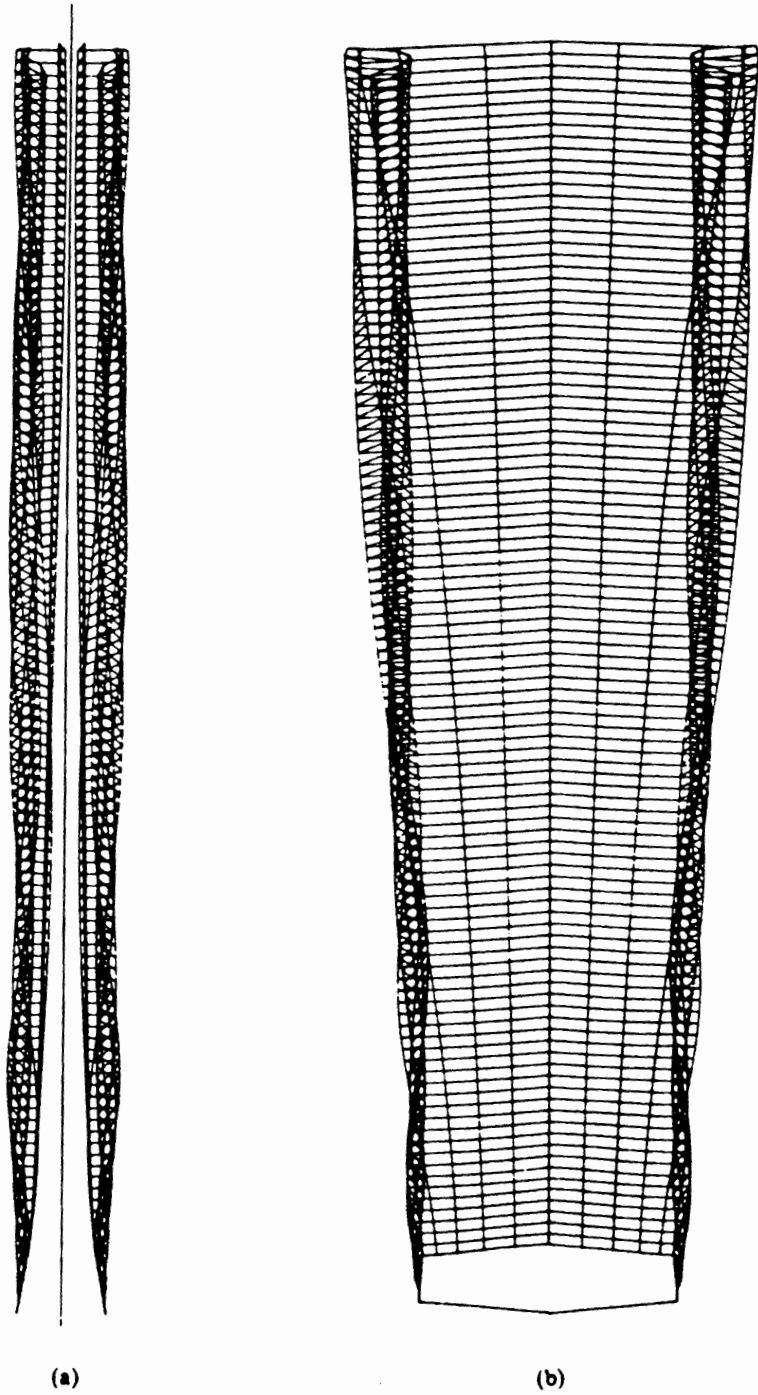
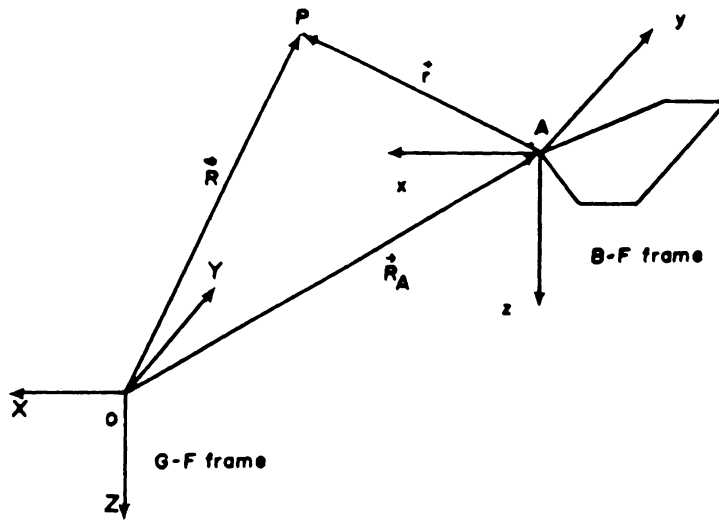


Figure 1. A wing, its wake, and their images near the ground: (a) side view and (b) top view.



P is an arbitrary point in space

Figure 2. The two coordinate systems: Ground-Fixed (G-F) Frame and Body-Fixed (B-F) Frame.

2.2 Coordinate systems

We follow the standard practice for orienting the axes; see for example Etkin (1982) and Schliching and Truckenbrodt (1979). The axes of the G-F frame are denoted by X,Y,Z and those of the B-F frame are denoted by x,y,z. Both coordinate systems are right-handed. The x- and y-axes lie on the plane of the planform, while the z-axis is normal to the wing and points downward. The x-axis points forward along the chord of the wing. The X- and Y-axes lie on the plane of the ground, while the Z-axis is normal to the ground and points downward. The X-axis points forward. The unit vectors of the B-F and G-F systems are denoted by $(\vec{i}, \vec{j}, \vec{k})$ and $(\vec{I}, \vec{J}, \vec{K})$, respectively. The two frames are related through the 3-2-1 set of rotations for Euler angles.

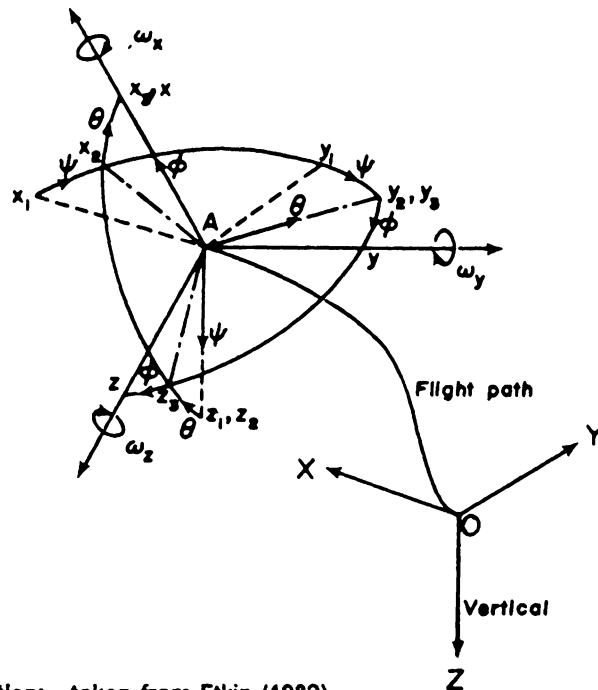


Figure 3. Wing orientation: taken from Etkin (1982).

In order to derive the relationship between the two frames, we assume that the x -, y -, and z -axes are initially parallel with the X -, Y -, and Z -axes, respectively. The B-F frame is in the position $Ax_1y_1z_1$, as shown in figure 3 (taken from Etkin, 1982). Then we follow the B-F frame as it assumes different orientations in space, as shown in figure 3, resulted from a sequence of orientations about the axes in the following order:

1. First, a yaw-like rotation $\psi(t)$ about the z_1 -axis.
2. Then, a pitch-like rotation $\theta(t)$ about the y_2 -axis.
3. Then, a roll-like rotation $\phi(t)$ about the x_3 -axis.

The transformation from the unit vectors of the G-F frame ($\vec{i}, \vec{j}, \vec{k}$) to those of the B-F frame ($\vec{i}, \vec{j}, \vec{k}$) (see appendix A) is given by the following:

$$\begin{bmatrix} \vec{i} \\ \vec{j} \\ \vec{k} \end{bmatrix} = [R_1(\phi)][R_2(\theta)][R_3(\psi)] \begin{bmatrix} \vec{i} \\ \vec{j} \\ \vec{k} \end{bmatrix}$$

which can be written simply,

$$\begin{bmatrix} \vec{i} \\ \vec{j} \\ \vec{k} \end{bmatrix} = [R] \begin{bmatrix} \vec{i} \\ \vec{j} \\ \vec{k} \end{bmatrix} \quad (2.2 - 1)$$

where $[R_1(\phi)]$, $[R_2(\theta)]$, and $[R_3(\psi)]$ are rotation matrices. For example, $[R_3(\psi)]$ represents the rotation of a system of axes originally coincident with axes X,Y,Z by an angle ψ about an axis that is parallel to Z (see appendix A for more detail). $[R]$ represents the triple product of the rotation matrices and it is simply

$$[R] = \begin{bmatrix} c\theta c\psi & c\theta s\psi & -s\theta \\ s\phi s\theta c\psi - c\phi s\psi & s\phi s\theta s\psi + c\phi c\psi & s\phi c\theta \\ c\phi s\theta c\psi + s\phi s\psi & c\phi s\theta s\psi - s\phi c\psi & c\phi c\theta \end{bmatrix}$$

and in which c and s denote the cosine and sine functions, respectively. $[R]$ is an orthonormal transformation between the two coordinate systems; as a result, the inverse transformation giving the unit vectors of the G-F frame in terms of those of the B-F frame is simply

$$\begin{bmatrix} \vec{i} \\ \vec{j} \\ \vec{k} \end{bmatrix} = [R]^T \begin{bmatrix} \vec{i} \\ \vec{j} \\ \vec{k} \end{bmatrix} \quad (2.2 - 2)$$

where $[R]^T$ is the transpose of $[R]$.

Because the origins of the two frames do not coincide, equations 2.2-1 and 2.2-2 must be modified in order to give the transformation from the ground axes to the body axes. This is done by introducing the position vector of the origin of the B-F frame as follows:

$$\begin{bmatrix} x \\ y \\ z \end{bmatrix} = [R] \begin{bmatrix} X - X_A \\ Y - Y_A \\ Z - Z_A \end{bmatrix} \quad (2.2 - 3)$$

where X_A , Y_A , and Z_A are coordinates of the origin of the B-F frame in terms of those of the G-F frame. Equation 2.2-3 transforms the coordinates of a point in the ground axes (X,Y,Z) to the body axes (x,y,z) . Inverting equation 2.2-3 yields

$$\begin{bmatrix} X \\ Y \\ Z \end{bmatrix} = [R]^T \begin{bmatrix} x \\ y \\ z \end{bmatrix} + \begin{bmatrix} X_A \\ Y_A \\ Z_A \end{bmatrix} \quad (2.2 - 4)$$

Equation 2.2-4 transforms the coordinates of a point in the body axes (x,y,z) to the ground axes (X,Y,Z) .

Next, the velocity at any point in space, say point P in figure 2, will be derived. The position vector of point P can be written simply,

$$\vec{R} = \vec{R}_A + \vec{r} \quad (2.2 - 5)$$

where \vec{R} is the position vector of point P in terms of the G-F frame, \vec{R}_A is the position vector of the origin of the B-F frame origin in terms of the G-F frame, and \vec{r} is the position vector of point P in terms of the B-F frame.

The velocity of point P, in terms of the G-F frame, is found by taking the substantial derivative of equation 2.2-5; that is

$$\vec{V} = \vec{V}_A + \vec{\omega} \times \vec{r} + \vec{v} \quad (2.2 - 6)$$

where \vec{V} is the velocity vector of point P in terms of the G-F frame, \vec{V}_A is the velocity vector of the B-F frame origin in terms of the G-F frame, $\vec{\omega}$ is the angular velocity of the B-F frame, and \vec{v} is the velocity vector of point P relative to the B-F frame.

Equation 2.2-6 is arranged to give the velocity relative to the moving frame; that is

$$\vec{v} = \vec{V} - \vec{V}_A - \vec{\omega} \times \vec{r} \quad (2.2 - 7)$$

Equation 2.2-7 will be useful later for convecting the wake and computing the pressure jump across the wing.

The angular velocity vector of the moving frame, $\vec{\omega}$, is derived in terms of the derivatives of the Euler angles; that is

$$\begin{aligned} \vec{\omega} &= \omega_x \vec{i} + \omega_y \vec{j} + \omega_z \vec{k} \\ &= \dot{\psi} \vec{k}_1 + \dot{\theta} \vec{j}_2 + \dot{\phi} \vec{i}_3 \end{aligned}$$

where ω_x , ω_y and ω_z are the three components of the angular velocity, $\vec{\omega}$, in the positive directions of the x-, y- and z-axes, respectively while $\dot{\psi}$, $\dot{\theta}$ and $\dot{\phi}$ are the

ordinary derivatives of ψ , θ and ϕ with respect to time, respectively, and \vec{k}_1 , \vec{j}_2 and \vec{i}_3 are unit vectors along z_1 , y_2 and x_3 axes, respectively (see figure 3). As shown in appendix A, one finds

$$\omega_x = \dot{\phi} - \dot{\psi} \sin \theta$$

$$\omega_y = \dot{\theta} \cos \phi + \dot{\psi} \cos \theta \sin \phi$$

$$\omega_z = -\dot{\theta} \sin \phi + \dot{\psi} \cos \theta \cos \phi$$

Or in matrix form

$$\begin{bmatrix} \omega_x \\ \omega_y \\ \omega_z \end{bmatrix} = [C] \begin{bmatrix} \dot{\phi} \\ \dot{\theta} \\ \dot{\psi} \end{bmatrix} \quad (2.2 - 8)$$

where

$$[C] = \begin{bmatrix} 1 & 0 & -s\theta \\ 0 & c\phi & s\phi c\theta \\ 0 & -s\phi & c\phi c\theta \end{bmatrix}$$

One can invert equation 2.2-8, as shown in appendix A, to express the derivative of the Euler angles in terms of the angular velocity of the moving frame, that is

$$\begin{bmatrix} \dot{\phi} \\ \dot{\theta} \\ \dot{\psi} \end{bmatrix} = [C]^{-1} \begin{bmatrix} \omega_x \\ \omega_y \\ \omega_z \end{bmatrix} \quad (2.2 - 9)$$

where

$$[C]^{-1} = \begin{bmatrix} 1 & \frac{s\phi s\theta}{c\theta} & \frac{c\phi s\theta}{c\theta} \\ 0 & c\phi & -s\phi \\ 0 & \frac{s\phi}{c\theta} & \frac{c\phi}{c\theta} \end{bmatrix}$$

$[C]^{-1}$ is singular at $\theta = \frac{1}{2}(2n + 1)\pi$ for $n=0,1,2, \dots$ which corresponds to a pitch-like rotation of 90° , 270° , etc. In this dissertation such cases are not considered.

The description of the coordinate systems and their relationships have been described in detail. Next, the general unsteady vortex-lattice method is introduced and the modification necessary to model unsteady ground effect is described.

2.3 The General Unsteady Vortex-Lattice Method

The general unsteady vortex-lattice method was described in detail by Konstadinopoulos (1981) and Elzebda (1986). In this dissertation, we extend the method to include the ground effects. Below, we briefly describe the vortex-lattice method.

The flow is incompressible and inviscid and separates only along the sharp edges of the wing. The ground plane is replaced by the images of the real wing and its wake as mentioned earlier. So, the problem of a wing flying near the ground is converted into the problem of two identical wings moving together while satisfying the no-penetration boundary condition all the time at the plane of symmetry (the ground plane); that is, the plane of symmetry is a stream surface.

When the wing and its image are suddenly set in motion, the fluid is set in motion too. Boundary layers on the upper and lower surfaces are generated as a result of the no-slip boundary condition. This in turn generates vorticity in the flow. The vortices that form along the sharp edges are shed and convected downstream. This process of shedding vorticity forms the wakes of the wing and its image.

In the numerical model, boundary layers on the upper and lower surfaces are merged into a single vortex sheet along the camber surface. As a result, all vorticity is confined to thin regions over the surfaces of the wing and its image. Both the wings and their wakes are represented by sheets of vorticity. These sheets consist of two parts. The part representing the wing has its position specified. As a result, it is called the "bound vortex sheet" and a pressure jump may exist across it. While the other part representing the wake does not have its position given in advance. It deforms freely and assumes a force-free position during the simulation. As a result, it is called the "free vortex sheet" and no pressure jump can exist across it. The bound and free vortex sheets are joined along the sharp edges where separation occurs and the Kutta condition is imposed.

The entire vortex sheet, bound and free, is replaced with discrete vortex rings. Each vortex ring, in general, consists of four short straight vortex segments. The circulation is taken to be the same for all four segments of the same loop to ensure spatial conservation of circulation. Each vortex segment is shared by two adjoining loops, except the ones along the first row, and its strength is equal to the difference in circulations of the two loops to which it belongs.

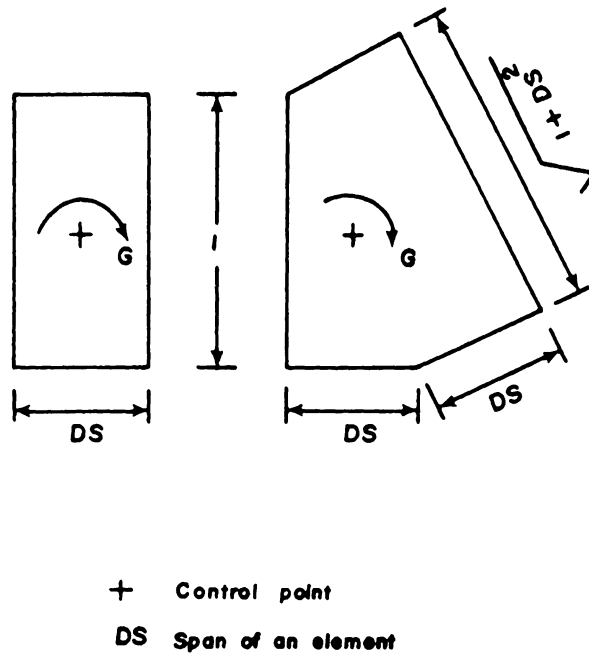
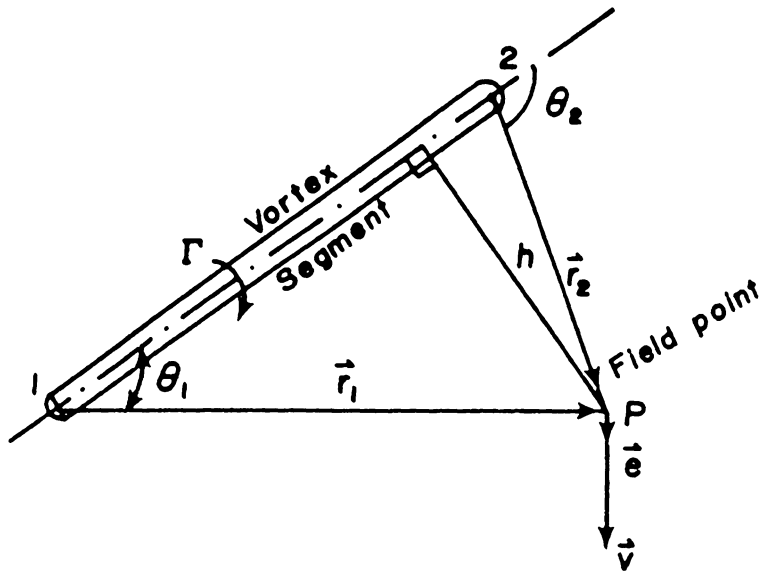


Figure 4. A typical rectangular and leading-edge elements.

The shape of each element is chosen to be a trapezoid. The leading-edge separation of delta wings is simulated by adding leading-edge extensions at each node, as shown in figure 4. This is done by placing the extensions in the plane of the wing and normal to the leading edge and giving them a length equal to the span of an element. As a result, the leading-edge element has five sides instead of four.

The absolute velocity induced by all discrete vortex segments is computed according to the Biot-Savart law. Thus, the Biot-Savart law is the building block of the present numerical method. So, it may be in order to discuss the Biot-Savart law and how it is implemented in the computer code before proceeding further with the general unsteady vortex-lattice method.



Γ Circulation around the vortex segment

P is an arbitrary point in space

Figure 5. Velocity field due to a finite strength vortex filament.

In figure 5, a vortex segment extending from 1 to 2 is shown. The velocity field induced by this vortex segment at point P is given by the Biot-Savart law (see Karamcheti, 1980):

$$\vec{V} = \frac{\vec{e}\Gamma}{4\pi h} (\cos \theta_1 - \cos \theta_2) \quad (2.3 - 1)$$

where \vec{V} is the absolute velocity with respect to the G-F frame, \vec{e} is a unit vector normal to the plane of points 1, 2 and P , Γ is the circulation around the vortex segment, h is the distance between point P and the segment, and θ_1 and θ_2 are the angles between the vortex segment and the lines connecting the end of the vortex segment to P , respectively. The divergence of \vec{V} is zero.

Equation 2.3-1 will be put in a new form that is suitable for programming purposes. From figure 5, it is clear that

$$\begin{aligned}\vec{\Omega} \times \vec{r}_1 &= \vec{e} |\vec{\Omega}| |\vec{r}_1| \sin \theta_1 \\ &= \vec{e} |\vec{\Omega}| h,\end{aligned}\tag{2.3 - 2}$$

$$\vec{\Omega} \cdot \vec{r}_1 = |\vec{\Omega}| |\vec{r}_1| \cos \theta_1\tag{2.3 - 3}$$

and

$$\vec{\Omega} \cdot \vec{r}_2 = |\vec{\Omega}| |\vec{r}_2| \cos \theta_2\tag{2.3 - 4}$$

where $\vec{\Omega}$ is the vector from point 1 to point 2, \vec{r}_1 is the vector from point 1 to point P and \vec{r}_2 is the vector from point 2 to point P. From equation 2.3-2, we obtain

$$\vec{e} = \frac{\vec{\Omega} \times \vec{r}_1}{|\vec{\Omega}| h}\tag{2.3 - 5}$$

Substituting equations 2.3-3, 2.3-4 and 2.3-5 into equation 2.3-1, one obtains the following equation:

$$\vec{v} = \frac{\Gamma(\vec{\Omega} \times \vec{r}_1)}{4\pi |\vec{\Omega}| h^2} \left[\frac{\vec{\Omega} \cdot \vec{r}_1}{|\vec{\Omega}| |\vec{r}_1|} - \frac{\vec{\Omega} \cdot \vec{r}_2}{|\vec{\Omega}| |\vec{r}_2|} \right]\tag{2.3 - 6}$$

But $|\vec{e}| = 1$, hence from equation 2.3-5

$$|\vec{\Omega} \times \vec{r}_1| = |\vec{\Omega}| h\tag{2.3 - 7}$$

Equation 2.3-6 becomes after substituting equation 2.3-7

$$\vec{v} = \frac{\Gamma(\vec{\Omega} \times \vec{r}_1)}{4\pi|\vec{\Omega} \times \vec{r}_1|^2} \left[\vec{\Omega} \cdot \left(\frac{\vec{r}_1}{|\vec{r}_1|} - \frac{\vec{r}_2}{|\vec{r}_2|} \right) \right] \quad (2.3 - 8)$$

\vec{v} is evaluated according to equation 2.3-8 by the computer thousands of times for a typical run. One can reduce the execution time by reducing the number of operations. Looking back at the equation, one can notice the constant 4π . An obvious way for reducing the execution time, is to delay the division by 4π operation until the solution is completed. To incorporate this concept, we solve for $\frac{\Gamma}{4\pi}$ instead of Γ . The resulting equation is

$$\vec{v} = \frac{\Gamma'(\vec{\Omega} \times \vec{r}_1)}{|\vec{\Omega} \times \vec{r}_1|^2} \left[\vec{\Omega} \cdot \left(\frac{\vec{r}_1}{|\vec{r}_1|} - \frac{\vec{r}_2}{|\vec{r}_2|} \right) \right] \quad (2.3 - 9)$$

where $\Gamma' = \frac{\Gamma}{4\pi}$. In order to make the subroutine that solves equation 2.3-9 as general as possible, Γ' is set equal to one. Then, the results returned from the subroutine can be multiplied by the value of Γ' . For $\Gamma' = 1$ equation 2.3-9 becomes

$$\vec{v} = \frac{(\vec{\Omega} \times \vec{r}_1)}{|\vec{\Omega} \times \vec{r}_1|^2} \left[\vec{\Omega} \cdot \left(\frac{\vec{r}_1}{|\vec{r}_1|} - \frac{\vec{r}_2}{|\vec{r}_2|} \right) \right] \quad (2.3 - 10)$$

In the computer code, the coordinates of the points 1, 2 and P are supplied as input parameters to a subroutine that uses equation 2.3-10 to compute the velocity field induced by a vortex segment having circulation of 4π and returns the three components of the velocity. From equation 2.3-1, it is clear that as point P approaches the vortex segment between its ends, the magnitude of the induced velocity approaches infinity. This singularity is avoided by introducing a cut-off length

below which the subroutine gives zero for all three components of \vec{V} . The cut-off length is specified in terms of the length of the vortex segment (for more detail about the effect of the cut-off length, see Konstadinopoulos 1981, Konstadinopoulos 1984 and/or Elzebda 1986). The complete algorithm is:

1. The coordinates of the points 1, 2 and P are supplied to the subroutine as (x_1, y_1, z_1) , (x_2, y_2, z_2) and (x_p, y_p, z_p) , respectively.

2. The vector $\vec{\Omega}$ is computed as follow:

$$\vec{\Omega} = (x_2 - x_1)\vec{I} + (y_2 - y_1)\vec{J} + (z_2 - z_1)\vec{K}$$

3. The vectors \vec{r}_1 and \vec{r}_2 are computed as follow:

$$\vec{r}_1 = (x_p - x_1)\vec{I} + (y_p - y_1)\vec{J} + (z_p - z_1)\vec{K}$$

and

$$\vec{r}_2 = (x_p - x_2)\vec{I} + (y_p - y_2)\vec{J} + (z_p - z_2)\vec{K}$$

4. The dot products $\vec{\Omega} \cdot \vec{r}_1$ and $\vec{\Omega} \cdot \vec{r}_2$ are evaluated.

5. The cross product $\vec{\Omega} \times \vec{r}_1$ is evaluated.

6. The magnitude of $\vec{\Omega} \times \vec{r}_1$ is evaluated.

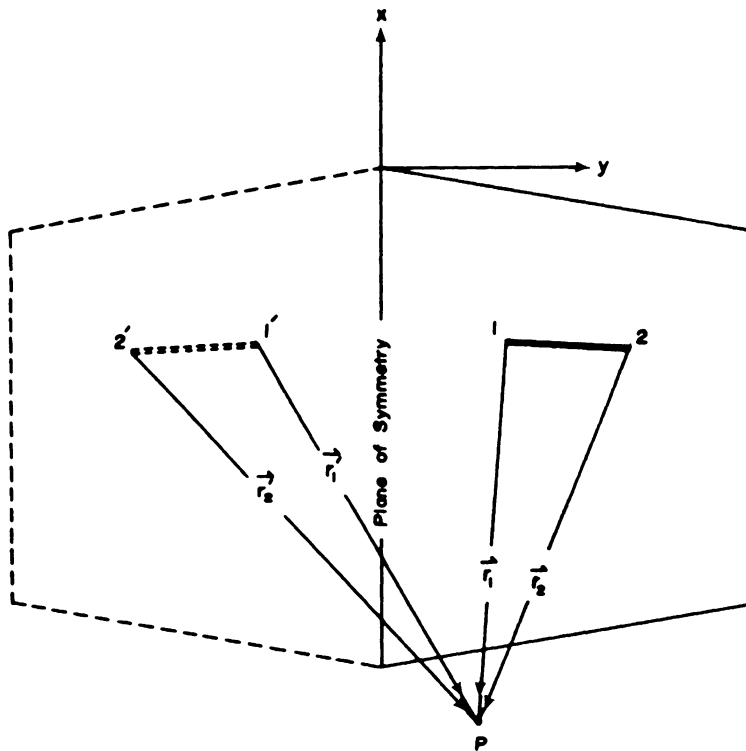
7. The following condition is checked:

$$|\vec{\Omega} \times \vec{r}_1|^2 \geq (\text{cutoff})^2 ?$$

8. If the above condition is not satisfied then $\vec{V} = \vec{0}$ and the subroutine returns to the main program.
9. If the above condition is satisfied then the magnitudes of \vec{r}_1 and \vec{r}_2 are evaluated and \vec{V} is set equal to

$$\frac{(\vec{\Omega} \times \vec{r}_1)}{|\vec{\Omega} \times \vec{r}_1|^2} \left[\frac{\vec{\Omega} \cdot \vec{r}_1}{|\vec{r}_1|} - \frac{\vec{\Omega} \cdot \vec{r}_2}{|\vec{r}_2|} \right]$$

and the subroutine returns to the main program.



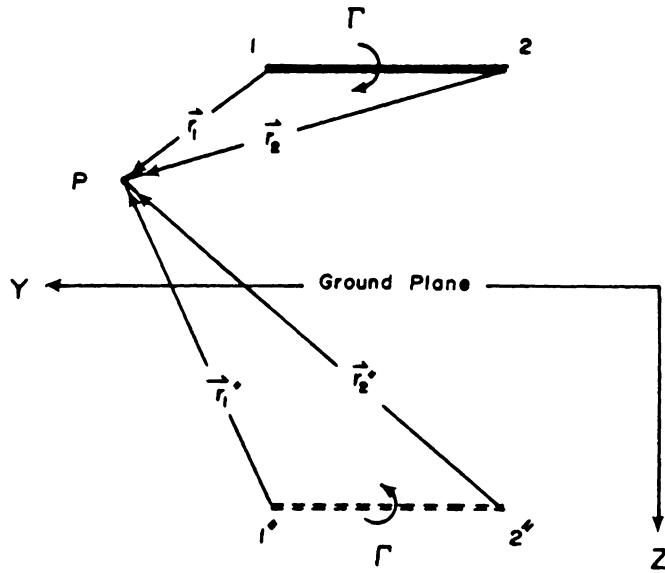
P is an arbitrary point in space

Figure 6. A vortex segment and its image to the left of the x-z plane.

When the flow is symmetric, one can reduce the computation time. In this research, we use only one half of the lifting surface (except when the cross wind is considered). The effect of the other half (of the lifting surfaces) is included by modifying equation 2.3-10. In figure 6, a vortex segment and its image to the left of the x-z plane are shown. Points 1' and 2' are the images of points 1 and 2 with respect to the x-z plane, respectively. Consequently, their x- and z-coordinates are the same as those of the points 1 and 2; their y-coordinates are opposite in sign. The circulation around vortex segment 2'1' is the same as that around vortex segment 12. Equation 2.3-10 becomes

$$\vec{v} = \frac{(\vec{\Omega} \times \vec{r}_1)}{|\vec{\Omega} \times \vec{r}_1|^2} \left[\vec{\Omega} \cdot \left(\frac{\vec{r}_1}{|\vec{r}_1|} - \frac{\vec{r}_2}{|\vec{r}_2|} \right) \right] + \frac{(\vec{\Omega}' \times \vec{r}'_2)}{|\vec{\Omega}' \times \vec{r}'_2|^2} \left[\vec{\Omega}' \cdot \left(\frac{\vec{r}'_2}{|\vec{r}'_2|} - \frac{\vec{r}'_1}{|\vec{r}'_1|} \right) \right] \quad (2.3 - 11)$$

where $\vec{\Omega}'$ is the vector from point 2' to point 1', \vec{r}'_1 is the vector from point 1' to point P and \vec{r}'_2 is the vector from point 2' to point P.



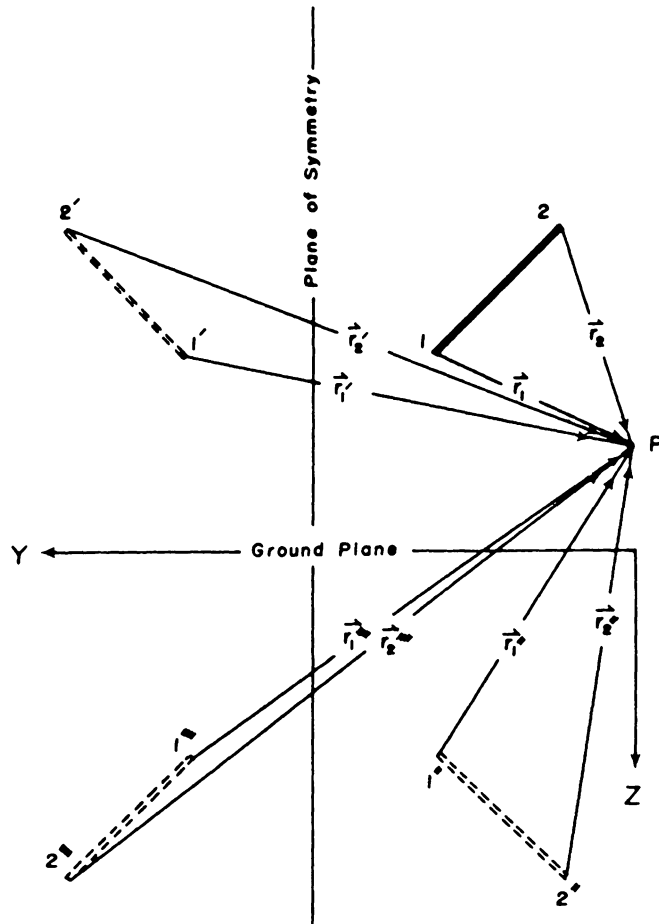
P is an arbitrary point in space

Figure 7. A vortex segment and its image below the ground plane.

In this research, The ground effect is simulated by the image technique; namely the images of the real wing and its wake are placed below the ground plane and thereby make the ground a plane of symmetry. Accordingly, the ground effect is included by modifying equation 2.3-10 (or equation 2.3-11 for symmetrical flight). In figure 7, a vortex segment and its image below the ground plane are shown. Points 1'' and 2'' are the images of points 1 and 2 with respect the ground plane, respectively. Hence, the X- and Y-coordinates of the image of the vortex segment are equal to those of the real one; the Z coordinate is opposite in sign. The circulations are reversed. Equation 2.3-10 becomes:

$$\vec{v} = \frac{(\vec{\Omega} \times \vec{r}_1)}{|\vec{\Omega} \times \vec{r}_1|^2} \left[\vec{\Omega} \cdot \left(\frac{\vec{r}_1}{|\vec{r}_1|} - \frac{\vec{r}_2}{|\vec{r}_2|} \right) \right] - \frac{(\vec{\Omega}'' \times \vec{r}''_1)}{|\vec{\Omega}'' \times \vec{r}''_1|^2} \left[\vec{\Omega}'' \cdot \left(\frac{\vec{r}''_1}{|\vec{r}''_1|} - \frac{\vec{r}''_2}{|\vec{r}''_2|} \right) \right] \quad (2.3 - 12)$$

where $\vec{\Omega}''$ is the vector from point 1'' to point 2'', \vec{r}''_1 is the vector from point 1'' to point P and \vec{r}''_2 is the vector from point 2'' to point P.



P is an arbitrary point in space

Figure 8. A vortex segment and its three images for the symmetric case.

In figure 8, a vortex segment and its three images are shown for symmetric flow. Points 1''' and 2''' are the images of points 1' and 2' with respect to the ground plane, respectively. Similarly, Equation 2.3-11 is modified in order to capture the ground effect for a symmetrical flight. The resulting equation is

$$\begin{aligned}
\vec{v} = & \frac{(\vec{\Omega} \times \vec{r}_1)}{|\vec{\Omega} \times \vec{r}_1|^2} \left[\vec{\Omega} \cdot \left(\frac{\vec{r}_1}{|\vec{r}_1|} - \frac{\vec{r}_2}{|\vec{r}_2|} \right) \right] \\
& + \frac{(\vec{\Omega}' \times \vec{r}'_2)}{|\vec{\Omega}' \times \vec{r}'_2|^2} \left[\vec{\Omega}' \cdot \left(\frac{\vec{r}'_2}{|\vec{r}'_2|} - \frac{\vec{r}'_1}{|\vec{r}'_1|} \right) \right] \\
& - \frac{(\vec{\Omega}'' \times \vec{r}''_1)}{|\vec{\Omega}'' \times \vec{r}''_1|^2} \left[\vec{\Omega}'' \cdot \left(\frac{\vec{r}''_1}{|\vec{r}''_1|} - \frac{\vec{r}''_2}{|\vec{r}''_2|} \right) \right] \\
& - \frac{(\vec{\Omega}''' \times \vec{r}'''_2)}{|\vec{\Omega}''' \times \vec{r}'''_2|^2} \left[\vec{\Omega}''' \cdot \left(\frac{\vec{r}'''_2}{|\vec{r}'''_2|} - \frac{\vec{r}'''_1}{|\vec{r}'''_1|} \right) \right]
\end{aligned} \tag{2.3 - 13}$$

where $\vec{\Omega}'''$ is the vector from point 2''' to point 1''', \vec{r}'''_1 is the vector from point 1''' to point P and \vec{r}'''_2 is the vector from point 2''' to point P. The implementation of equation 2.3-13 in the computer code is shown in appendix B.

Now we continue the discussion of the general vortex-lattice method. The vortex sheets are replaced with a lattice of discrete vortex lines. The total velocity field induced by those vortex lines must satisfy the continuity equation, and the following conditions:

1. $\vec{V}_{Disturbance} \rightarrow \vec{0}$ at infinity
2. The vertical velocity component is zero on the ground plane.
3. The no-penetration condition is satisfied on the lifting surfaces.
4. The pressure is continuous in the wake.
5. There is spatial conservation of circulation.

6. The unsteady Kutta condition is satisfied along the lines where the free and bound sheets are joined.

Because the induced velocity is computed according to the Biot-Savart law, equation 2.3-10, the continuity equation and the first condition are satisfied. Because the method of images is used the ground is a plane of symmetry and hence the second condition is satisfied too. The third condition is written simply,

$$(\vec{V} - \vec{V}_{LS}) \cdot \vec{n} = 0 \quad \text{on } S_{LS} \quad (2.3 - 14)$$

where \vec{V} is the absolute velocity of a fluid particle, \vec{V}_{LS} is the absolute velocity of the point on the wing in contact with the fluid particle, \vec{n} is the unit vector that is normal to the wing, and S_{LS} is the lifting (wing) surface. Equation 2.3-14 is discussed in detail later. The fourth condition is satisfied by convecting the wake at the local particle velocity, as required by the Kelvin-Helmholtz theorem (Konstadinopoulos, 1981). The fifth condition is satisfied by taking the circulation to be the same for all the discrete vortex segments of the same loop. The sixth condition is satisfied by shedding all the vorticity formed along the sharp edges where the steady Kutta condition is imposed; more details will be given later.

Before proceeding further in the discussion, we write all variables in dimensionless form by introducing the following characteristic variables:

U is a speed characterizing the motion of the wing. The dimensionless speed is always one.

L is the physical length of the chordwise increment of the bound lattice. The dimensionless chordwise increment is always one regardless of the number of the chordwise elements used.

$\frac{L}{U}$ is the characteristic time. The computational time step is taken to be

unity. This yields lengths in the wake that are about the same as those on the wing.

The dimensionless variables are introduced as follows:

$$\vec{V} = \frac{\vec{V}^*}{U}, \Phi = \frac{\Phi^*}{UL}, \vec{r} = \frac{\vec{r}^*}{L}, \vec{V}_A = \frac{\vec{V}_A^*}{U}, \vec{\omega} = \vec{\omega}^* \frac{L}{U}, P = \frac{P^*}{\rho^* U^2} \text{ and } t = t^* \frac{U}{L}$$

where Φ is the velocity potential with respect to the G-F frame, P is the pressure, ρ is the air density; the rest of the variables were defined before. The asterisks denote the physical quantities.

We now return to equation 2.3-14. The lifting surface is discretized into a finite number of elements. The no-penetration boundary condition is imposed at one point in each finite element. These are called control points. The control point is the centroid of the four corners of the element. Equation 2.3-14 becomes

$$\sum_{j=0}^N A_{ij} G_j = (\vec{V}_{LSi} - \vec{V}_{wi}) \cdot \vec{n}_i \quad \text{on } S_{LS} \quad \text{for } i=1,2, \dots, N \quad (2.3-15)$$

in which A_{ij} represents the normal component of the velocity induced at the control point of the i -th element by the vortex ring, having a unit circulation, around element j and its image. A_{ij} is called the influence matrix. In general, the A_{ij} are functions of space and/or time. G_j is the circulation of the vortex ring at element j . \vec{V}_{wi} is the velocity induced by the wake and its image whose position and circulation distribution are known. \vec{n}_i is the unit normal vector at the control point of the i -th element. \vec{V}_{LSi} is the absolute velocity of the wing at the control point of the i -th element. In general, the \vec{V}_{LSi} are functions of space and/or time. They are computed according to equation 2.2-7 by setting $\vec{v} = 0$, so that:

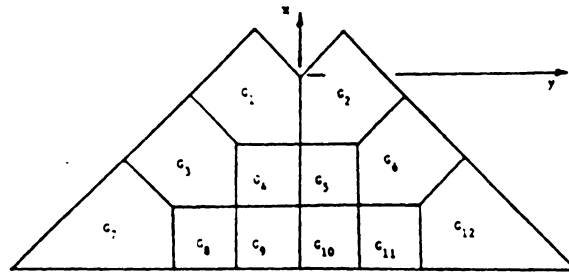
$$\vec{V}_{LSi} = \vec{V}_A + \vec{\omega} \times \vec{r}_i \quad (2.3 - 16)$$

where \vec{r}_i is the position vector of the control point of the i-th element relative to the B-F frame.

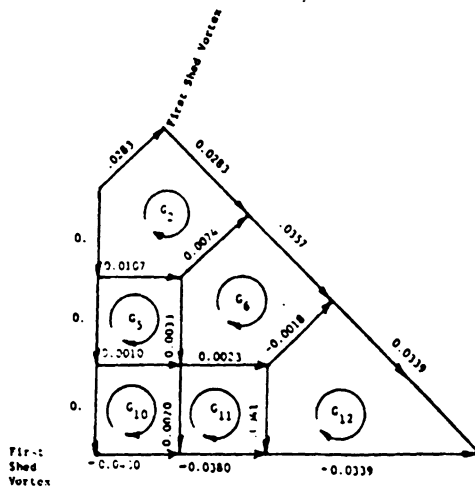
In order to solve equation 2.3-15, an initial condition must be prescribed. The initial condition describes the wake, giving the position and vorticity distribution. One special case of interest is when the wing is put into motion impulsively. At this instant, no wake yet exists; hence, \vec{V}_{wi} is zero, and equation 2.3-15 reduces to the following:

$$\sum_{j=0}^N A_{ij} G_j = \vec{V}_{LSi} \cdot \vec{n}_i \quad \text{on } S_{LS} \quad \text{for } i = 1, 2, \dots, N \quad (2.3 - 17)$$

Equation 2.3-17 is solved for the unknown circulations, G_j , by Gauss elimination. The system of equations 2.3-17 can be solved by iterative schemes as well; those are, for example, Jacobi and Gauss-Seidel iterative methods. When the matrix of influence coefficients, A_{ij} , is constant the matrix is inverted once; but when A_{ij} is variable, Gauss elimination is used at each time step. At the beginning of the first time step, $t = 1$, all the circulations in the bound and free portions of the vortex lattice are zero, as shown in figure 9a. Figure 9 was taken from Elzebda (1986). At the end of the first time step, $t = 1$, the circulations in the bound portion have changed, as shown in figure 9b, and a vortex line is formed along the sharp edges. This is the starting vortex dictated by the requirement of spatial conservation of circulation. At the beginning of the second time step, $t = 2$, in order to satisfy the unsteady Kutta condition, all the vorticity formed along the sharp edges where Kutta condition is imposed in the steady state is convected downstream at the local particle velocity.



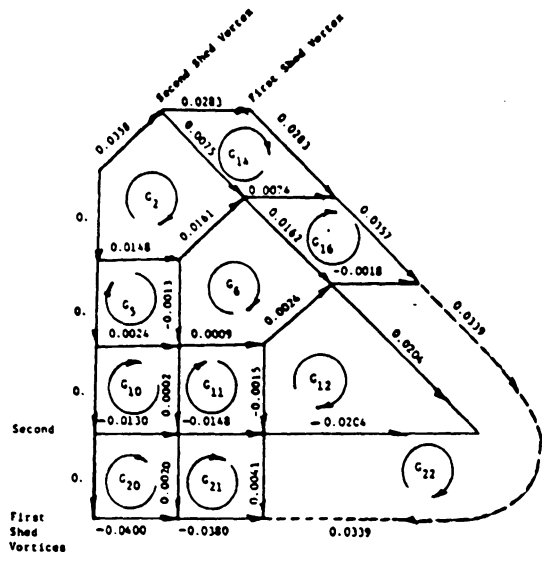
(a)



$G_1 = 0.0282837269$	$G_7 = 0.0338835404$
$G_2 = 0.0282837269$	$G_8 = 0.0380137253$
$G_3 = 0.0356739174$	$G_9 = 0.0399843350$
$G_4 = 0.0390180502$	$G_{10} = 0.0399843350$
$G_5 = 0.0390180502$	$G_{11} = 0.0380137253$
$G_6 = 0.0356739174$	$G_{12} = 0.0338835404$

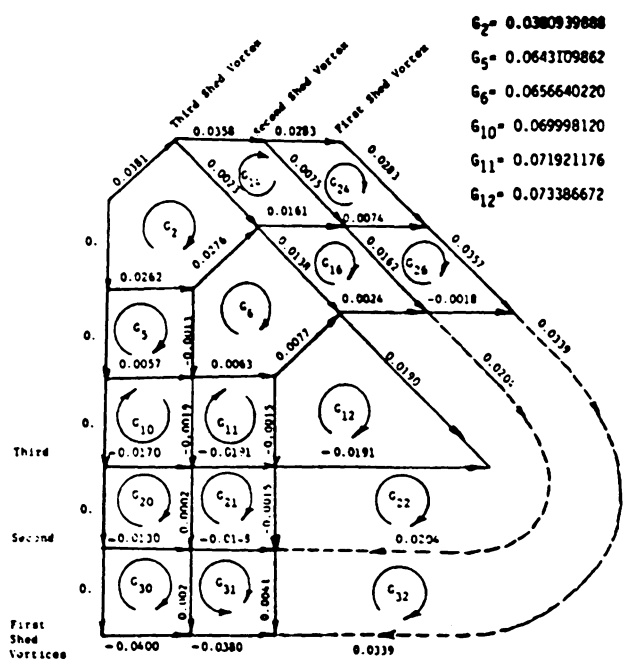
(b)

Figure 9. Circulation around the closed loops and individual vortex segments of delta wing: (a) just before the start of the motion, (b) after one time step, (c) after two time steps and (d) after three time steps taken from Elzebeda (1986).



- $G_2 = 0.0357958638$
- $G_5 = 0.0505862689$
- $G_6 = 0.0519090977$
- $G_{10} = 0.0529538379$
- $G_{11} = 0.0528088195$
- $G_{12} = 0.0542843042$
- $G_{14} = 0.0282837269$
- $G_{16} = 0.0356739174$
- $G_{20} = 0.0399843350$
- $G_{21} = 0.0380137253$
- $G_{22} = 0.0338835404$

(c)



- $G_2 = 0.0380939888$
- $G_5 = 0.0643109862$
- $G_6 = 0.0656640220$
- $G_{10} = 0.069998120$
- $G_{11} = 0.071921176$
- $G_{12} = 0.073386672$
- $G_{14} = 0.035798638$
- $G_{16} = 0.051909098$
- $G_{20} = 0.052953838$
- $G_{21} = 0.052808820$
- $G_{22} = 0.054284304$
- $G_{24} = 0.028283727$
- $G_{26} = 0.035673917$
- $G_{30} = 0.039984335$
- $G_{31} = 0.038013725$
- $G_{32} = 0.033883504$

(d)

Figure 9. Continued.

This local particle velocity is computed according to equation 2.2-7. Equation 2.2-7 is rewritten again for convenience:

$$\vec{v} = \vec{V} - \vec{V}_A - \vec{\omega} \times \vec{r} \quad (2.3 - 18)$$

where \vec{V} is the absolute velocity computed by the Biot-Savart law, equation 2.3-10.

Equation 2.3-18 is used to compute the local particle velocity at each node of the wake in the moving reference frame. Despite the fact that all quantities in equation 2.3-18 are functions of time, the quantities which are computed at the previous time step, ($t = 1$), are used. The justification is that computing the quantities at the present time step, ($t = 2$), requires iterations, which in turn, as stated by Konstadinopoulos (1981) "increases the computation time without any significant improvement in the accuracy of the method". The starting vortex is convected downstream. Its circulation at the new position is the same as the circulation around the starting vortex at $t = 1$ in order to guarantee the temporal conservation of circulation. In order to guarantee the spatial conservation of circulation, the starting vortices at the old and new positions are joined at the nodal points with connectors, as shown in figure 9c. The new position of the node i is computed by the following equation:

$$\vec{R}_i(2) = \vec{R}_i(1) + \vec{v}_i(1)\Delta t \quad (2.3 - 19)$$

The wake is created as a result of shedding the starting vortices. The bound circulations are calculated at the second time step, ($t = 2$), using equation 2.3-15 and including the effects of the wake and its image. A second starting vortex forms along the sharp edges as shown in figure 9c. The second starting vortex is then shed and convected downstream to its new position as required by the unsteady Kutta condition. Simultaneously, the first starting vortex is convected to its new position.

The wake is growing. The bound circulations are computed at the end of the third time step, $t=3$. A third starting vortex forms along the sharp edges as shown in figure 9d. The procedure for finding the solution of equation 2.3-15 can be repeated for any desired number of steps. In figure 10, an actual computed wake of a delta wing near the ground is shown.

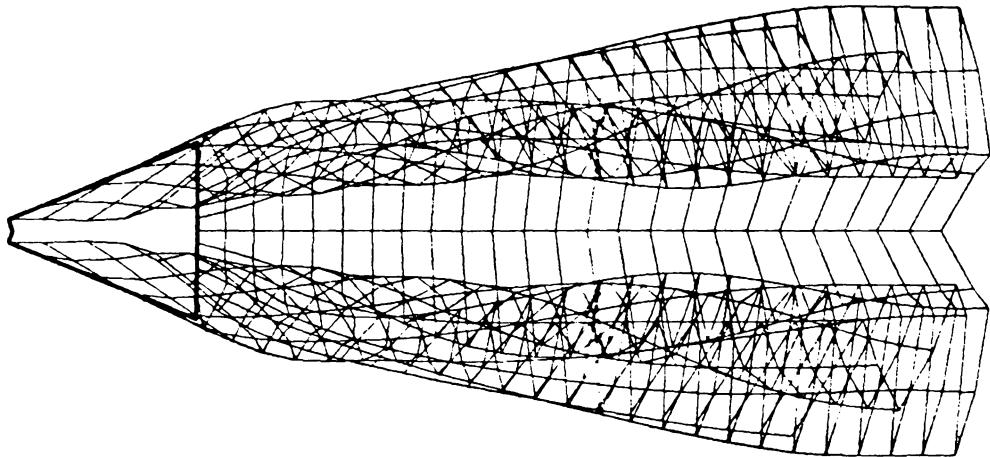


Figure 10. An actual computed wake of a delta wing near the ground: top view for steady flow.

2.4 Computation of the Aerodynamic Loads

The aerodynamic forces and moments are computed after the pressure jump distribution across the bound lattice is found. The pressure jump across each element is computed at the control point of the element by using the unsteady Bernoulli's equation. The unsteady Bernoulli's equation in terms of dimensionless variables is written as follows:

$$\frac{\partial \Phi}{\partial t} + \frac{1}{2} \vec{V} \cdot \vec{V} + P = H(t) \quad (2.4 - 1)$$

where $H(t)$ is a function of dimensionless time and the rest of the variables were defined earlier.

At infinity, Φ is constant and the velocity is zero; therefore, equation 2.4-1 becomes as follows:

$$P_{\infty} = H(t) = \text{a constant} \quad (2.4 - 2)$$

The pressure coefficient, C_p , is obtained by combining equations 2.4-1 and 2.4-2; it takes the following form

$$\begin{aligned} C_p &= 2(P - P_{\infty}) \\ &= -2 \frac{\partial \Phi}{\partial t} - \vec{V} \cdot \vec{V} \end{aligned} \quad (2.4 - 3)$$

where $\frac{\partial \Phi(\vec{R}, t)}{\partial t}$ is the partial derivative with respect to time of the potential function for a fixed value of \vec{R} . There are some advantages when $\frac{\partial \Phi(\vec{R}, t)}{\partial t}$ is in terms of $\frac{\partial \phi(\vec{r}, t)}{\partial t}$, which is the potential function that is expressed in terms of the relative position vector \vec{r} and time, t . Konstadinopoulos (1981) derived the following relation:

$$\frac{\partial \Phi(\vec{R}, t)}{\partial t} = \frac{\partial \phi(\vec{r}, t)}{\partial t} - \vec{V} \cdot (\vec{V}_A + \vec{\omega} \times \vec{r}) \quad (2.4 - 4)$$

After substituting equation 2.4-4 into equation 2.4-3, one finds that the pressure coefficient takes the following form:

$$C_p = -2 \frac{\partial \phi}{\partial t} - \vec{V} \cdot (\vec{V} + \vec{V}_A + \vec{\omega} \times \vec{r}) \quad (2.4 - 5)$$

The pressure jump is the difference between the pressure coefficients on the upper and lower surfaces. That is

$$\Delta C_p = C_{pu} - C_{pl}$$

in which the subscripts *u* and *l* denote the upper and lower surfaces, respectively.

The pressure jump is given by the following relation:

$$\Delta C_p = -2 \frac{\partial(\phi_u - \phi_l)}{\partial t} - (\vec{V}_u + \vec{V}_l) \cdot (\vec{V}_u - \vec{V}_l) + 2(\vec{V}_u - \vec{V}_l) \cdot (\vec{V}_A + \vec{\omega} \times \vec{r}) \quad (2.4 - 6)$$

The evaluation of each term in the right hand side of equation 2.4-6 is discussed next.

1. The quantity $(\phi_u - \phi_l)$ is the difference at any instant between velocity potentials on the upper and lower surfaces at the same control point. This term is evaluated by integrating the velocity along a path that starts just above the control point, goes upstream all the way around the leading edge, then comes back downstream to just below the control point. Konstadinopoulos (1981) derived the following simple result:

$$(\phi_u - \phi_l)_l = G_l$$

The term $\frac{\partial(\phi_u - \phi_l)_l}{\partial t} = \frac{\partial G_l}{\partial t}$ is approximated by the following finite difference expression:

$$\frac{\partial(\phi_u - \phi_l)_i}{\partial t} \cong \frac{G_i(t + \Delta t) - G_i(t)}{\Delta t} \quad (2.4 - 7)$$

Equation 2.4-7 is evaluated by storing the values of G , for two successive time steps.

2. The quantity $(\vec{V}_u + \vec{V}_l)_i$, is the sum of the upper and lower surface velocities at the control point i . Both velocities can be written in terms of two new quantities: the mean (average) velocity and the velocity jump at the control point i ; that is

$$\vec{V}_u = \vec{V}_m + \frac{1}{2} \Delta \vec{V} \quad (2.4 - 8)$$

and

$$\vec{V}_l = \vec{V}_m - \frac{1}{2} \Delta \vec{V} \quad (2.4 - 9)$$

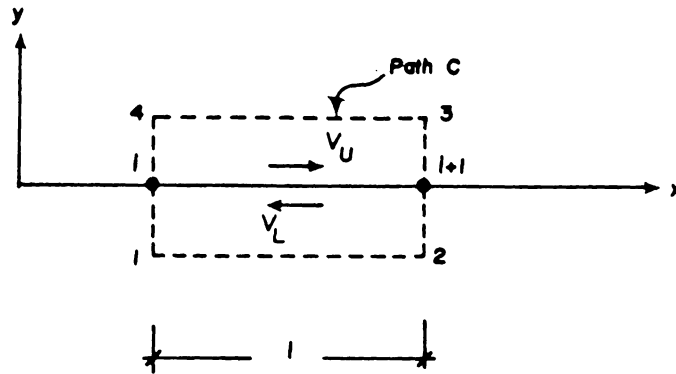
where \vec{V}_m is the mean velocity induced at the control point on an element, say i , by all the vortex rings of the wing and its wake and their images and $\Delta \vec{V}$ is the jump in the tangential velocity.

By adding equation 2.4-8 to equation 2.4-9, the following equation is obtained

$$\vec{V}_u + \vec{V}_l = 2\vec{V}_m \quad (2.4 - 10)$$

3. The quantity $(\vec{V}_u - \vec{V}_l)_i$, is the difference between velocities on the upper and lower surfaces at control point i . By subtracting equation 2.4-9 from equation 2.4-8, one can obtain the following:

$$\vec{V}_u - \vec{V}_l = \Delta \vec{V} \quad (2.4 - 11)$$



● Discrete point vortices

Figure 11. Two-dimensional discrete point vortices.

The velocity jump, $\Delta \vec{V}$, at the control point of an element i is computed from circulations of the straight vortex segments of element i . The circulation, Γ , is defined by

$$\Gamma = \oint_C \vec{V} \cdot d\vec{r} \quad (2.4 - 12)$$

in which \vec{V} is the fluid velocity and $d\vec{r}$ is a line element along a closed path C . In figure 11, two-dimensional discrete point vortices are shown. V_u and V_l are assumed to be constants. The circulation, Γ , for a two-dimensional flow is calculated using equation 2.4-12 around the path C as shown in figure 11. The closed path C starts just

below point i and goes parallel to x-axis all the way around point $i + 1$ and then comes back parallel to the x-axis all the way around point i . The result is

$$\begin{aligned}
 \Gamma &= \int_C \vec{V} \cdot d\vec{r} \\
 &= \int_1^2 \vec{V} \cdot d\vec{r} + \int_2^3 \vec{V} \cdot d\vec{r} + \int_3^4 \vec{V} \cdot d\vec{r} + \int_4^1 \vec{V} \cdot d\vec{r} \\
 &= (V_u - V_l)l \\
 &= (\Delta V)l
 \end{aligned}
 \tag{2.4 - 13}$$

where l is the distance separating the two vortices. From equation 2.4-13 the velocity jump, ΔV , is

$$\Delta V = \frac{\Gamma}{l}
 \tag{2.4 - 14}$$

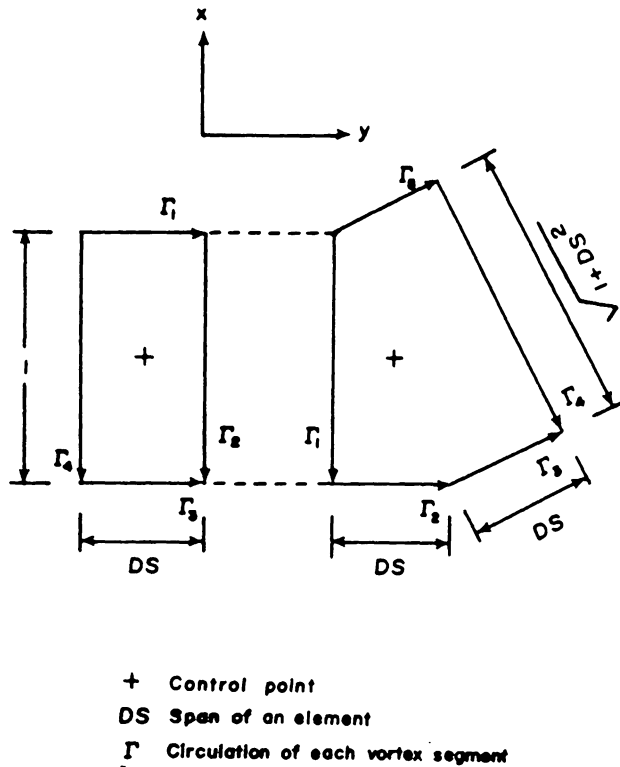


Figure 12. A rectangular and leading-edge elements of a delta wing for pressure calculations.

Equation 2.4-14 is generalized for the three-dimensional wing. In figure 12, a rectangular and leading-edge elements of a delta wing which are surrounded by discrete vortex cores are shown. Each circulation belongs to two neighboring elements. Hence, one half of each circulation is taken for each element except those along the first row. The average circulations, for the case of a rectangular element, are given by: $\frac{\Gamma_1 + \Gamma_3}{2}$ and $\frac{\Gamma_2 + \Gamma_4}{2}$ in the y and x directions, respectively. For a finite wing equation 2.4-14 is replaced by:

$$\Delta V_x = - \frac{(\Gamma_1 + \Gamma_3)}{2l_x} \quad (2.4 - 15)$$

$$\Delta V_y = - \frac{(\Gamma_2 + \Gamma_4)}{2l_y} \quad (2.4 - 16)$$

$$\Delta V_z = 0 \quad (2.4 - 17)$$

where l_x is the length separating Γ_1 and Γ_3 ; l_y is the length separating Γ_2 and Γ_4 .

Equations 2.4-15 to 2.4-17 are combined to obtain a general result that is valid for a trapezoidal element; that is

$$\Delta \vec{V} = -\vec{n} \times \frac{[F\Gamma_1\vec{l}_1 + \Gamma_2\vec{l}_2 + \Gamma_3\vec{l}_3 + \Gamma_4\vec{l}_4]}{2A} \quad (2.4 - 18)$$

where \vec{l}_1 , \vec{l}_2 , \vec{l}_3 and \vec{l}_4 are the relative position vectors along the sides of the trapezoidal element and coincide with Γ_1 , Γ_2 , Γ_3 and Γ_4 , respectively, F takes the value one, except for the first row where it takes the value two, and A is the area of the element.

The area of the element, A, is computed next. First we define two vectors \vec{B}_1 and \vec{B}_2 :

$$\vec{B}_1 = \vec{l}_2 \times \vec{l}_1 \quad \vec{B}_2 = \vec{l}_4 \times \vec{l}_3 \quad (2.4 - 19)$$

The area is given by

$$A = \frac{1}{2} [|\vec{B}_1| + |\vec{B}_2|] \quad (2.4 - 20)$$

The normal vector, \vec{n} , is

$$\vec{n} = \left[\frac{\vec{B}_1 + \vec{B}_2}{|\vec{B}_1 + \vec{B}_2|} \right] \quad (2.4 - 21)$$

In the case of an element along the leading-edge of delta wing, as shown in figure 12, equation 2.4-18 is not valid. The applicable equation for the leading edge of the delta wing will be derived. The velocity jump at the control point is given by

$$\Delta \vec{V} = -\vec{n} \times \frac{[F\Gamma_5\vec{l}_5 + \Gamma_3\vec{l}_3 + \Gamma_4\vec{l}_4]}{2A} \quad (2.4 - 22)$$

where \vec{l}_5 , \vec{l}_3 and \vec{l}_4 are the relative position vectors along the sides of the element in figure 12 with Γ_5 , Γ_3 and Γ_4 , respectively, F takes the value one, except for the first row where it takes the value two, and A is the area of the element.

The area of the element, A is computed next. First we define a vector \vec{B}

$$\vec{B} = \vec{l}_2 \times \vec{l}_1 \quad (2.4 - 23)$$

The area is given by

$$A = \frac{1}{2} |\vec{B}| \quad (2.4 - 24)$$

The normal vector is

$$\vec{n} = \frac{\vec{B}}{|\vec{B}|} \quad (2.4 - 25)$$

It should be noted that in equation 2.4-22 the terms $\Gamma_1\vec{l}_1$ and $\Gamma_2\vec{l}_2$ are omitted. Konstadinopoulos (1981) said "omitting these terms may appear arbitrary, but it is necessary for equation 2.4-22 to reduce to the proper form for steady flow". He then added, "Experimental evidence shows that, in steady flow, all vorticity leaves the wing (approximately) in a direction normal to the leading edge". He pointed out that Γ_4 is zero in steady flow and that Γ_4 takes care of the starting vortex in unsteady flow.

Now, the evaluation of each term in the right-hand side of equation 2.4-6 has been presented in detail. Substituting equations 2.4-7, 2.4-10 and 2.4-11 into equation 2.4-6 gives the following expression for the pressure jump:

$$\Delta C_p = -2 \frac{G_i(t + \Delta t) - G_i(t)}{\Delta t} - 2\Delta \vec{V} \cdot (\vec{V}_m - \vec{V}_A - \vec{\omega} \times \vec{r}) \quad (2.4 - 26)$$

Equation 2.4-26 is used to compute the pressure jump across each element of the lifting surface. Actual computed pressure jumps, For example, will be shown next. In figure 13, a grid used to calculate the steady pressure jumps, ΔC_p , across a square planar lifting surface is shown. In figure 14, the actual computed ΔC_p at each control point for different heights of the trailing edge above the ground is shown. Each set of connected symbols corresponds to a spanwise row of control points. We note that in row 6, the row near the trailing edge, ΔC_p is very small for all cases, as the Kutta condition requires.

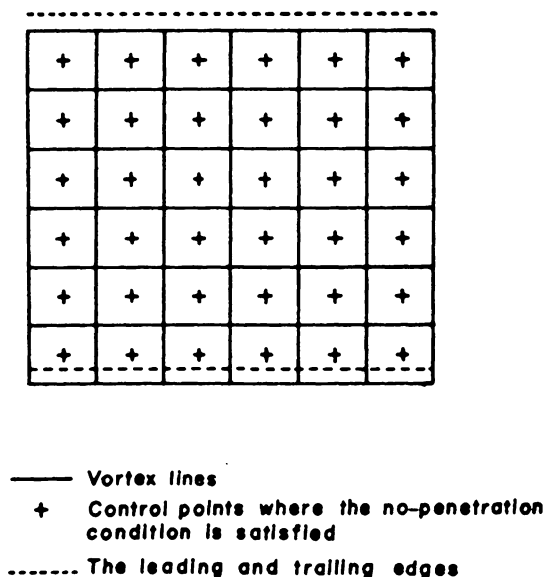


Figure 13. A grid used to compute pressure jumps across a rectangular wing of unit aspect ratio.

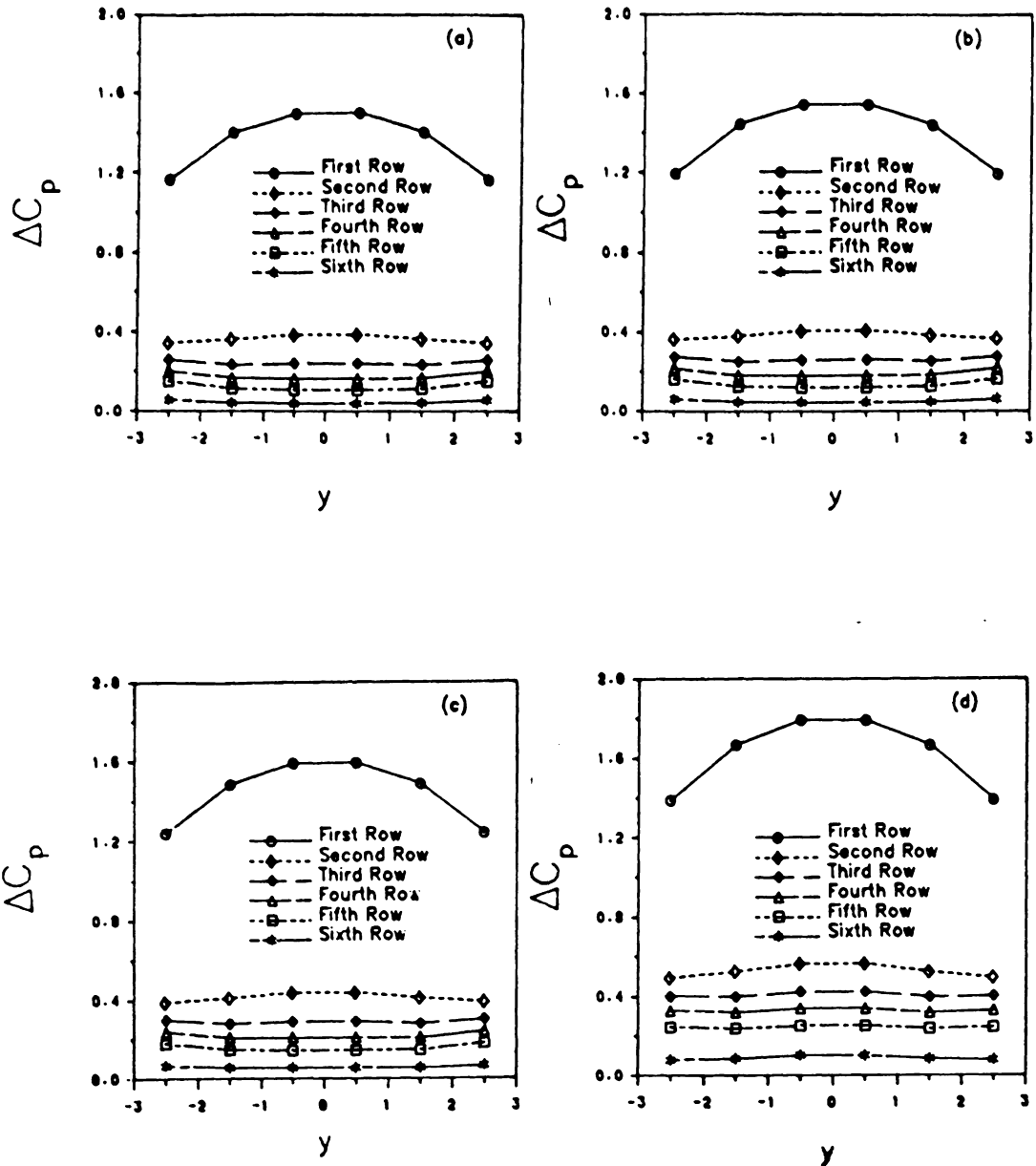


Figure 14. Pressure jumps across a rectangular wing of unit aspect ratio for steady flow: (a) ΔC_p for $H/C = \infty$ (far from the ground), (b) ΔC_p for $H/C = 0.66$, (c) ΔC_p for $H/C = 0.41$ and (d) ΔC_p for $H/C = 0.16$ at $\alpha = 10^\circ$ where H is the height of the trailing edge above the ground.

The elemental normal force, $(F_n)_i$, is found by multiplying the pressure jump, equation 2.4-26, by the elemental area, A_i , equation 2.4-20 or equation 2.4-24, that is

$$(F_n)_i = (\Delta C_p)_i A_i \quad (2.4 - 27)$$

The normal-force coefficient, C_n , is found from the following equation:

$$C_n = \frac{\sum_{i=1}^N (F_n)_i}{\sum_{i=1}^N (A)_i} \quad (2.4 - 28)$$

The elemental pitching moment, $(PM)_i$, is found by multiplying $(F_n)_i$ with distance from the leading edge to the control point of each element, r_{x_i} ; that is

$$(PM)_i = - (F_n)_i (r_{x_i}) \quad (2.4 - 29)$$

The pitching-moment coefficient, C_M , is found from the following equation:

$$C_M = \frac{\sum_{i=1}^N (PM)_i}{\sum_{i=1}^N (A)_i (\text{chord})} \quad (2.4 - 30)$$

The rolling and yawing moments are computed in a similar way.

2.5 Computation Procedure

2.5.1 Unsteady Ground Effect

The steady-state results are obtained by giving the wing an impulsive start and having it move forward at a constant velocity parallel to the ground plane. In the case of unsteady ground effects, the wing was initially located far from the ground, so that the flow reached a steady state while the wing descended along the flight path before it experiences the ground effect. For the computations, the sink rates were varied by varying the flight-path angle γ . In figure 15, a wing and its image near the ground are shown. The definition of the flight-path and pitch angles and how they are related to the angle of attack, α , are shown. The flight-path angle is related to the velocity of the wing by the following:

$$\gamma = \tan^{-1} \frac{V_{A_z}}{V_{A_x}} \quad (2.5 - 1)$$

in which V_{A_z} is the global velocity of the wing in the positive Z direction (downward) and V_{A_x} is the global velocity of the wing in the positive X direction. The magnitude of the wing velocity, $|\vec{V}_A|$, was chosen to be unity (see page 21), and hence $V_{A_x} = \cos \gamma$ and $V_{A_z} = \sin \gamma$. We refer to γ as the sink rate.

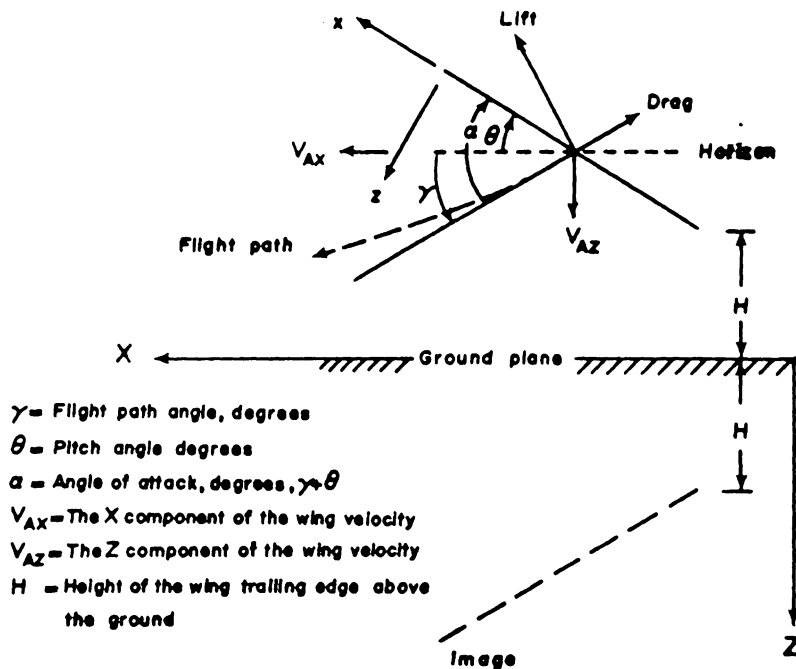


Figure 15. A side view of a wing and its image near the ground.

2.5.2 Velocity of Wind

The apparent free-stream velocity is defined by the following:

$$\vec{V}_{\infty} = -(\vec{V}_A - \vec{V}_{wind}) \quad (2.5 - 2)$$

in which \vec{V}_{wind} is the velocity of the wind. The velocity of the wind is parallel to the X-Y plane and makes an angle η with the X-axis. A wing in a cross wind is obtained by letting either $\eta = 90^\circ$ or $\eta = -90^\circ$, and a wing in head or tail wind is obtained by letting $\eta = 0^\circ$ or $\eta = 180^\circ$, respectively. The strength of the wind is specified as a percentage of the wing speed.

2.5.3 Flight Path

Three flight paths were used for studying the effect of the flight path on the aerodynamic characteristics of a wing. These flight paths are a sine wave, a parabola and a circular arc. The three flight paths will be derived next.

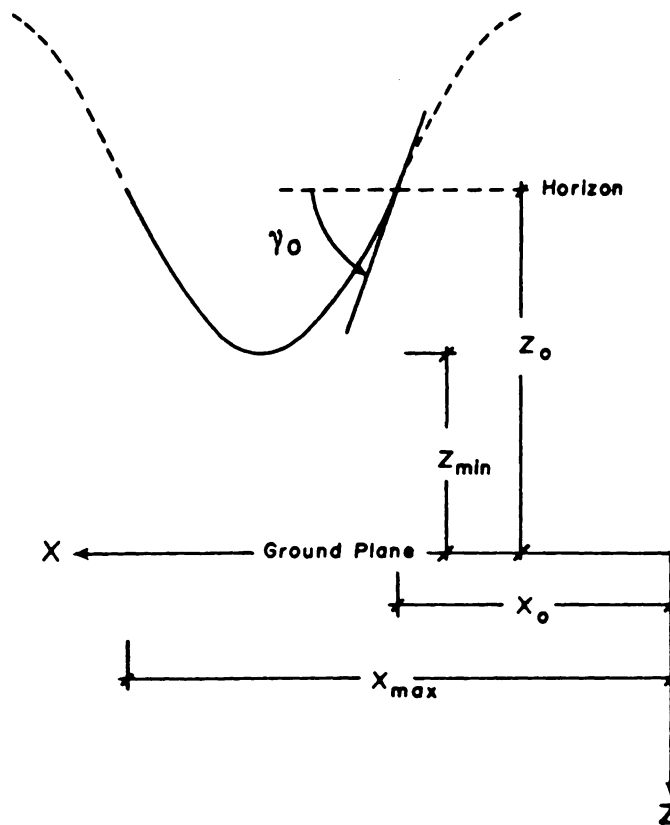


Figure 16. A sinusoidal flight path.

We start with the sine wave. In figure 16, a flight path is shown that is part of a sine wave. The equation describing this curve is given by the following:

$$Z = Z_0 - (Z_0 - Z_{min}) \sin \frac{\pi(X - X_0)}{X_{max} - X_0} \quad (2.5 - 3)$$

In which Z_0 , Z_{min} , X_0 and X_{max} are shown in figure 16. Taking the derivative of equation 2.5-3 with respect to X , one finds that

$$\frac{dZ}{dX} = \tan \gamma = - \frac{\pi(Z_0 - Z_{min})}{X_{max} - X_0} \cos \frac{\pi(X - X_0)}{X_{max} - X_0} \quad (2.5 - 4)$$

Substituting $X = X_0$ and $\gamma_0 = \gamma_0$ into equation 2.5-4, leads to the following

$$\frac{\pi}{X_{max} - X_0} = - \frac{\tan \gamma}{Z_0 - Z_{min}} \quad (2.5 - 5)$$

Substituting equation 2.5-5 into equation 2.5-4 leads to the following

$$\tan \gamma = \tan \gamma_0 \cos \frac{(X - X_0) \tan \gamma_0}{Z_0 - X_{min}} \quad (2.5 - 6)$$

Equation 2.5-6 describes the flight-path angle, γ , as a function of X for a sinusoidal flight path.

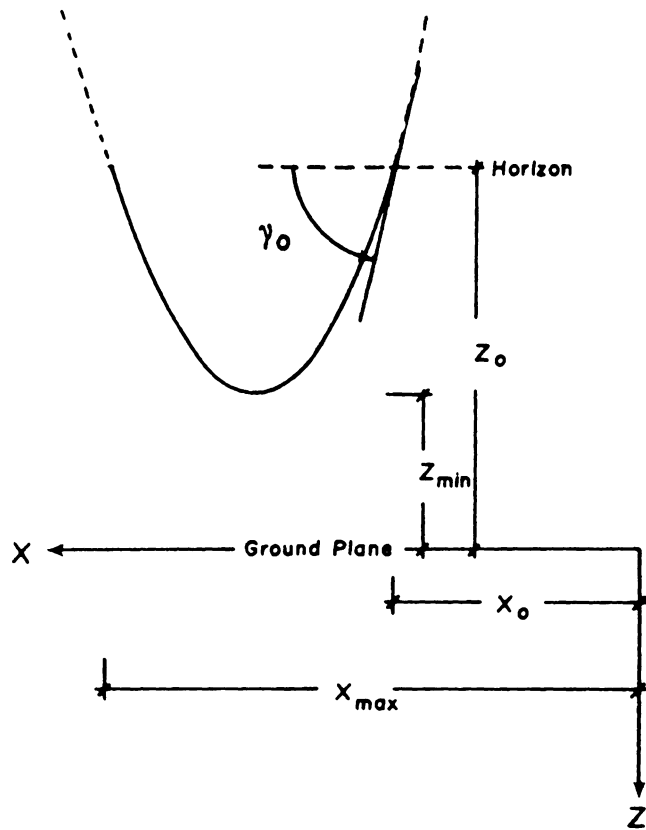


Figure 17. A parabolic flight path.

In figure 17, a flight path is shown that is part of a parabola. The equation describing this curve is given by the following:

$$Z = Z_{\min} - K \left[X - \frac{X_{\max} + X_0}{2} \right]^2 \quad (2.5 - 7)$$

in which K is a constant. K is found from equation 2.5-7 by substituting $X = X_0$ and $Z = Z_0$; that is,

$$K = - \frac{4(Z_0 - Z_{\min})}{(X_{\max} - X_0)^2} \quad (2.5 - 8)$$

Taking The derivative of equation 2.5-7 with respect to X, one finds

$$\tan \gamma = -2K \left[X - \frac{X_{\max} + X_0}{2} \right] \quad (2.5 - 9)$$

K is found from equation 2.5-9 by substituting $X = X_0$, that is

$$K = \frac{\tan \gamma_0}{X_{\max} - X_0} \quad (2.5 - 10)$$

Equating equation 2.5-8 to equation 2.5-10, on finds the following:

$$X_{\max} = X_0 - \frac{2(Z_0 - z_{\min})}{\tan \gamma_0} \quad (2.5 - 11)$$

Substituting equations 2.5-10 and 2.5-11 into equation 2.5-9, one obtains the following

$$\tan \gamma = \tan \gamma_0 \left[\frac{(X - X_0) \tan \gamma_0}{2(Z_0 - Z_{\min})} + 1 \right] \quad (2.5 - 12)$$

Equation 2.5-12 describes the flight-path angle, γ , as a function of X for a parabolic flight path.

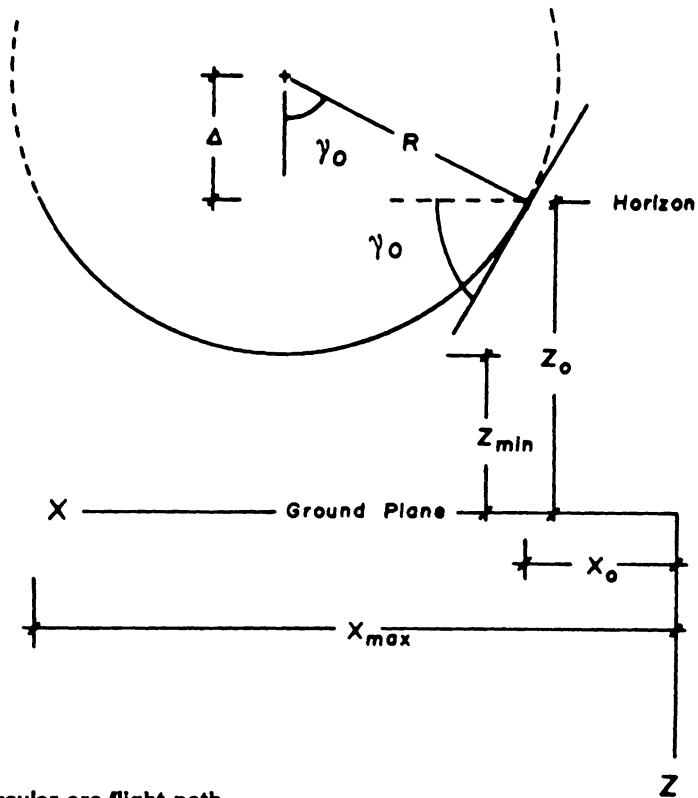


Figure 18. A circular-arc flight path.

In figure 18, a flight path is shown that is part of a circle. The equation describing this curve is given by the following:

$$[Z - (Z_0 - \Delta)]^2 + \left[X - \frac{(X_{\max} + X_0)}{2}\right]^2 = [Z_0 - Z_{\min} - \Delta]^2 \quad (2.5 - 13)$$

in which Δ is a positive number (see figure 18). Δ is given by

$$\Delta = R - |Z_0 - Z_{\min}| \quad (2.5 - 14)$$

in which R is the radius of the circle. Because $Z_0 - Z_{\min} < 0$, equation 2.5-14 becomes

$$\Delta = R + (Z_0 - Z_{\min}) \quad (2.5 - 15)$$

The radius, R, is given by

$$R = \frac{\Delta}{\cos \gamma_0} \quad (2.5 - 16)$$

From equations 2.5-15 and 2.5-16, Δ is found as

$$\Delta = - \frac{(Z_0 - Z_{min}) \cos \gamma_0}{1 - \cos \gamma_0} \quad (2.5 - 17)$$

Taking the derivative of equation 2.5-13 with respect to X, one finds the following

$$\tan \gamma = \frac{X - \frac{X_{max} + X_0}{2}}{Z - Z_0 + \Delta} \quad (2.5 - 18)$$

$\frac{X_{max} + X_0}{2}$ is found from equation 2.5-18 by substituting $X = X_0$, $Z = Z_0$ and $\gamma = \gamma_0$. The result is the following:

$$\frac{X_{max} + X_0}{2} = - \Delta \tan \gamma_0 + X_0 \quad (2.5 - 19)$$

Substituting equation 2.5-19 into equation 2.5-18 yields the following:

$$\tan \gamma = \frac{X - X_0 + \Delta \tan \gamma_0}{Z - Z_0 + \Delta} \quad (2.5 - 20)$$

Equations 2.5-17 and 2.5-20 describe the flight-path angle, γ , as functions of X and Z for a circular flight path.

Initially, the flight path is chosen to be straight, so that the flow would reach a steady state before the wing experiences the curvature effect.

Chapter III

Numerical Examples

3.1 *General*

A general unsteady aerodynamic model was described in chapter II. The capability of the model to predict aerodynamic forces and moments is shown in this chapter. This is done by studying wings in steady and unsteady ground effects. Some of the computed results were published by Nuhait and Mook (1988).

As a means of establishing the credibility of the numerical model, we first use it to compute the steady ground effects for a series of circular-arc airfoils. These results are compared with an exact solution found by Tomotika et al. (1951b). The comparison is done in section 3.2. In section 3.3, the effect of the ground on the wakes of three wings is shown. A comparison of the computed and experimental results in steady flow for an F-104A wing is presented in section 3.4. Computed results are shown for flat rectangular wings in section 3.5 and for rectangular wings

with dihedral angles in section 3.6. Numerical results for swept wings are presented in section 3.7. Numerical results for delta wings in steady and unsteady flows and some comparisons with experimental results are given in section 3.8. In addition, the effects of sink rate and aspect ratio are shown. The effects of cross and/or head winds and of flight-path shapes are presented in sections 3.9 and 3.10, respectively. Concluding remarks are given in section 3.11.

3.2 *Two-Dimensional Airfoils*

The vortex-lattice technique is used to investigate the steady ground effect on two-dimensional circular-arc airfoils with various cambers. The results are compared with an exact solution found by Tomotika et al. (1951b). The exact and computed lift and pitching-moment (about the trailing edge) increments are plotted as functions of height above the ground. The angle of attack is always five degrees. The results for the flat plate (zero camber) are shown in figure 19. The agreement is excellent. The results of the circular-arc airfoil with 0.022, 0.053 and 0.097 cambers are shown in figures 20, 21 and 22, respectively. For camber, the agreement is excellent too. It is clear, as shown in figure 19, that the ground effect first slightly lowers the lift and moment and then increases them as the flat plate approaches the ground. From figures 19 to 22, it is clear that the effect of the ground on the lift and moment of an airfoil is greatly modified by its camber. Thus, the ground effect first lowers the lift and moment and then raises them as the airfoil approaches the ground. As the camber becomes larger, this trend grows stronger, and for the last case there is essentially only a loss in lift and moment.

The vortex-lattice method is not restricted to two-dimensional steady flows, as the analysis of Tomotika et al. is. Below, we show the effect of finite aspect ratio for wings in steady and unsteady ground effect.

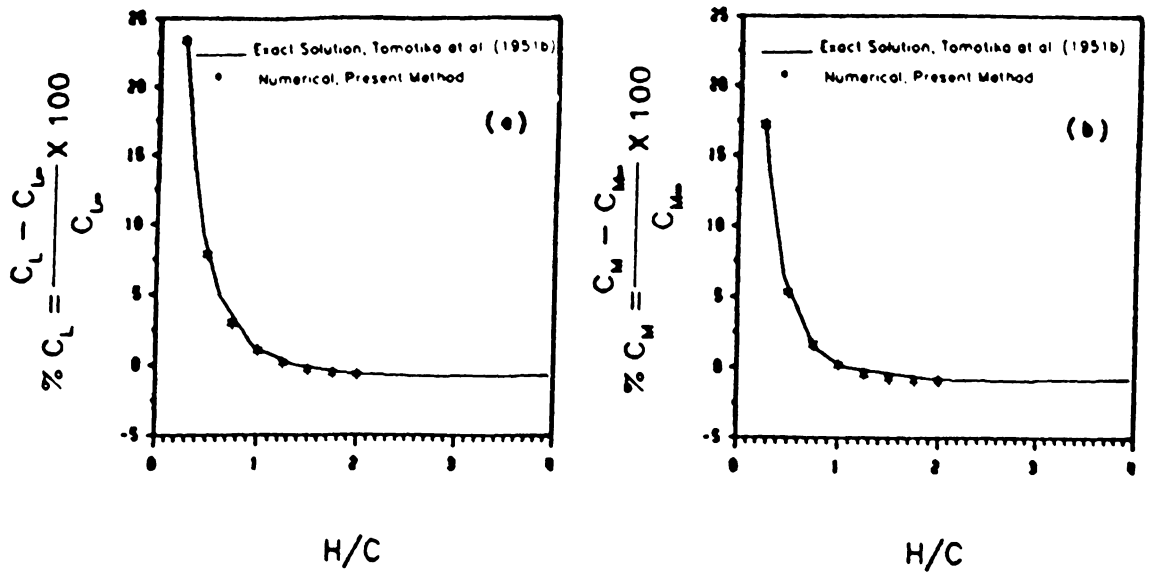


Figure 19. A two-dimensional flat plate wing in a steady ground effect: (a) lift and (b) pitching-moment (about the trailing edge) coefficients as functions of height of the trailing edge above the ground at $\alpha = 5^\circ$.

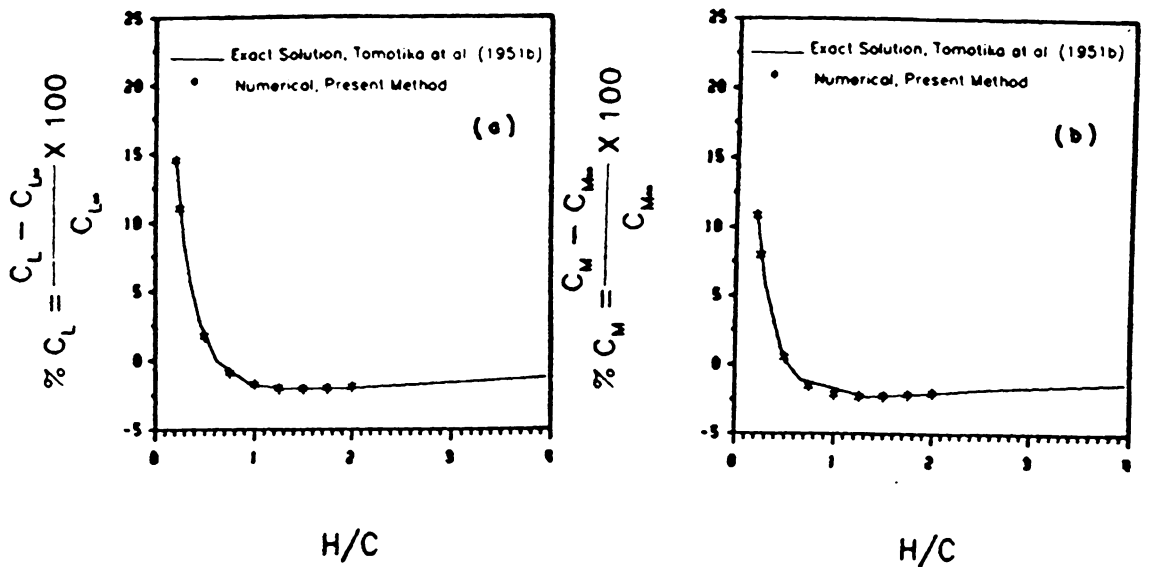


Figure 20. A two-dimensional circular-arc airfoil (camber = 0.022) in a steady ground effect: (a) lift and (b) pitching-moment (about the trailing edge) coefficients as functions of height of the trailing edge above the ground at $\alpha = 5^\circ$.

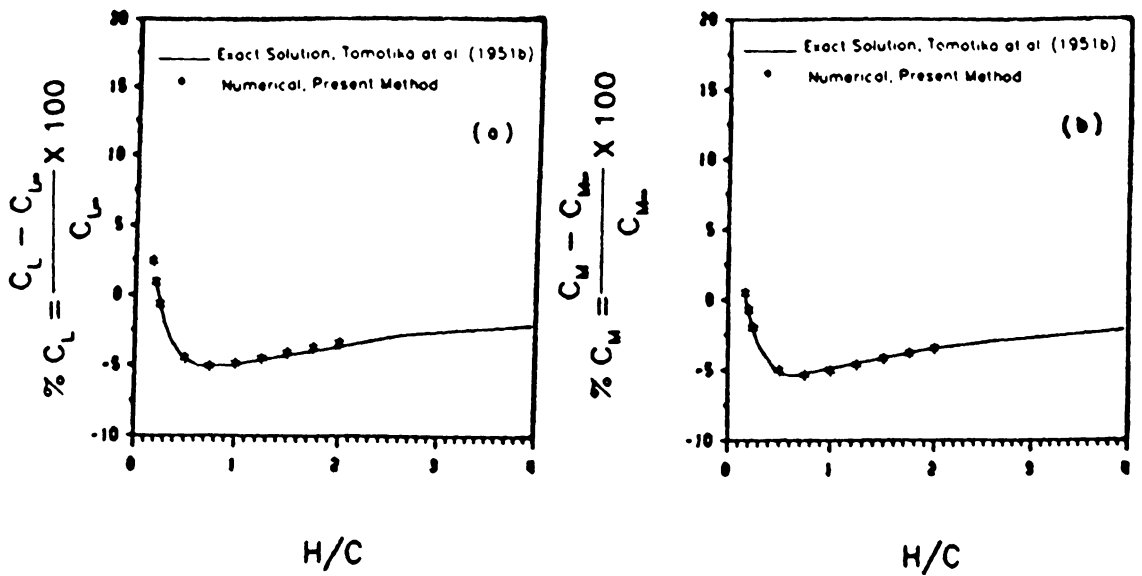


Figure 21. A two-dimensional circular-arc airfoil (camber = 0.053) in a steady ground effect: (a) lift and (b) pitching-moment (about the trailing edge) coefficients as functions of height of the trailing edge above the ground at $\alpha = 5^\circ$.

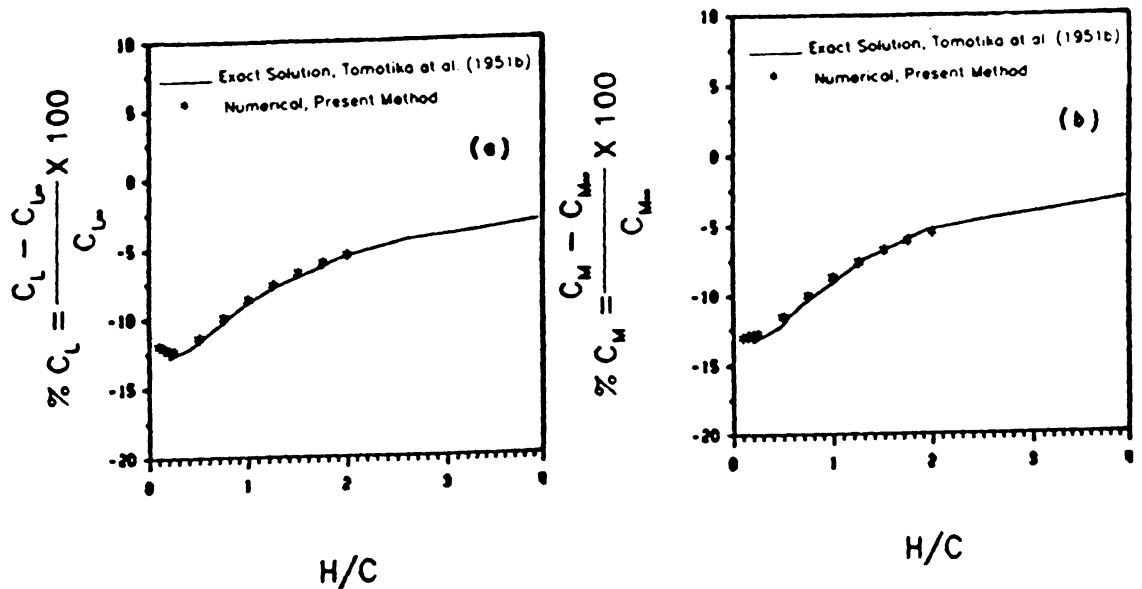


Figure 22. A two-dimensional circular-arc airfoil (camber = 0.097) in a steady ground effect: (a) lift and (b) pitching-moment (about the trailing edge) coefficients as functions of height of the trailing edge above the ground at $\alpha = 5^\circ$.

3.3 Wake Plots

All the results, even those for the steady states, are computed by a general unsteady algorithm. At each time step, a vortex is formed along the sharp edges where the Kutta condition is imposed in a steady flow. These vortices are shed and convected at the local fluid velocity to form the wake. Thus, the distribution of the vorticity in, and the shape of, the wake are predicted as part of the solution. In figure 23, computed wakes are shown. In part (a) the top views of a low aspect ratio tapered wing ($AR = 1.9$) are shown in and out of ground effect. The corresponding side views are shown in part (b). The angle of attack is 10° and the flow is steady. Similar results are shown in figure 24 for a moderate aspect ratio tapered wing ($AR = 3.8$). The horizontal line below the wing in part (b) of both figures shows the position of the ground for the ground-effect case; it is also included in the results for the out-of-ground-effect case for comparison. Clearly, the effect of the ground restricts the downward movement of the wake and causes it spread. As a result, the wake effects (downwash) will be weaker and in turn the effective angle of attack is higher; this is one of the factors that cause lift to increase. In figure 25, plots of computed wakes in and out-of ground effects for a delta wing of aspect ratio 1.5 at 10° angle of attack are shown. In parts (a), (b) and (c) the top, side and front views are shown, respectively. Clearly, the effect of the ground restricts the downward movement of the wake and causes it spread. This ground effect appears to be stronger for delta wings than for the wings considered previously.

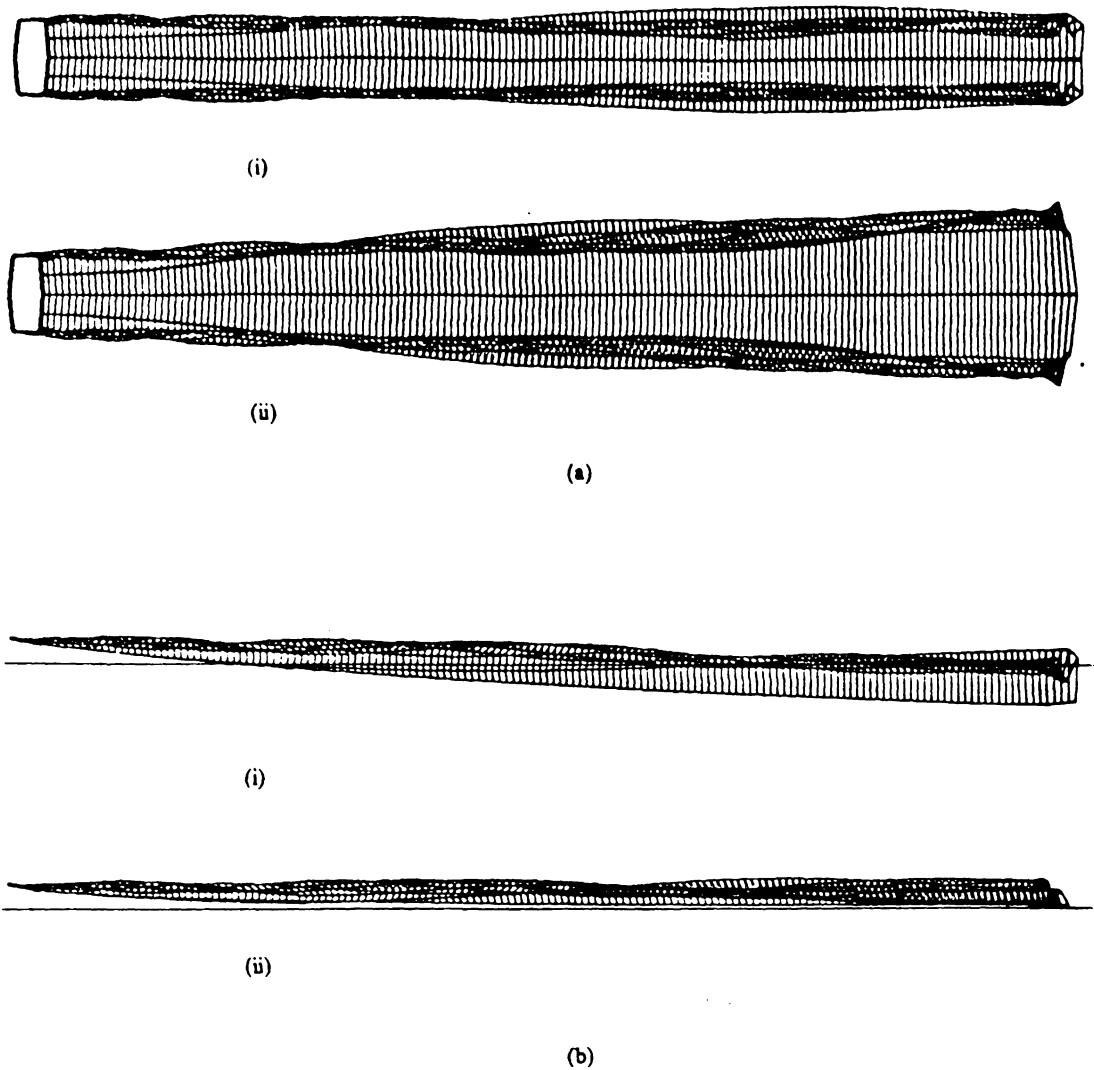


Figure 23. Actual computed wakes for a low-aspect-ratio tapered wing ($AR = 1.9$) in and out of ground effect for steady flow: part (a) top views; (i) out of ground effect and (ii) in ground effect. Part (b) side views; (i) out of ground effect and (ii) in ground effect. $\alpha = 10^\circ$.

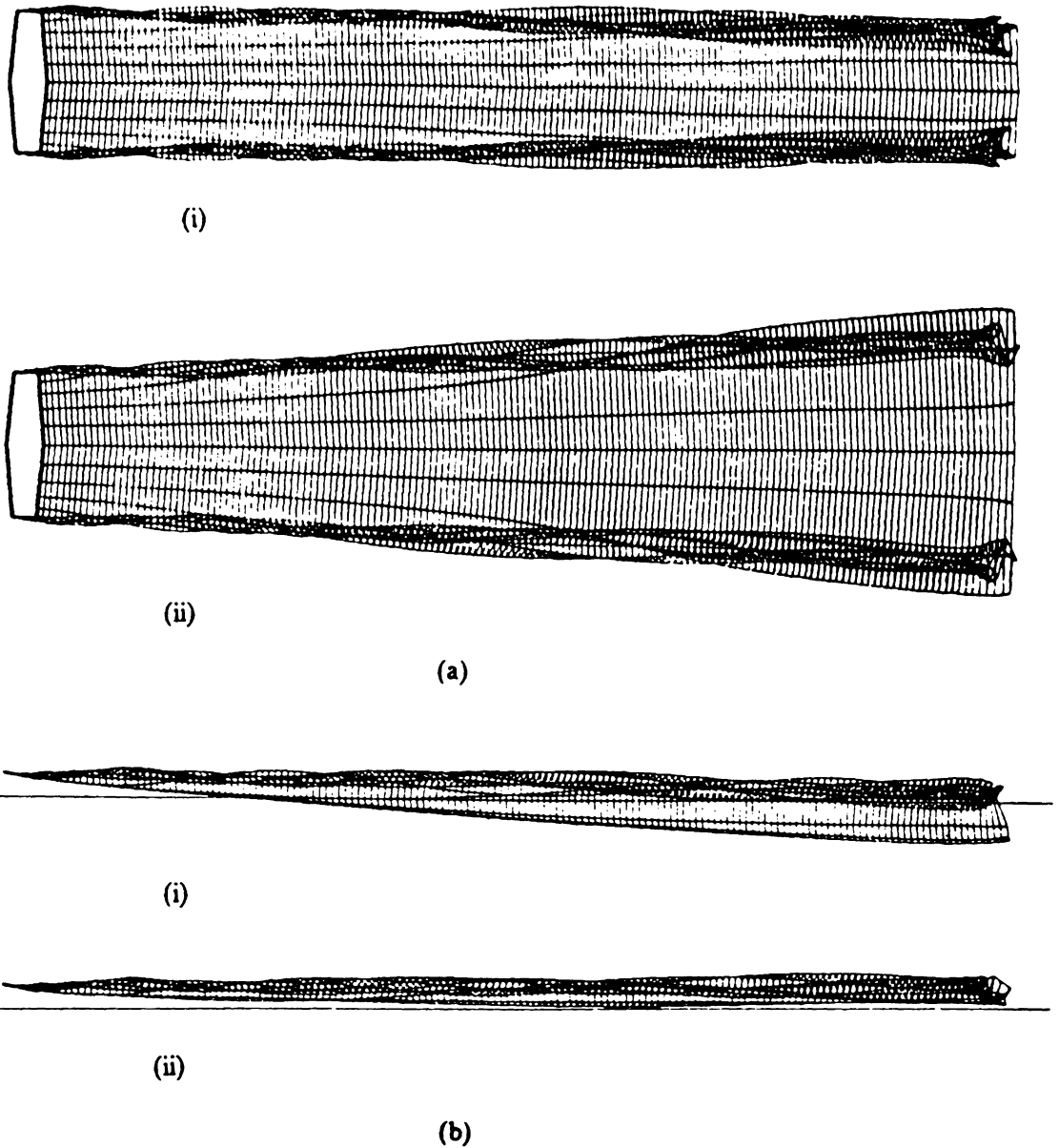
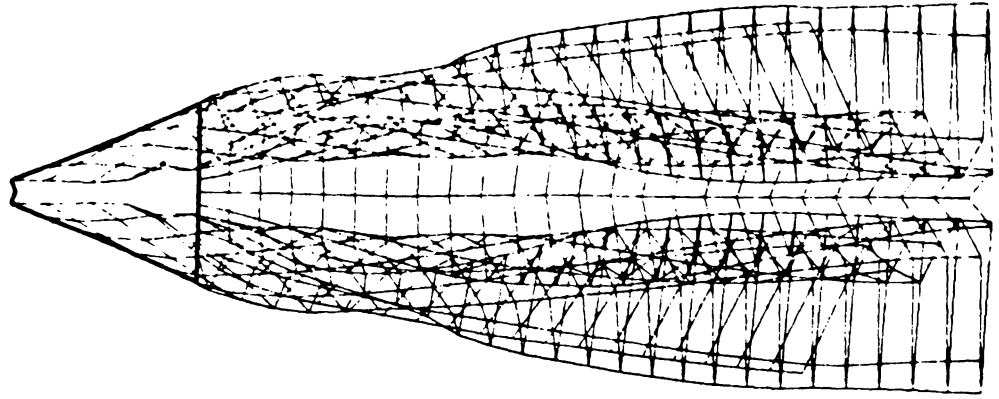
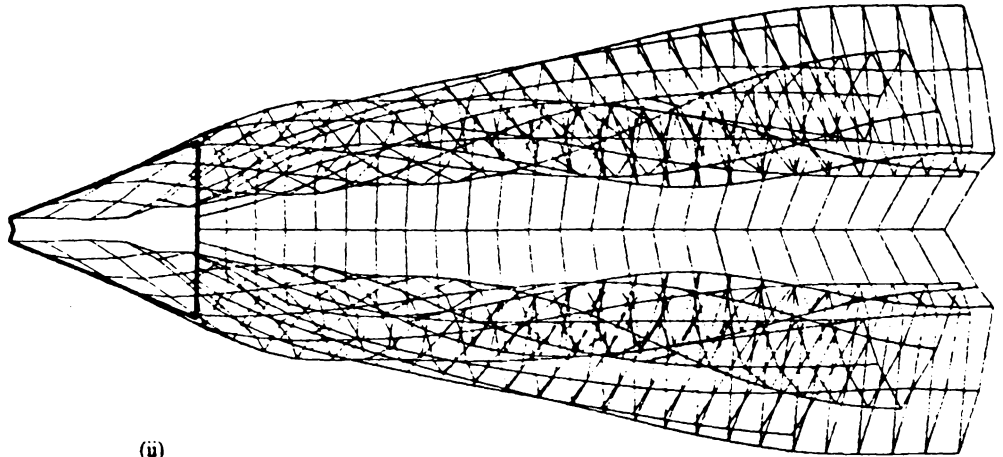


Figure 24. Actual computed wakes for a low-aspect-ratio tapered wing ($AR = 3.8$) in and out of ground effect for steady flow: part (a) top views; (i) out of ground effect and (ii) in ground effect. Part (b) side views; (i) out of ground effect and (ii) in ground effect. $\alpha = 10^\circ$.



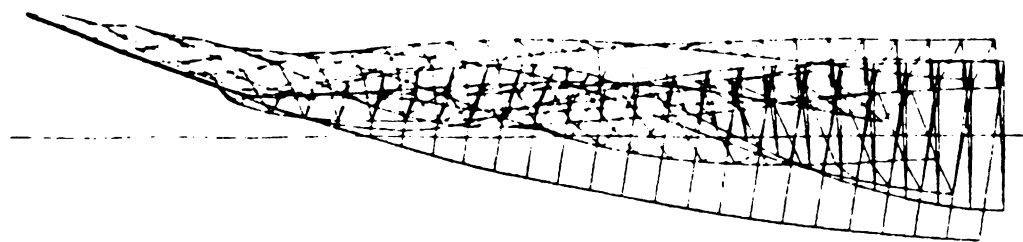
(i)



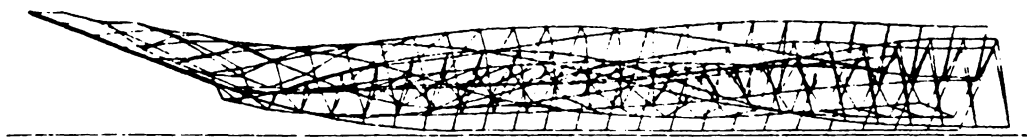
(ii)

(a)

Figure 25. Actual computed wakes for a delta wing ($AR = 1.5$) in and out of ground effect for steady flow: part (a) top views; (i) out of ground effect and (ii) in ground effect. Part (b) side views; (i) out of ground effect and (ii) in ground effect. Part (c) side views; (i) out of ground effect and (ii) in ground effect. $\alpha = 10^\circ$.

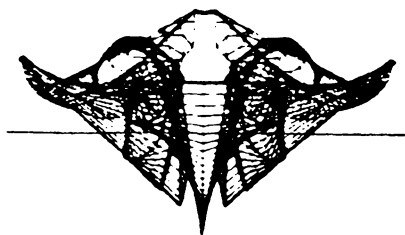


(i)

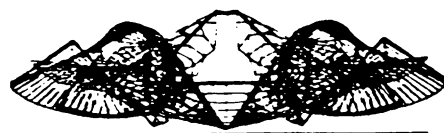


(ii)

(b)



(i)



(ii)

(c)

Figure 25. Continued

3.4 Tapered Wing

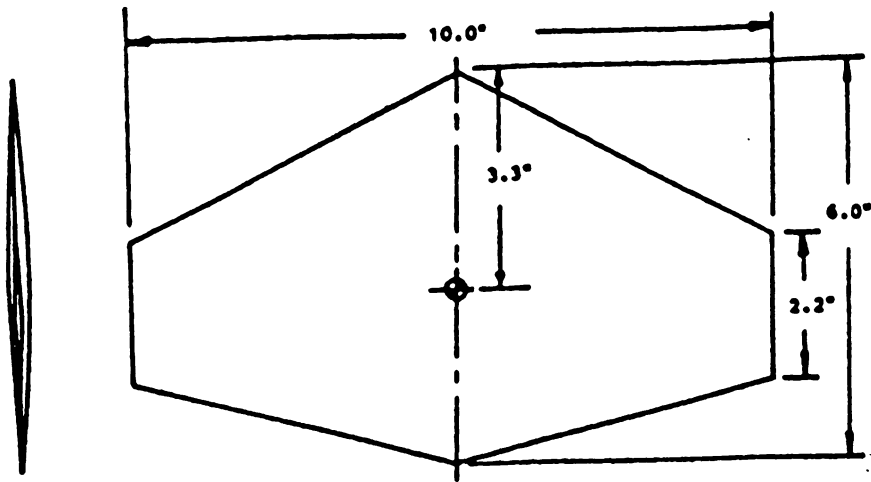


Figure 26. Dimension of the model of an F-104A wing: tested by Chang and Muirhead (1985).

In figure 26, there is a sketch of a model of an F-104A wing taken from Chang and Muirhead (1985). In figure 27, plots of the aerodynamic coefficients in and out of ground effect are given for this model. In each plot the computed results are compared with the experimental data of Chang (1985). The height above the ground divided by the span ($\frac{h}{b}$) is equal to 0.28 for the case near the ground, where h is measured to a point 3.3 inches behind the apex. In parts (a) and (b), the lift coefficients as functions of angle of attack are shown out of and in ground effect, respectively. The agreement is good up to approximately 10 degrees angle of attack. Beyond 10 degrees, the data seem to show that stall occurs in both cases. In parts (c) and (d), lift coefficients are plotted as functions of the drag coefficients for out of and in ground effect, respectively. Both plots show good agreement with experimental results. In part (e), the lift coefficients are plotted as functions of

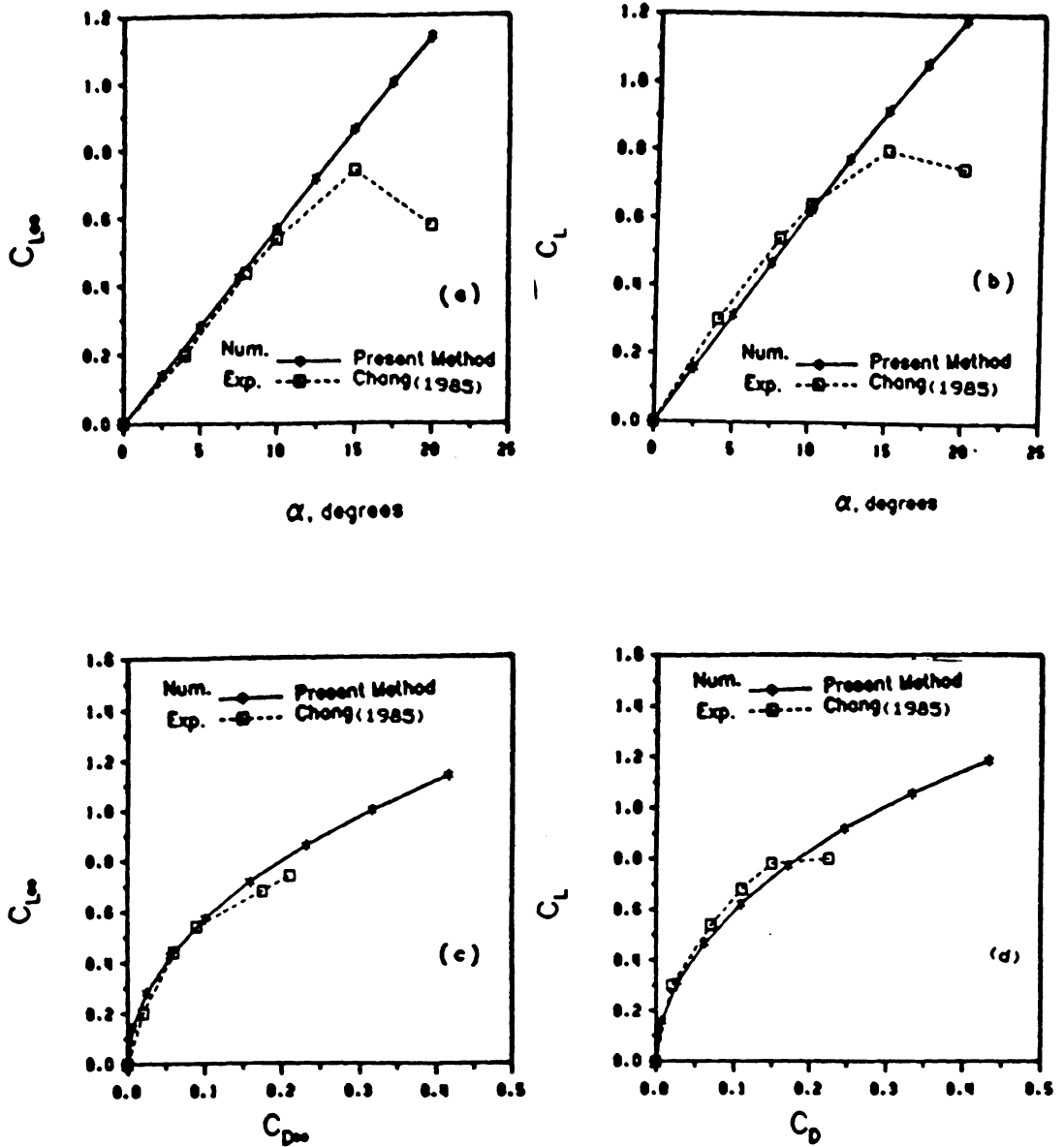


Figure 27. A comparison of the computed and experimental results in steady flow for an F-104A wing: parts (a) and (b) lift coefficients for out of and in ground effect as functions of angle of attack, respectively. Parts (c) and (d) lift coefficients for out of and in ground effect as functions of drag coefficients, respectively. Parts (e) and (f) lift coefficients for out of and in ground effect as functions of pitching-moment coefficients, respectively. For the case near the ground, $h/b = 0.28$ where h is the height above the ground of a point 3.3 inches behind the apex.

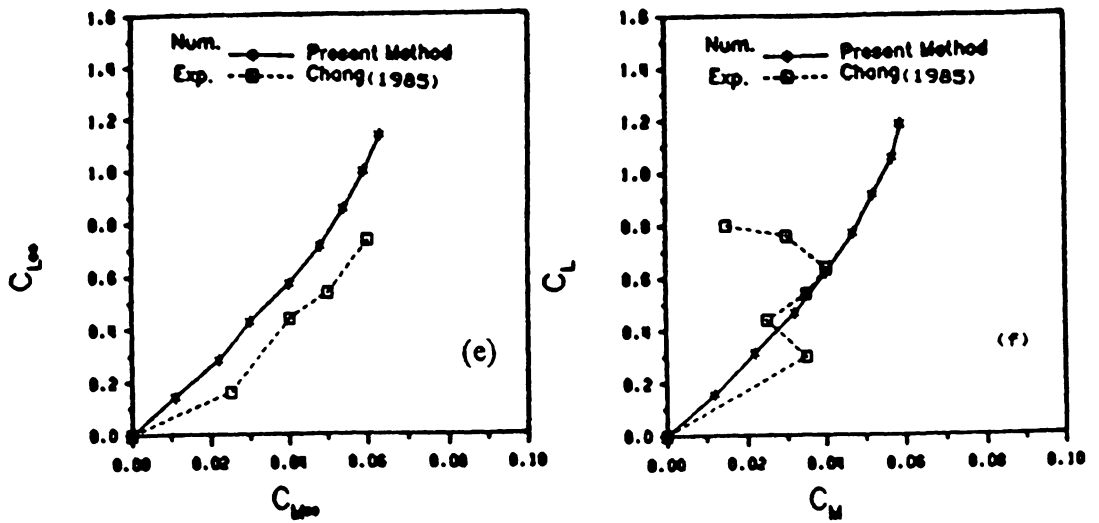


Figure 27. Continued

pitching moment coefficients far from the ground. The trends for both curves are the same. The disagreement could be caused by taking the moment at different points. Near the ground, part (f), there seems to be a problem with the experimental data.

3.5 Flat Rectangular Wings

In figure 28, the percentage changes in the aerodynamic coefficients are given as functions of the height of the trailing edge above the ground for different sink rates for a rectangular wing. The angle of attack is 10 degrees and the aspect ratio is unity. It is clear that the proximity of the ground increases all the aerodynamic coefficients and that this effect is stronger for higher sink rates. This trend was also noticed for aspect ratios 2 and 4.

In figure 29, the percentage changes in the lift coefficient are given as functions of the height of the trailing edge above the ground for different sink rates for a rectangular wing. The angle of attack is -10 degrees and the aspect ratio is unity. It is clear that the proximity of the ground increases all the aerodynamic coefficients and that this effect is stronger for higher sink rates.

In figure 30, the percentage changes in the aerodynamic coefficients are given as functions of the height of the trailing edge above the ground for different aspect ratios for unsteady flow ($\gamma = 20^\circ$). The angle of attack is 10 degrees. It is clear that the ground increases all coefficients and that these effects are stronger for larger aspect ratios. Also, it is clear that the wings with larger aspect ratios feel the ground at higher positions. The same trend was also noticed for sink rates $\gamma = 10^\circ$ and $\gamma = 0^\circ$ (steady).

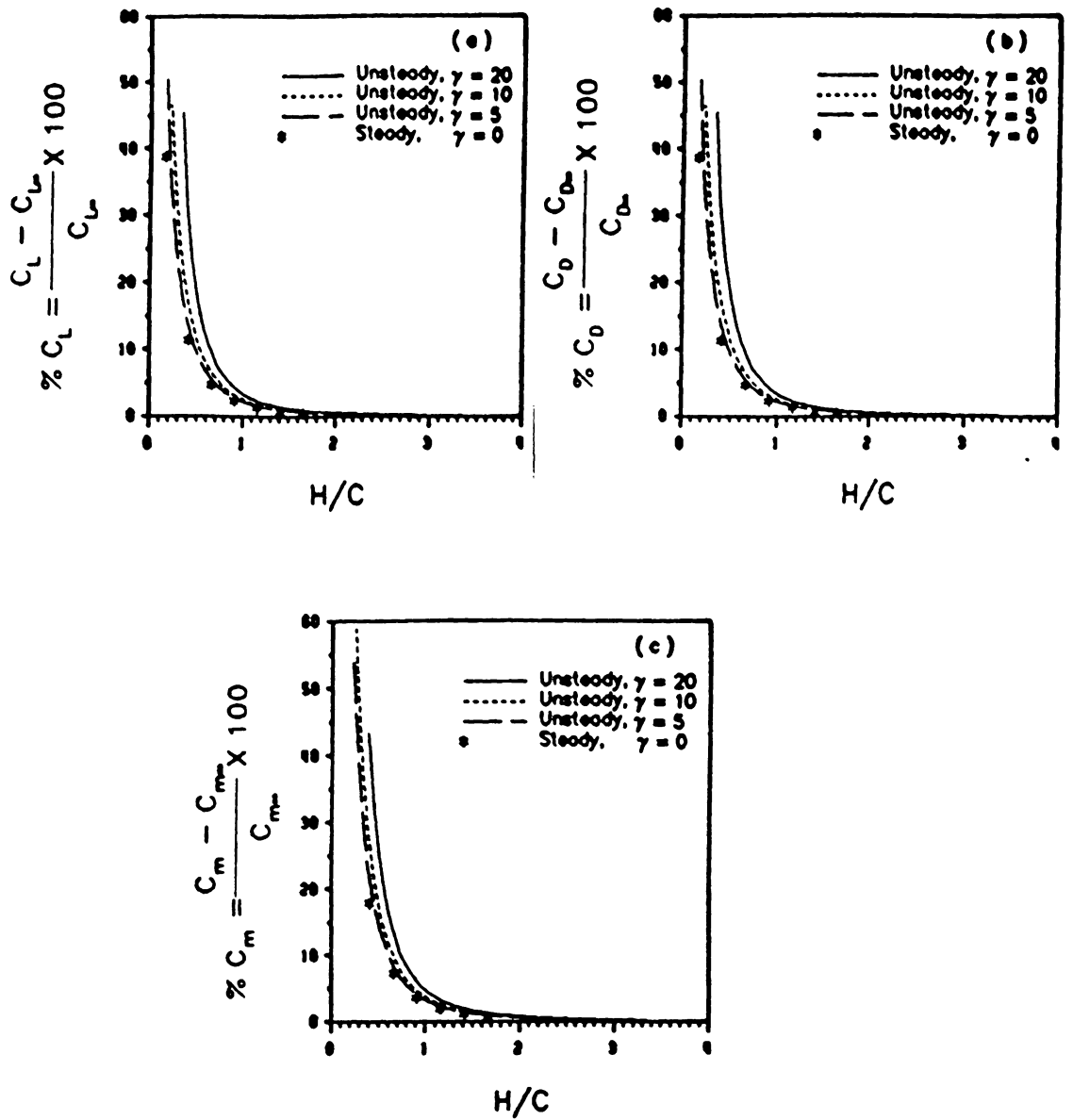


Figure 28. Computed results for a rectangular wing of unit aspect ratio in ground effect: (a) lift, (b) drag and (c) pitching-moment increments as functions of the height of the trailing edge above the ground for different sink rate (see figure 15 for the definition of γ). $\alpha = 10^\circ$.

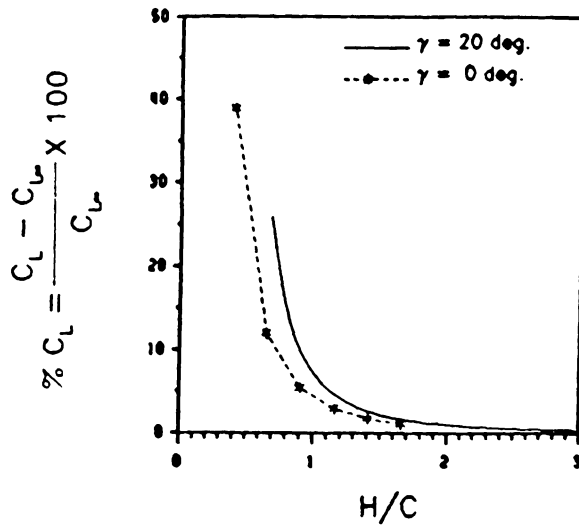


Figure 29. Computed results for a rectangular wing of unit aspect ratio in ground effect: lift increment as functions of the height of the trailing edge above the ground for different sink rate (see figure 15 for the definition of γ). $\alpha = -10^\circ$.

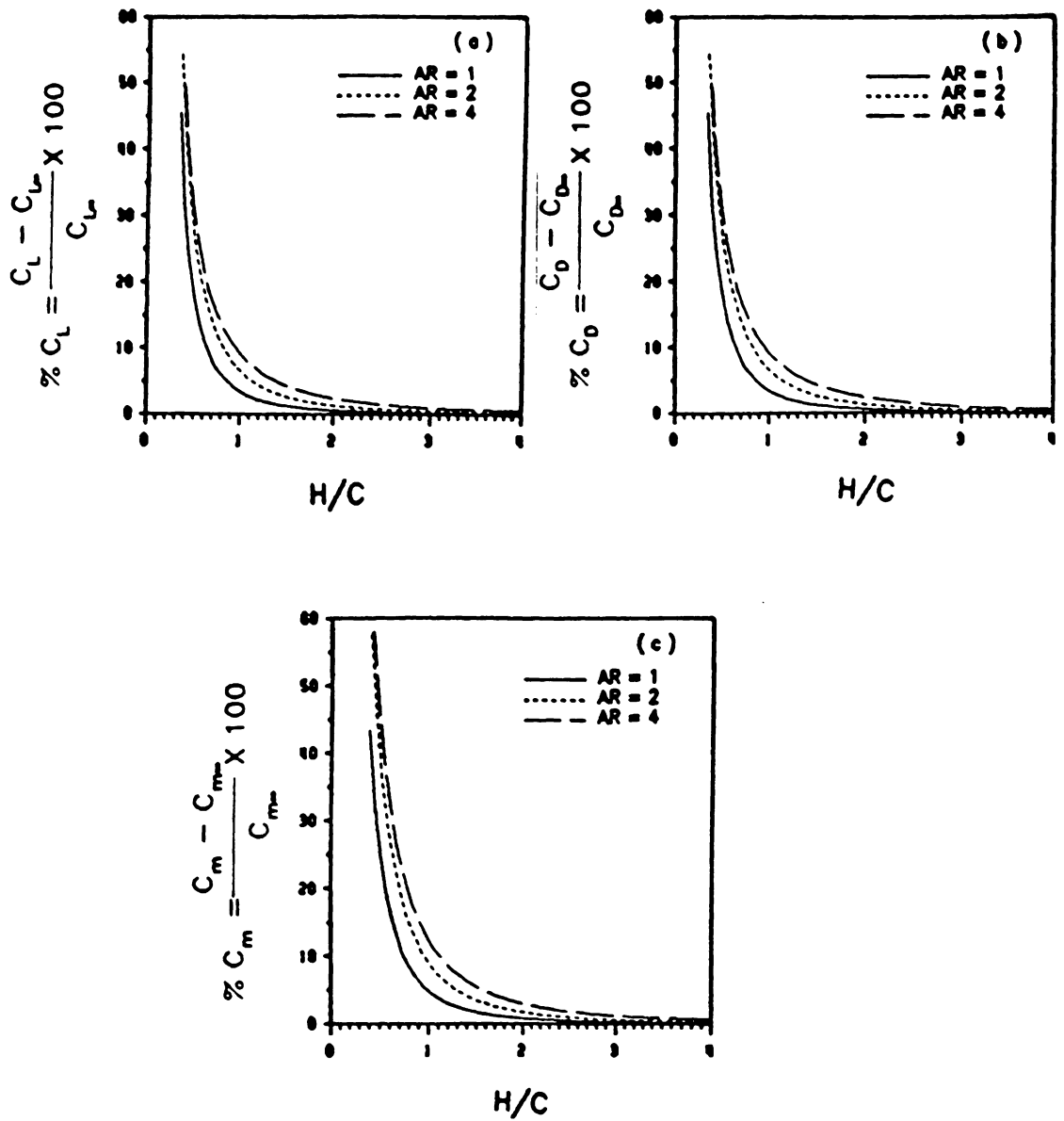


Figure 30. Computed results for a rectangular wing of unit aspect ratio in ground effect: (a) lift, (b) drag and (c) pitching-moment increments as functions of the height of the trailing edge above the ground for unsteady flow, $\gamma = 20^\circ$ (see figure 15 for the definition of γ). $\alpha = 10^\circ$.

3.6 Rectangular Wings with Dihedral Angles

In figure 31, the percentage changes in the aerodynamic coefficients are given as functions of the height of the trailing edge at the root chord above the ground for different sink rates. The angle of attack is 10 degrees, the aspect ratio is 4, and the dihedral angle is five degrees. It is clear that the proximity of the ground increases all coefficients and that this effect is stronger for larger sink rates. But as the next sets of results shows, the dihedral angle reduces the ground effects. In figure 32, similar plots for different dihedral angles for unsteady flow ($\gamma = 20^\circ$) are presented. The angle of attack is 10 degrees. It is clear that the ground effect increases all coefficients but this trend is weaker for higher dihedral angles. The same trend was also noticed for sink rates $\gamma = 10^\circ$ and $\gamma = 0^\circ$.

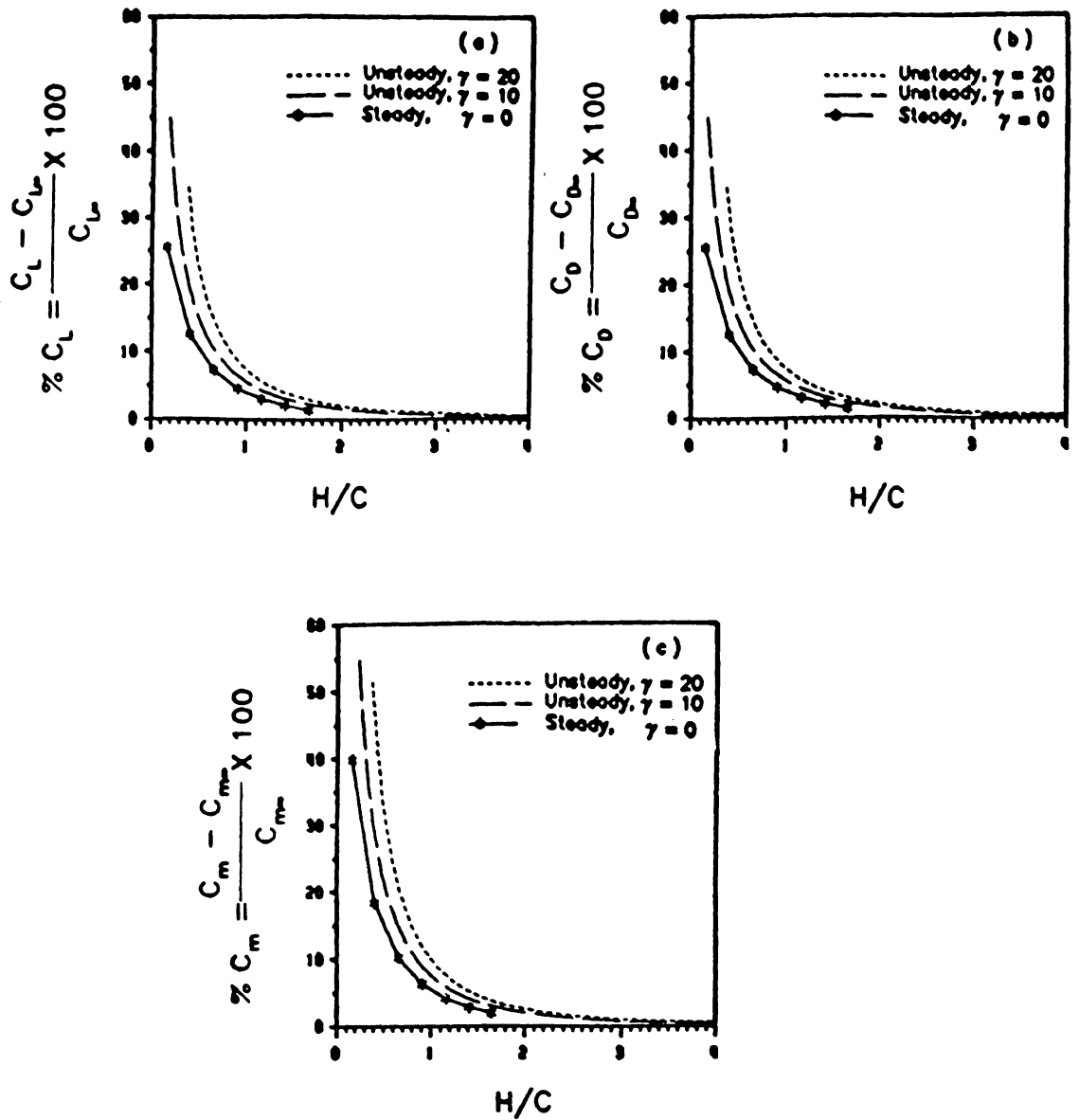


Figure 31. Computed results for a rectangular wing of aspect ratio 4 in ground effect: (a) lift, (b) drag and (c) pitching-moment increments as functions of the height of the trailing edge above the ground for different sink rate. $\alpha = 10^\circ$ and $\Gamma = 5^\circ$.

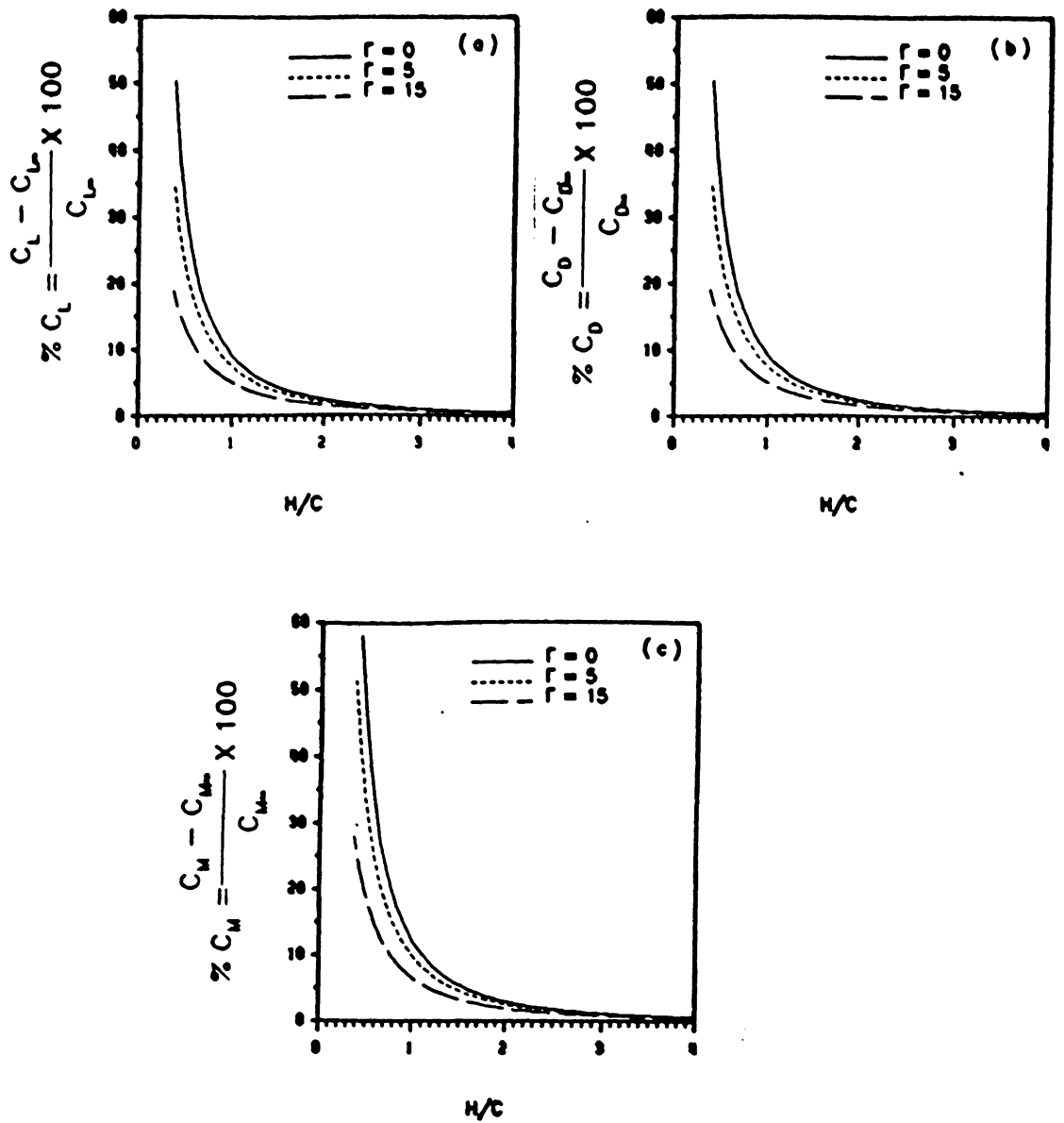


Figure 32. Computed results for a rectangular wing of aspect ratio 4 in ground effect for unsteady flow: (a) lift, (b) drag and (c) pitching-moment increments as functions of the height of the trailing edge above the ground for different dihedral angles. $\alpha = 10^\circ$ and $\gamma = 20^\circ$.

3.7 Swept Wings

In figure 33, the percentage changes in the aerodynamic coefficients are given as functions of the height of the trailing edge at the root chord above the ground for different sink rates. The angle of attack is 10 degrees, the aspect ratio is 4 and the sweep-back angle is 45 degrees. It is clear that the proximity of the ground increases all coefficients, but the ground effect is nearly the same for all sink rates, which means that unsteady ground effects can be predicted by a steady analysis.

In figure 34, the percentage changes in the aerodynamic coefficients are presented as functions of the height of the trailing edge at the root chord above the ground for different sweep-back angles for steady flow, ($\gamma = 0^\circ$). The angle of attack is 10 degrees and the aspect ratio is 4. Clearly, the proximity of the ground increases all coefficients and this effect is the same for all sweep-back angles. Similar results are shown in figure 35 for unsteady flow, ($\gamma = 20^\circ$). Clearly, the proximity of the ground increases all coefficients and this effect is weaker for larger sweep-back angles. The same trend was also noticed for sink rate $\gamma = 10^\circ$.

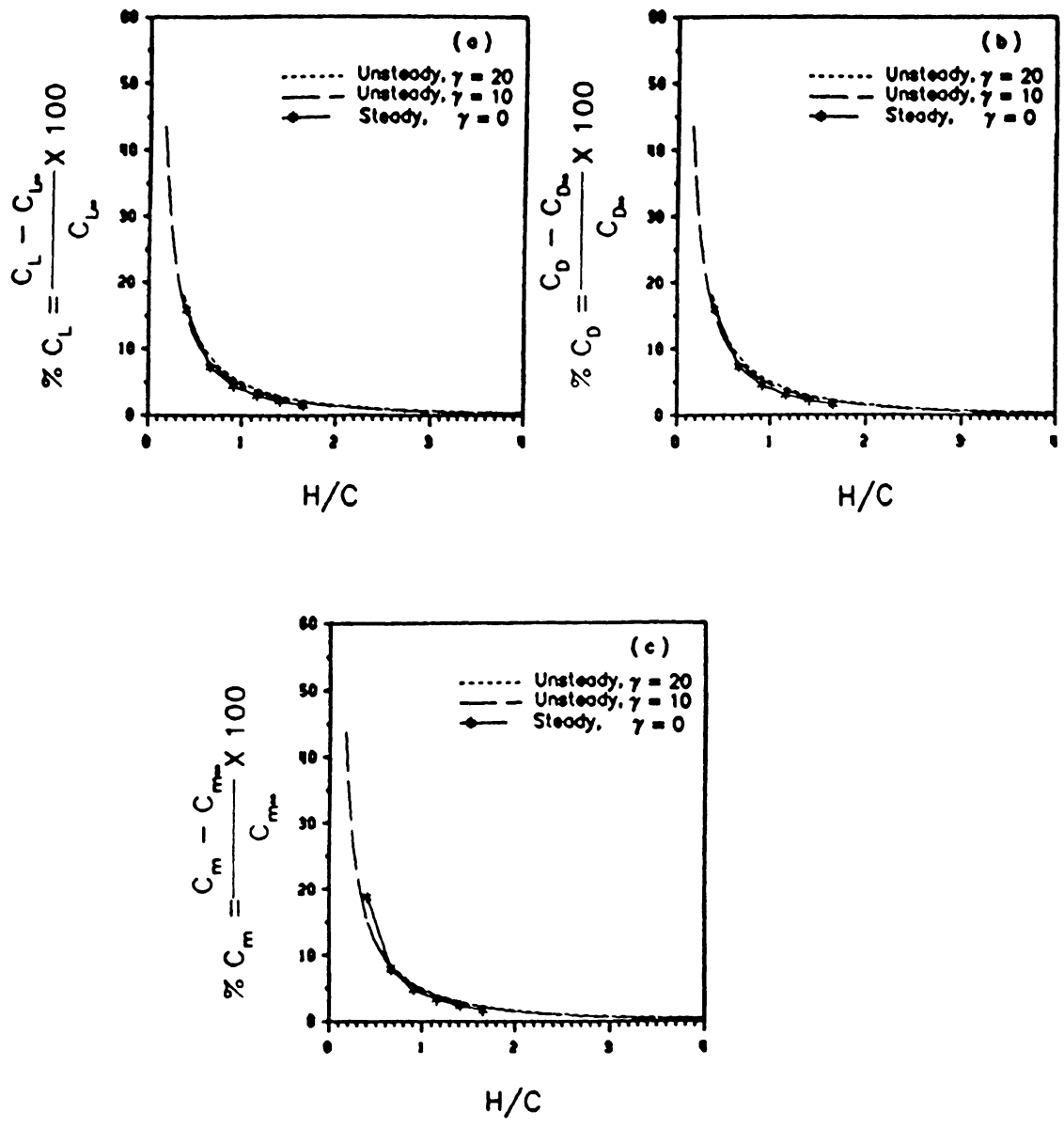


Figure 33. Computed results for a swept wing of aspect ratio 4 in ground effect: (a) lift, (b) drag and (c) pitching-moment increments as functions of the height of the trailing edge above the ground for different sink rate. $\alpha = 10^\circ$ and $\beta = 45^\circ$.

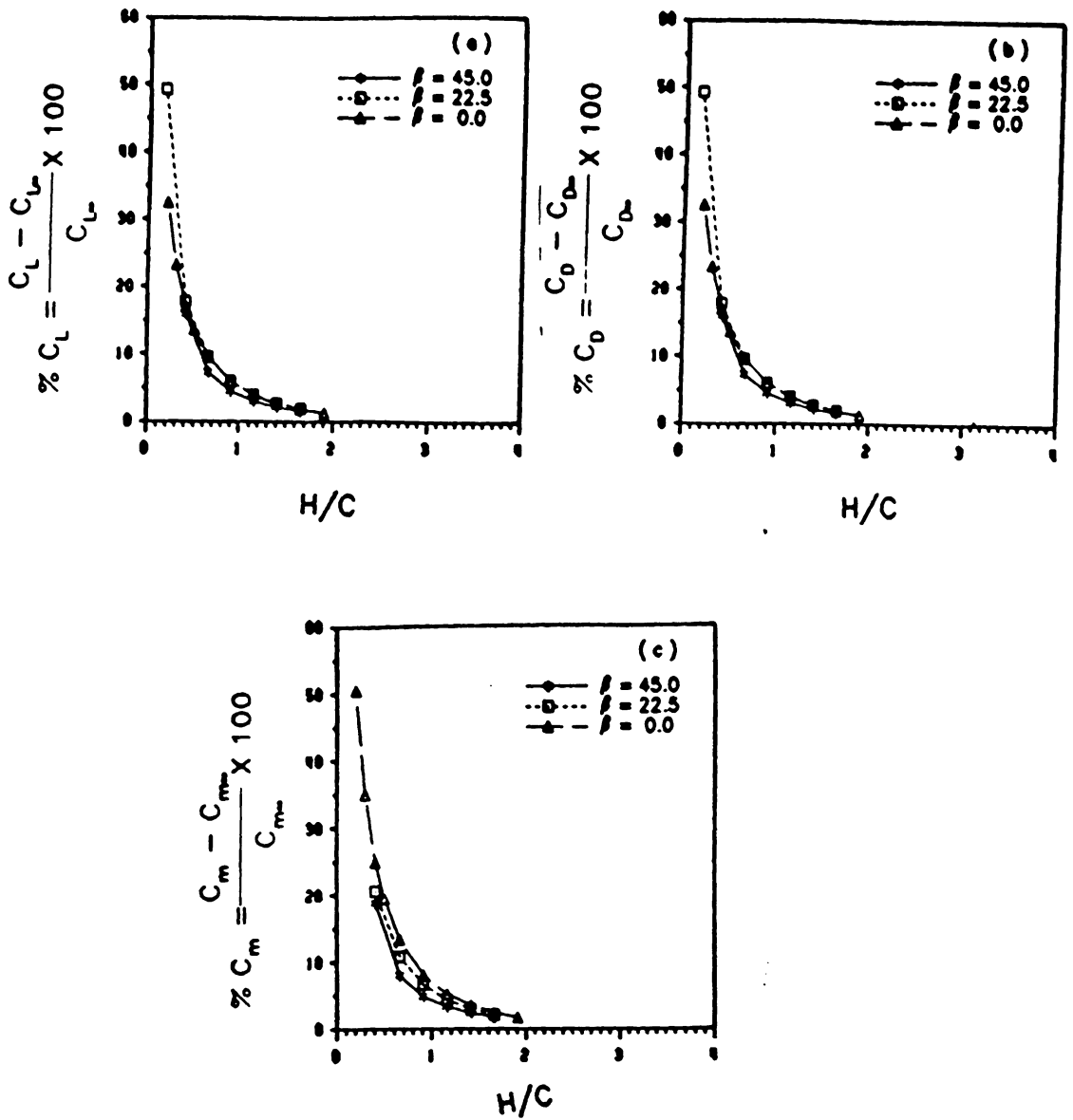


Figure 34. Computed results for a swept wing of aspect ratio 4 in ground effect for steady flow: (a) lift, (b) drag and (c) pitching-moment increments as functions of the height of the trailing edge above the ground for different sweep-back angles. $\alpha = 10^\circ$ and $\gamma = 0^\circ$.

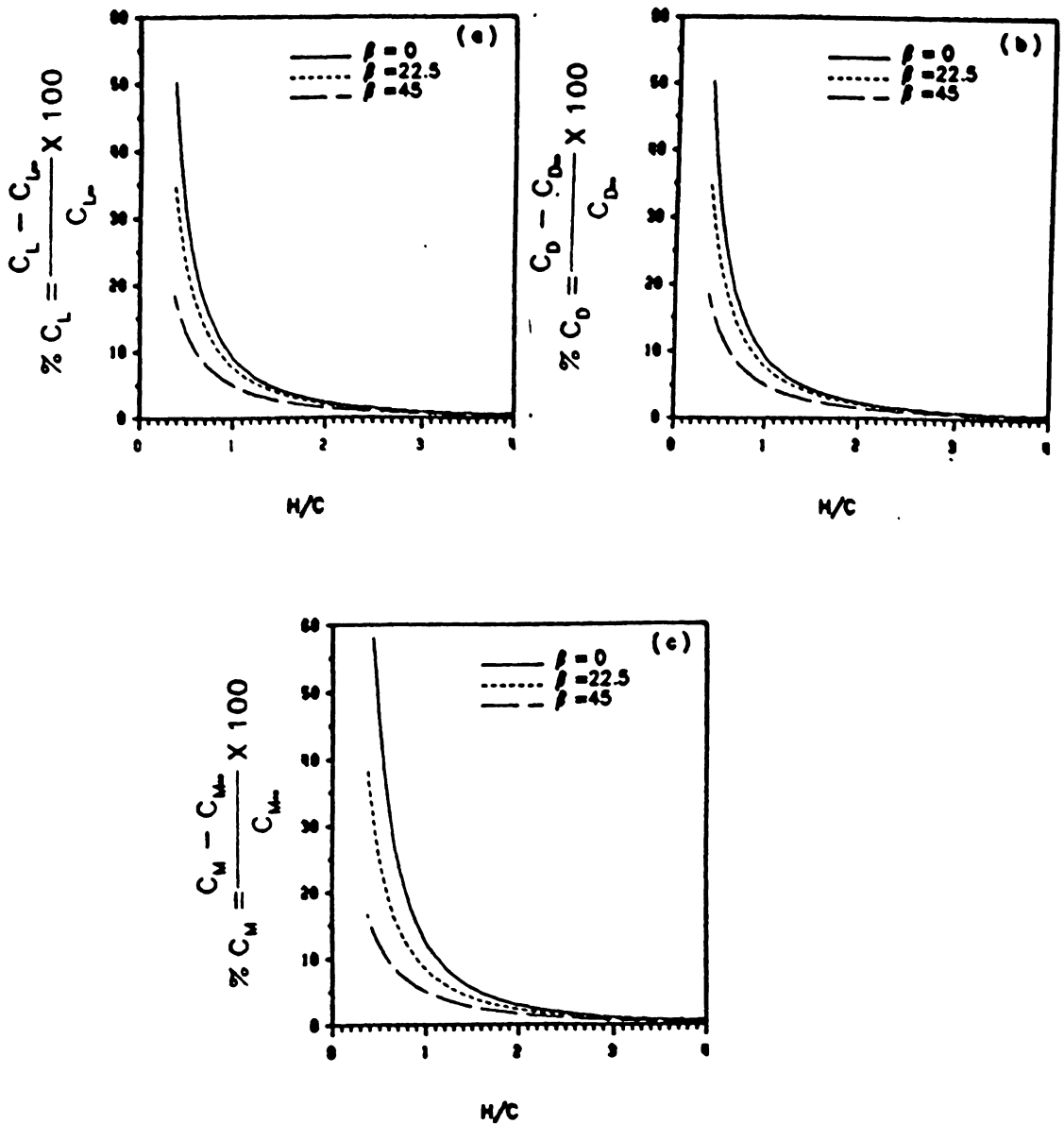


Figure 35. Computed results for a swept wing of aspect ratio 4 in ground effect for unsteady flow: (a) lift, (b) drag and (c) pitching-moment increments as functions of the height of the trailing edge above the ground for different sweep-back angles. $\alpha = 10^\circ$ and $\gamma = 20^\circ$.

3.8 Delta Wings

In figure 36, the computed and experimental aerodynamic coefficients are presented as functions of angle of attack far from the ground. The experimental results are taken from Bartlett and Vidal (1955), Chang (1985) and Wentz (1968). The wing is a flat thin delta wing for which the sweep-back angle is 70 degrees (AR = 1.456). The pitching-moment coefficient was calculated about an axis that passes through the apex. The pitching-moment coefficient is based on the root chord. These results and some experimental results from Bartlett and Vidal (1955) are shown in part (c). In part (d), the computed and experimental pitching-moment coefficients about an axis through the mid-point of the root chord are shown. The moment coefficients are based on two thirds of the root chord, which is the mean aerodynamic chord. There is good agreement between the computed and experimental results up to approximately 25 degrees angle of attack, where stall or vortex bursting begins. In figure 37, the aerodynamic coefficients in ground effect are given for a delta wing of aspect ratio 1.5 in steady flow. In each plot the computed results are compared with the experimental data of Chang (1985). The height above the ground divided by the span ($\frac{h}{b}$) is equal to 0.28 for the case near the ground, where h is measured to the mid-point of the root chord. In part (a) the lift coefficients as functions of angle of attack are shown. The agreement is good up to approximately 15 degrees angle of attack. In part (b) lift coefficients are plotted as functions of the drag coefficients. The computed results are in agreement with the experimental results. In part (c) lift coefficients are plotted as functions of the pitching-moment coefficients about an axis that passes through the mid-point of the

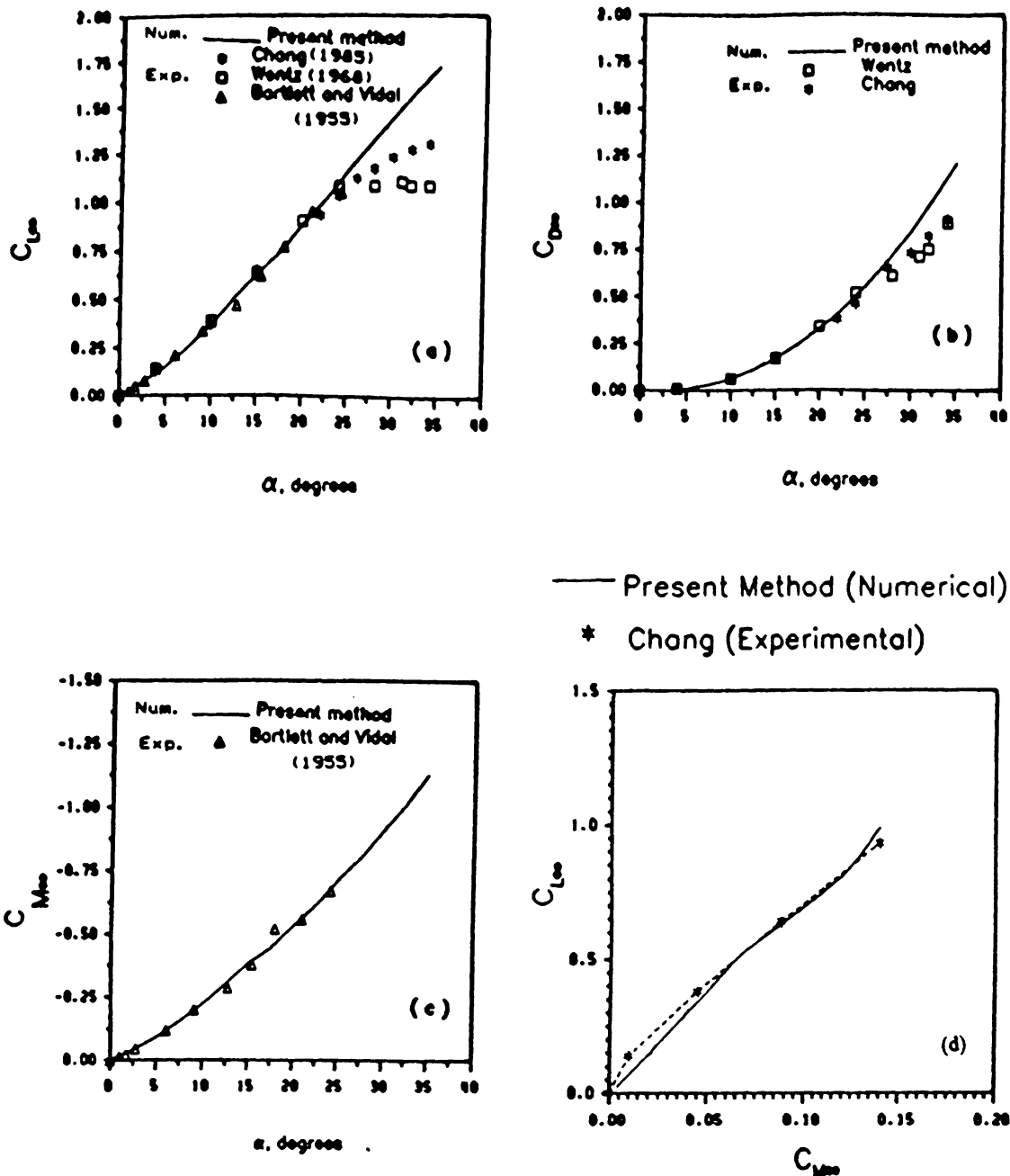


Figure 36. Numerical and experimental results for a thin flat delta wing ($AR = 1.5$) out of ground effect for steady flow: part (a) lift coefficients as functions of angles of attack. Part (b) drag coefficients as functions of angles of attack. Part (c) pitching-moment coefficients about an axis passes through the apex and based on the root chord as functions of angles of attack. Part (d) lift coefficients as functions of pitching-moment coefficients about an axis passes through one half of the root chord and based on the mean aerodynamic chord.

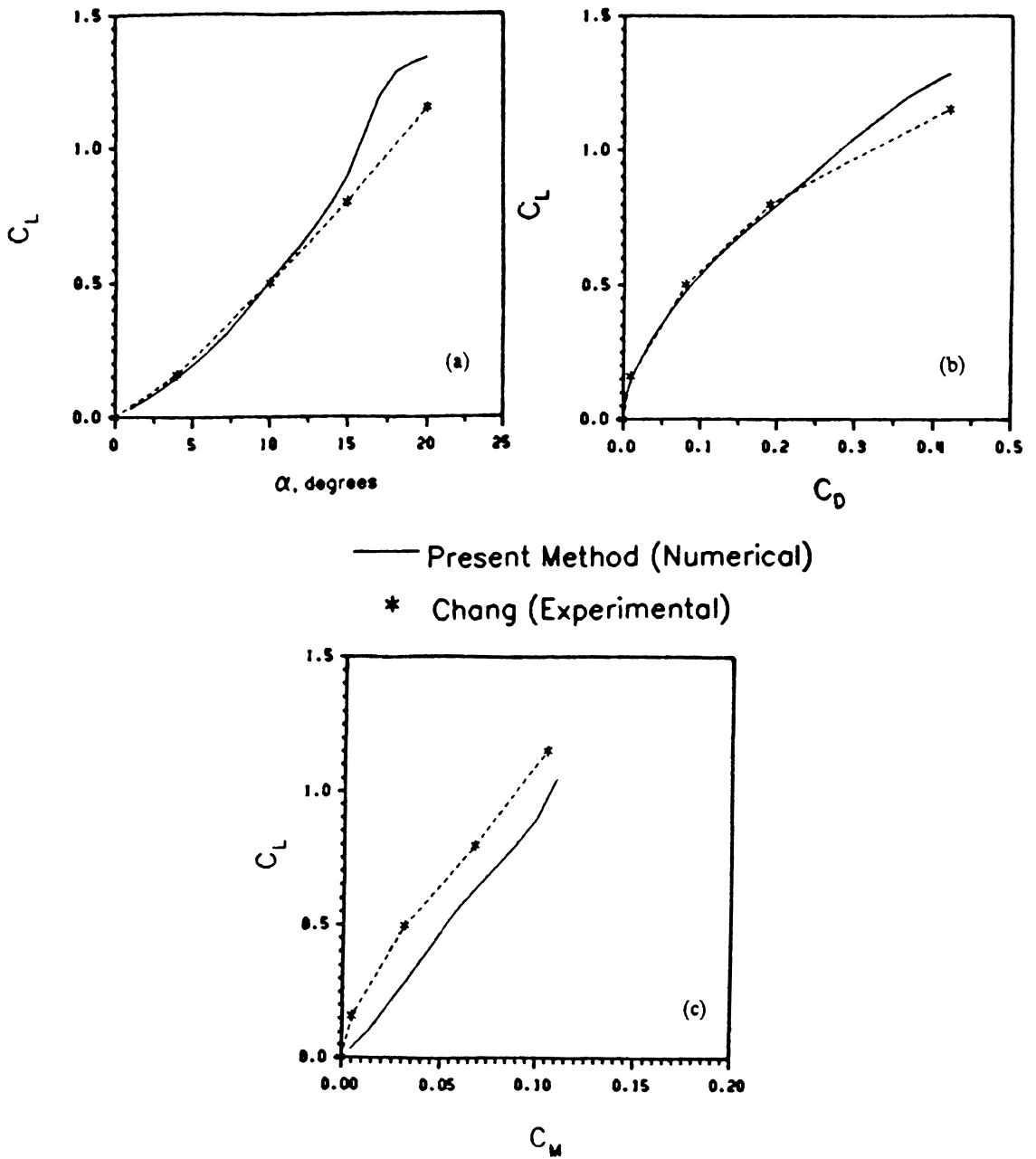


Figure 37. Numerical and experimental results for a thin flat delta wing ($AR = 1.5$) in ground effect for steady flow: part (a) lift coefficients as functions of angles of attack. Part (b) lift coefficients as functions of drag coefficients. Part (c) lift coefficients as functions of pitching-moment coefficients about an axis passes through one half of the root chord and based on the mean aerodynamic chord. For the case near the ground, $h/b = 0.28$ where h is the height of the mid-point of the root chord.

based on the mean aerodynamic chord. The computed results show the same trend as the experimental results.

In figure 38, the percentage changes in the coefficients of lift and drag are plotted for steady flow as functions of height above the ground for a thin flat delta wing ($AR = 1.456$) at ten degrees angle of attack. Similar results are given in figure 39 when the wing is at 22.1 degrees angle of attack. In both cases, the computed lift and the experimental data of Chang (1985) are in good agreement. For drag, both sets of results show the same trend, but they do not agree as well as those for the lift.

In figure 40, the percentage changes in the lift coefficient for unsteady flow are given as functions of the height of the mid-point of the root chord above the ground for a thin flat delta wing ($AR = 1.456$) at $\alpha = 22.1^\circ$. The steady results are included for comparison. The computed lift and experimental data of Chang (1985) are in fair agreement. It seems that the unsteadiness lowers the ground effect; this is due to the different definitions of H and h . As the next set of results show, the unsteadiness increases the effect.

In figure 41, the percentage changes in the aerodynamic coefficients are given as functions of the height of the trailing edge above the ground for different sink rates. The wing is a flat thin delta wing ($AR = 1.456$) at 22.1 degrees angle of attack. It is clear that the ground increases all coefficients and that this effect is stronger for higher sink rates.

In figure 42, the percentage changes in the aerodynamic coefficients for a thin delta wing are plotted as functions of the height of the trailing edge above the ground for different aspect ratios for unsteady flows ($\gamma = 20^\circ$). The angle of attack is 10 degrees. It is clear that the ground effects increase all coefficients and that these effects are stronger for larger aspect ratios. The same trend was noticed for sink rates $\gamma = 10^\circ$ and $\gamma = 0^\circ$.

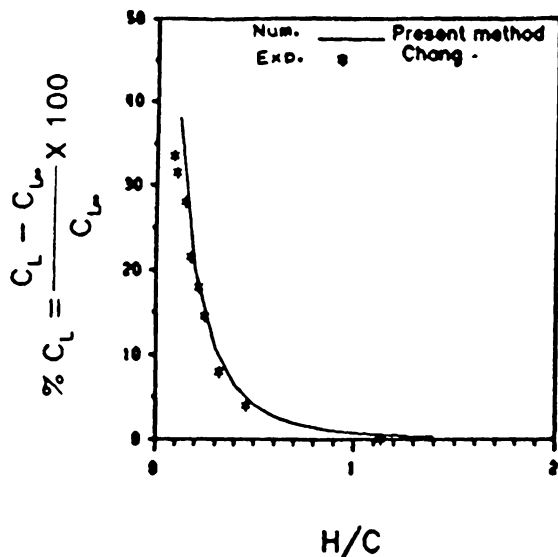


Figure 38. A comparison of the computed and experimental results for delta wing (AR = 1.5) in steady ground effect: lift increments at $\alpha = 10^\circ$ as functions of the height of the trailing edge above the ground.

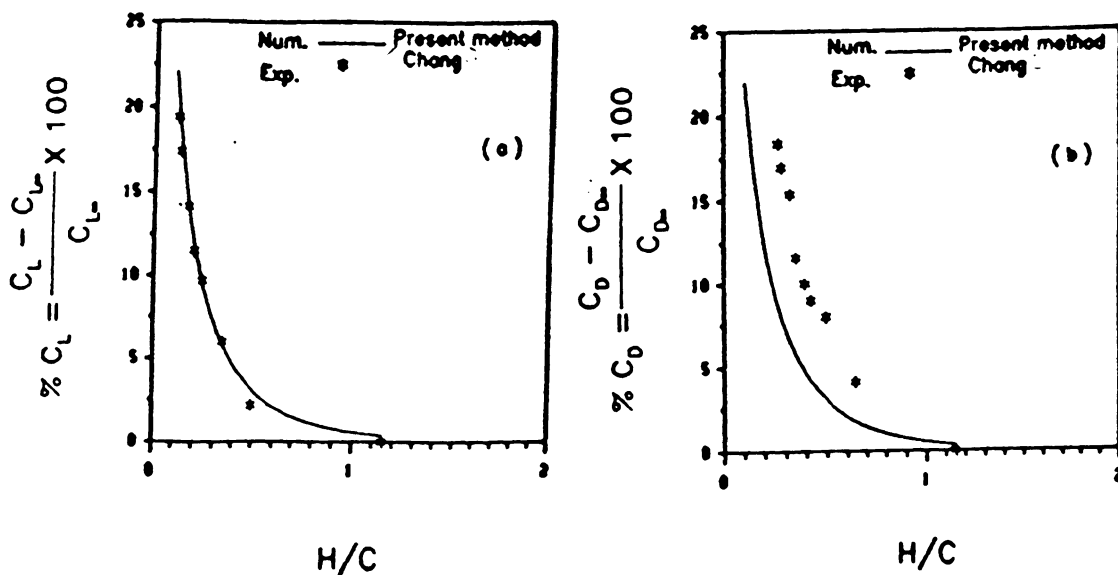


Figure 39. A comparison of the computed and experimental results for delta wing (AR = 1.5) in steady ground effect: (a) lift and (b) drag increments at $\alpha = 22.1^\circ$ as functions of the height of the trailing edge above the ground.

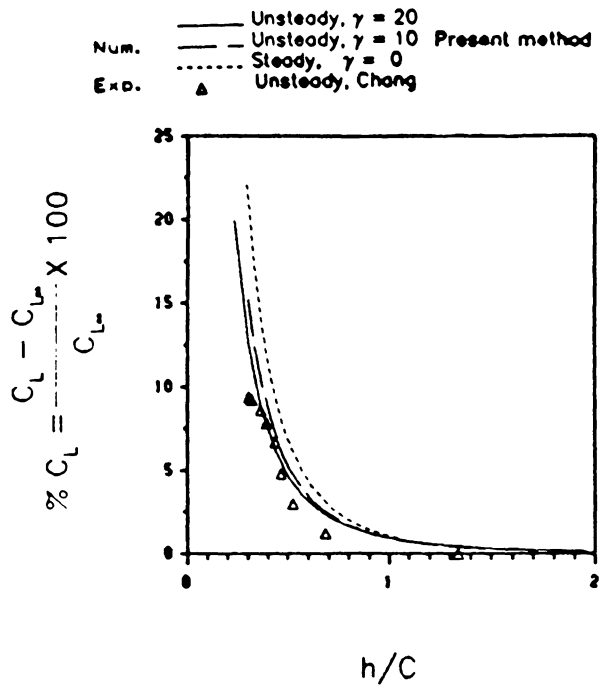


Figure 40. A comparison of the computed and experimental results for delta wing ($AR = 1.5$) in unsteady ground effect: lift increments at $\alpha = 22.1^\circ$ as functions of the height of the mid-point of the root chord above the ground.

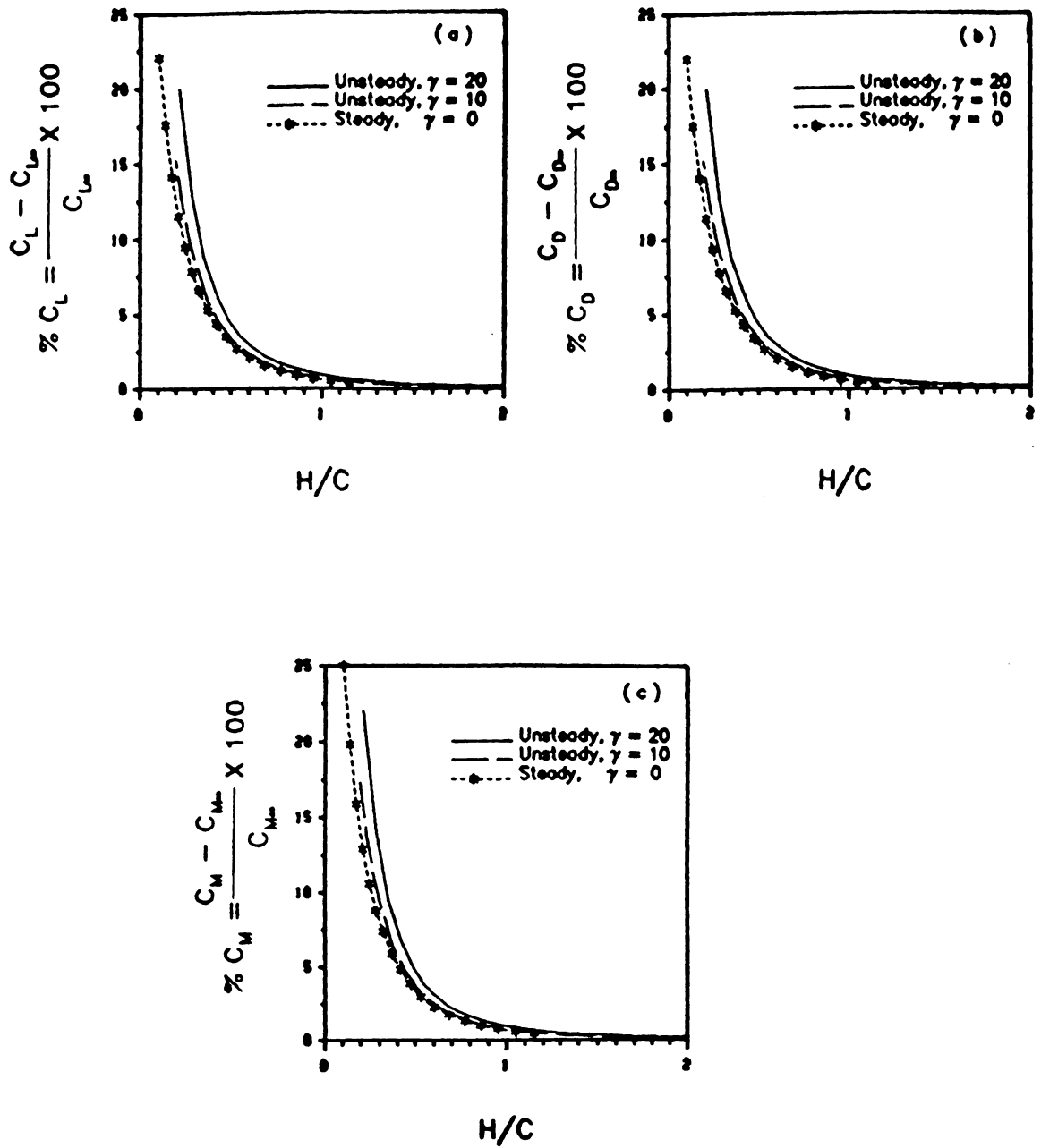


Figure 41. Computed results for a delta wing of aspect ratio 1.5 in ground effect: (a) lift, (b) drag and (c) pitching-moment increments at $\alpha = 10^\circ$ as functions of the height of the trailing edge above the ground for different sink rate.

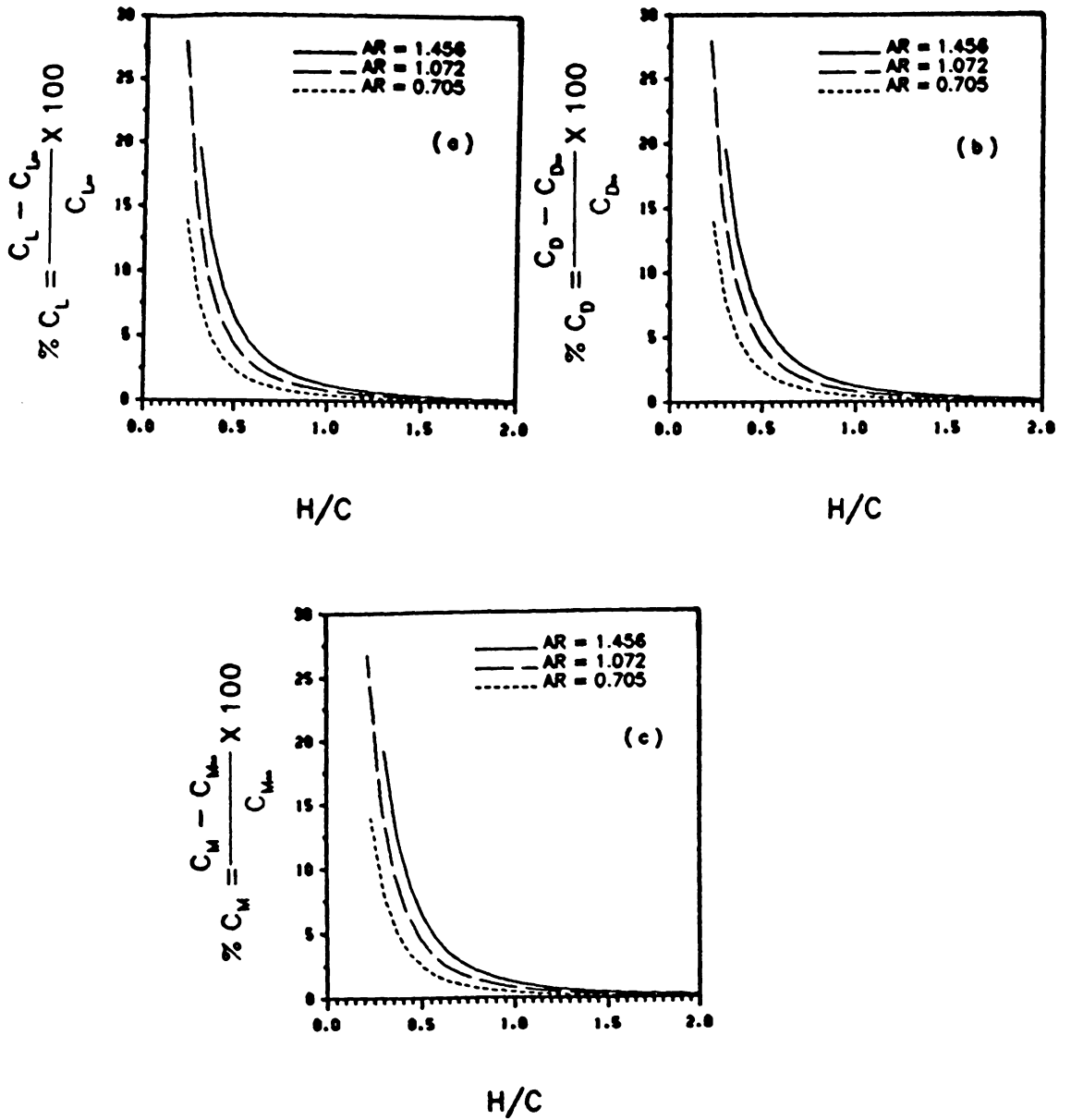


Figure 42. Computed results for delta wings in ground effect for unsteady flow: (a) lift, (b) drag and (c) pitching-moment increments at $\alpha = 10^\circ$ and $\gamma = 20^\circ$ as functions of the height of the trailing edge above the ground for different aspect ratios.

3.9 Wind Effect

In figure 43, the percentage changes in rolling moment and side force for a rectangular wing of unit aspect ratio at $\alpha = 10^\circ$ and $\phi = 10^\circ$ (roll angle) for steady flow are given as functions of the height of the trailing edge above the ground. The magnitude of the wind velocity is taken to be ten percent of the magnitude of the velocity of the wing. Clearly, the ground effect increases the restoring rolling moment and side force.

In figures 44 and 45, the aerodynamic coefficients of rectangular wings of unit aspect ratio are plotted as functions of the height of the trailing edge above the ground for different sink rates in 10 and 20 percent head wind, respectively. The angle of attack is 10° and the angle of roll is 0° . Clearly, the ground increases all coefficients and that this effect is weaker for higher sink rates.

In figure 46, the aerodynamic coefficients for a rectangular wing of unit aspect ratio at $\alpha = 10^\circ$, $\phi = 10^\circ$, $\eta = 45^\circ$ and 10% wind velocity are given as functions of the height of the trailing edge above the ground for different sink rates. Similar results are shown in figure 47 when $\eta = 90^\circ$; that is, when the cross-wind velocity is 10%.

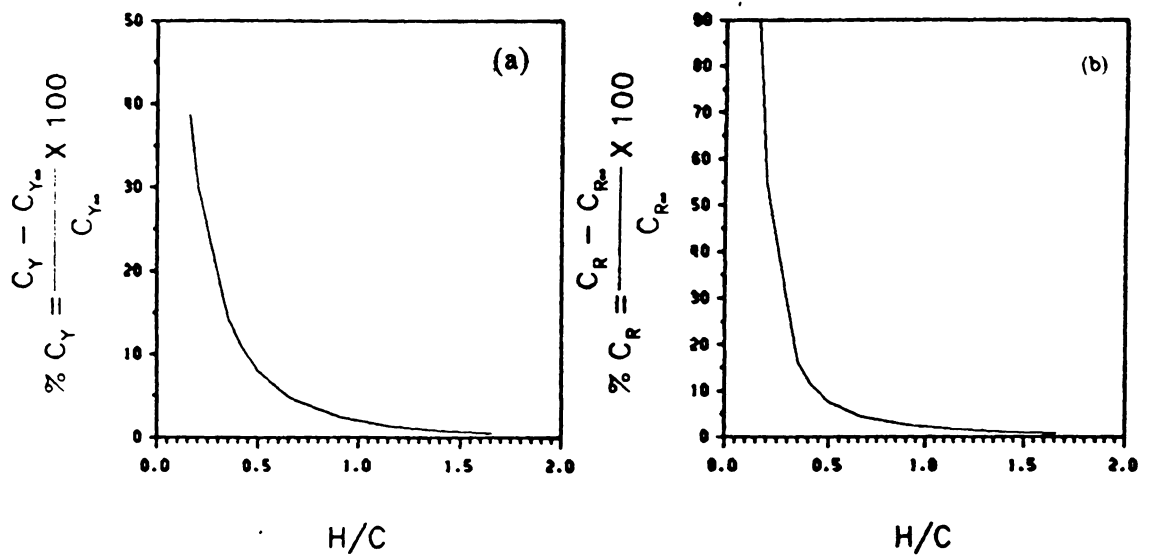


Figure 43. Computed results for a rectangular wing of aspect ratio 1 in ground effect with cross and head winds for steady flow: (a) side force and (b) rolling-moment increments at $\alpha = 10^\circ$, $\phi = 5^\circ$ and 3.4% cross- and 9.4% head-wind velocities as functions of the height of the trailing edge above the ground.

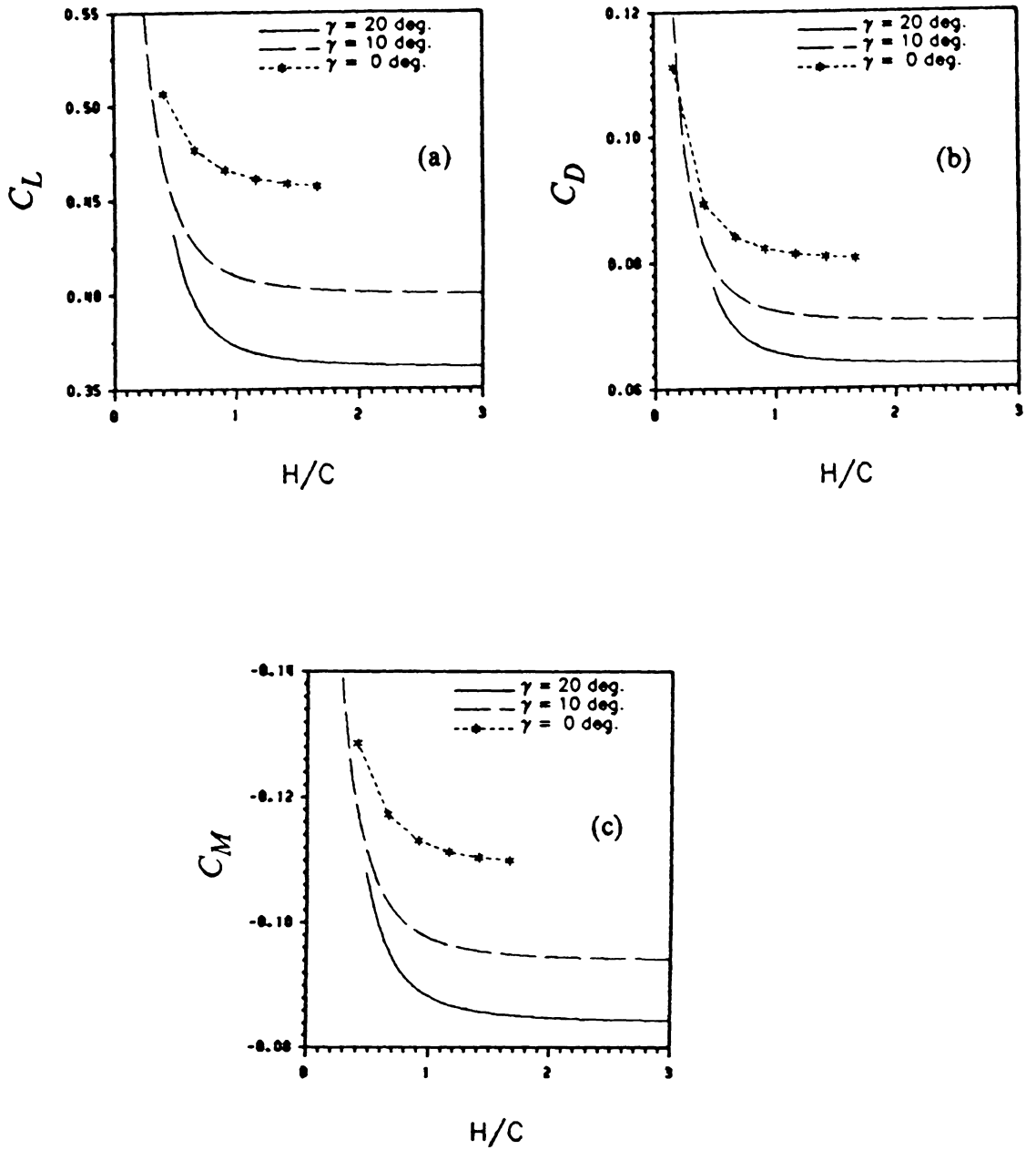


Figure 44. Computed results for a rectangular wing of aspect ratio 1 in ground effect with head wind: (a) normal force, (b) pitching-moment and (c) rolling-moment coefficients at $\alpha = 10^\circ$, $\phi = 0^\circ$ and 10% head-wind velocity as functions of the height of the trailing edge above the ground for different sink rates.

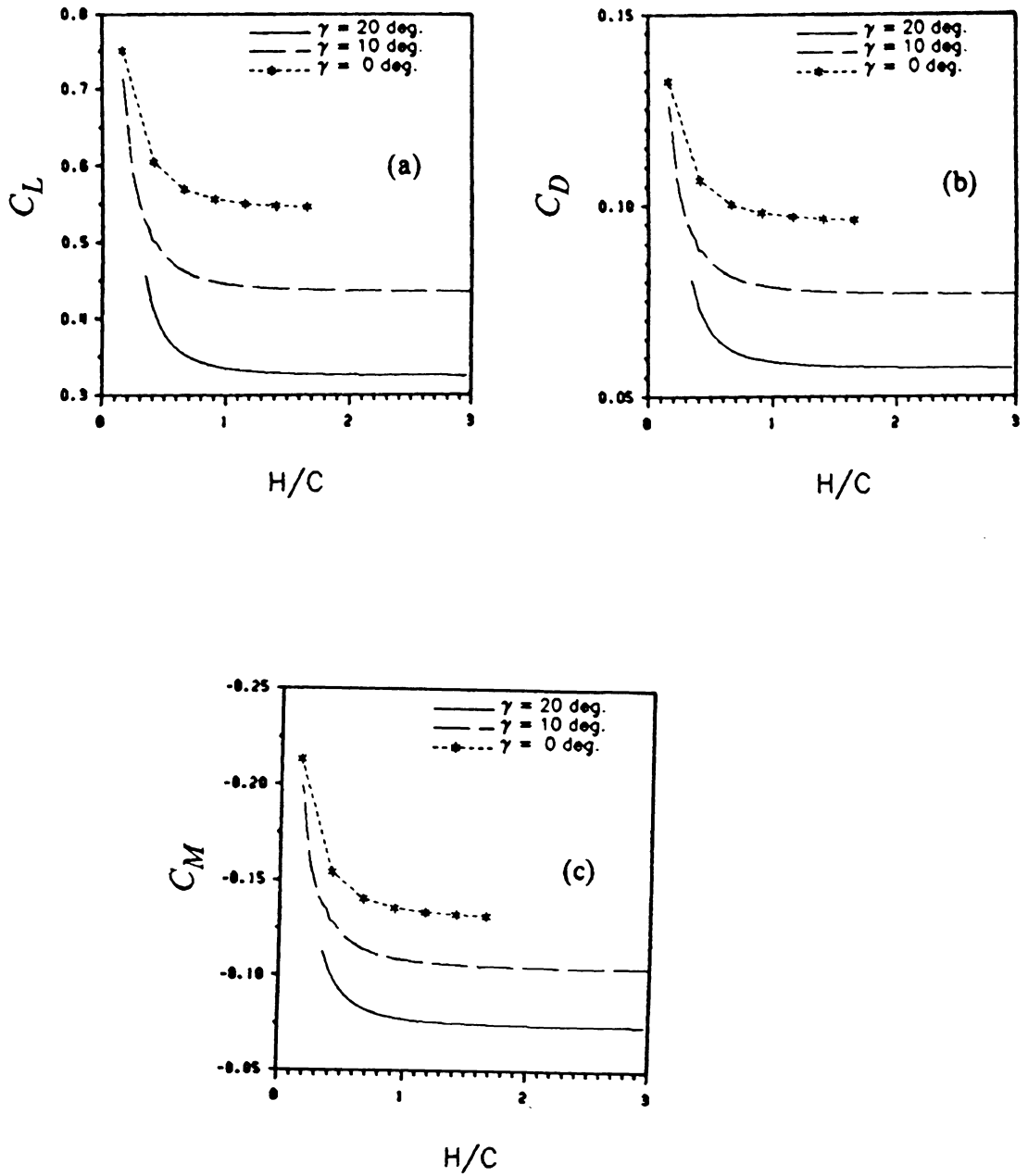


Figure 45. Computed results for a rectangular wing of aspect ratio 1 in ground effect with head wind: (a) normal force, (b) pitching-moment and (c) rolling-moment coefficients at $\alpha = 10^\circ$, $\phi = 0^\circ$ and 20% head-wind velocity as functions of the height of the trailing edge above the ground for different sink rates.

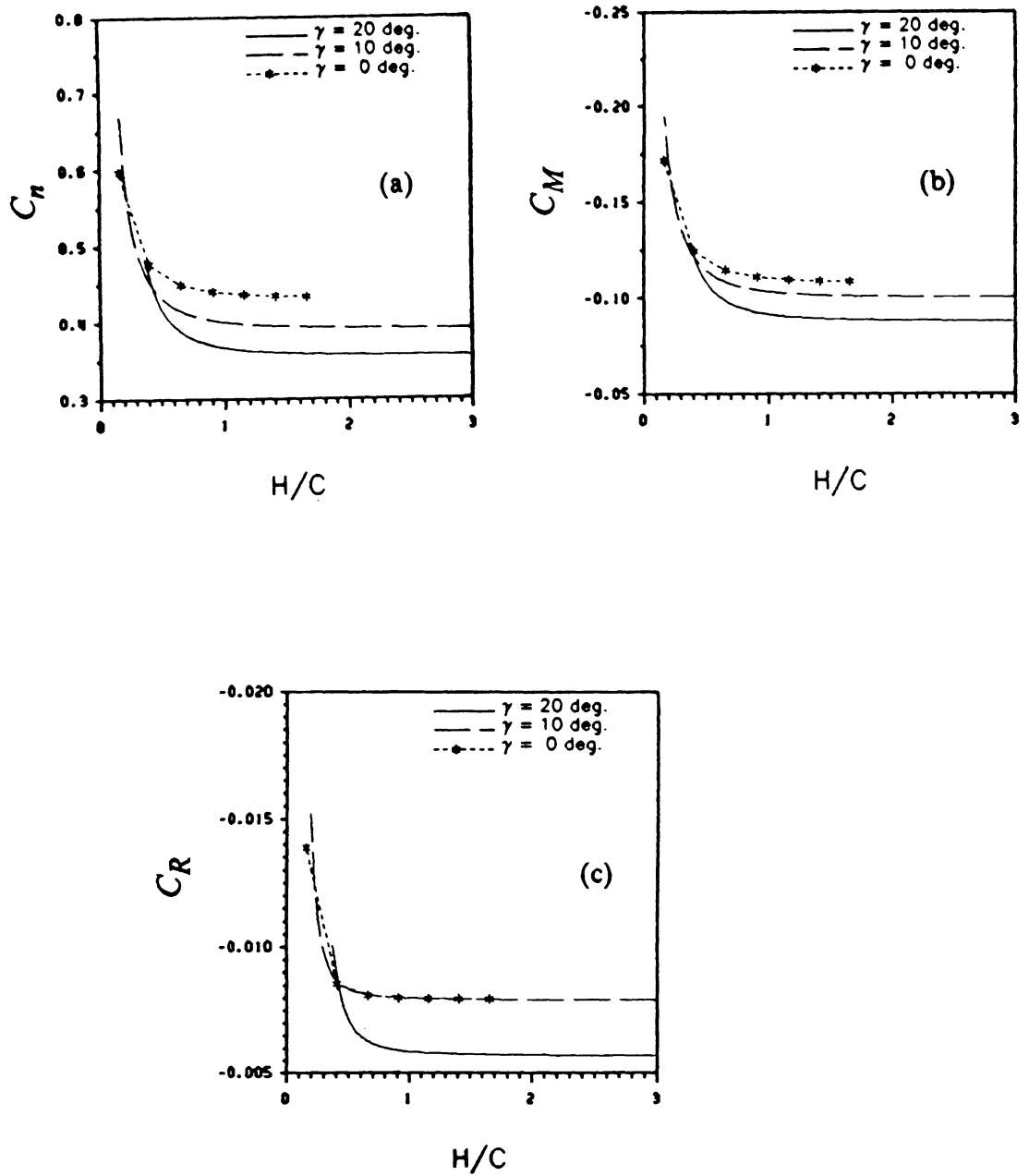


Figure 45. Computed results for a rectangular wing of aspect ratio 1 in ground effect with cross and head winds: (a) normal force, (b) pitching-moment and (c) rolling-moment coefficients at $\alpha = 10^\circ$, $\phi = 10^\circ$ and 7.1% cross- and 7.1% head-wind velocities as functions of the height of the trailing edge above the ground for different sink rates.

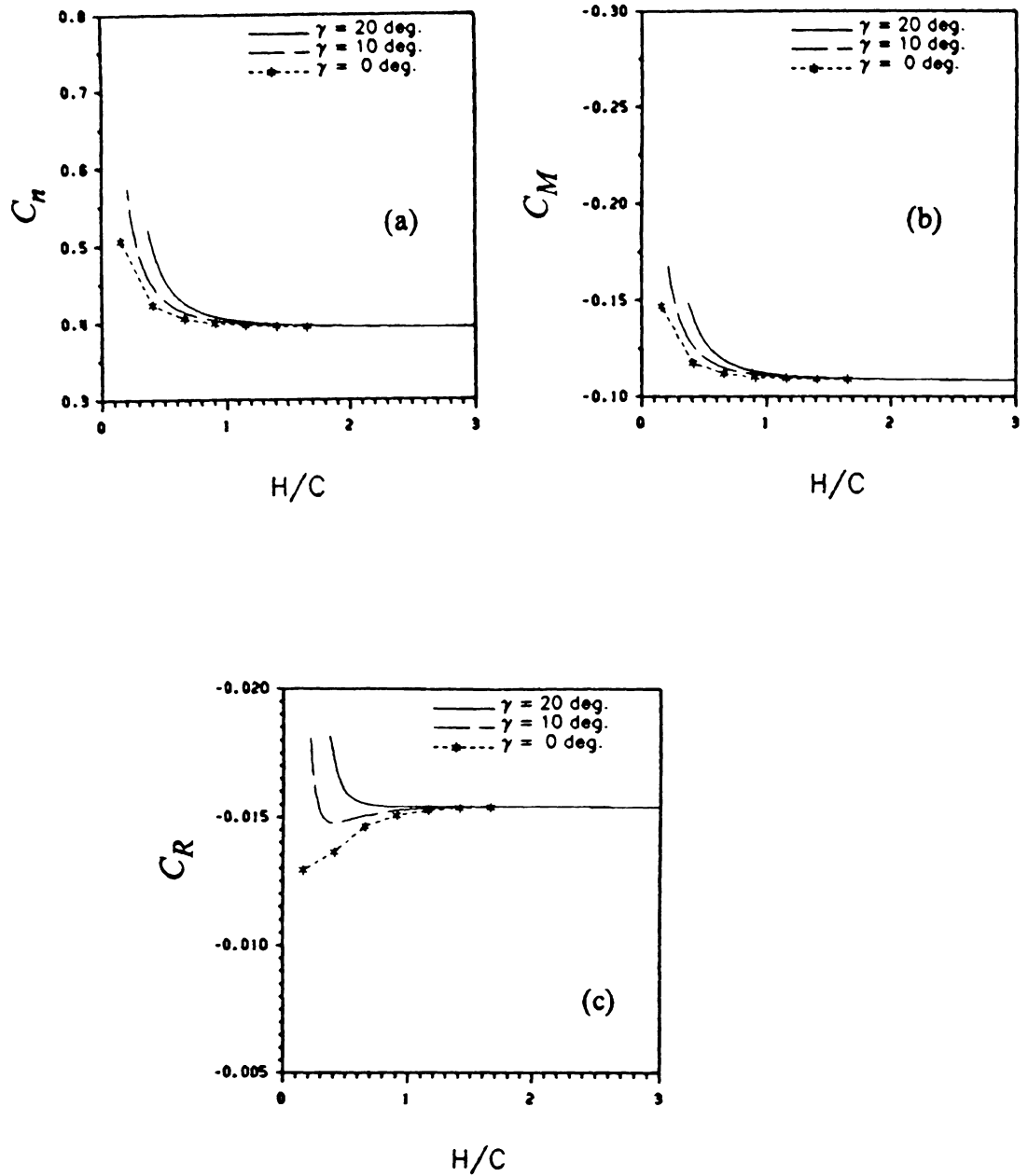


Figure 47. Computed results for a rectangular wing of aspect ratio 1 in ground effect with cross wind: (a) normal force, (b) pitching-moment and (c) rolling-moment coefficients at $\alpha = 10^\circ$, $\phi = 10^\circ$ and 10% cross-wind velocity as functions of the height of the trailing edge above the ground for different sink rates.

3.10 *Flight-Path Effect*

In figure 48, the aerodynamic coefficients for a rectangular wing of unit aspect ratio at $\alpha = 10^\circ$ are plotted as functions of the horizontal distance in and out of ground effects for unsteady flow, $\gamma_0 = 25^\circ$. The flight path is a sine wave with $Z_0 = 23.286$ and $Z_{\min} = 4.231$ (see section 2.5). The axis of rotation passes through the leading edge. Similar results are shown in figures 49 and 50 when the axis of rotation passes through the mid point of the root chord and the trailing edge, respectively. In figure 49, Z_0 and Z_{\min} are 24.063 and 4.998, respectively. For the case in figure 50, Z_0 and Z_{\min} are 24.839 and 5.775, respectively.

In figure 51, the aerodynamic coefficients for a rectangular wing of unit aspect ratio at $\alpha = 10^\circ$ are plotted as functions of the horizontal distance in and out of ground effects for unsteady flow, $\gamma_0 = 25^\circ$. The flight path is a parabola with $Z_0 = 23.286$ and $Z_{\min} = 4.221$. The axis of rotation passes through the leading edge. Similar results are shown in figure 52 when the flight path is a circular arc with $Z_0 = 23.286$ and $Z_{\min} = 4.228$.

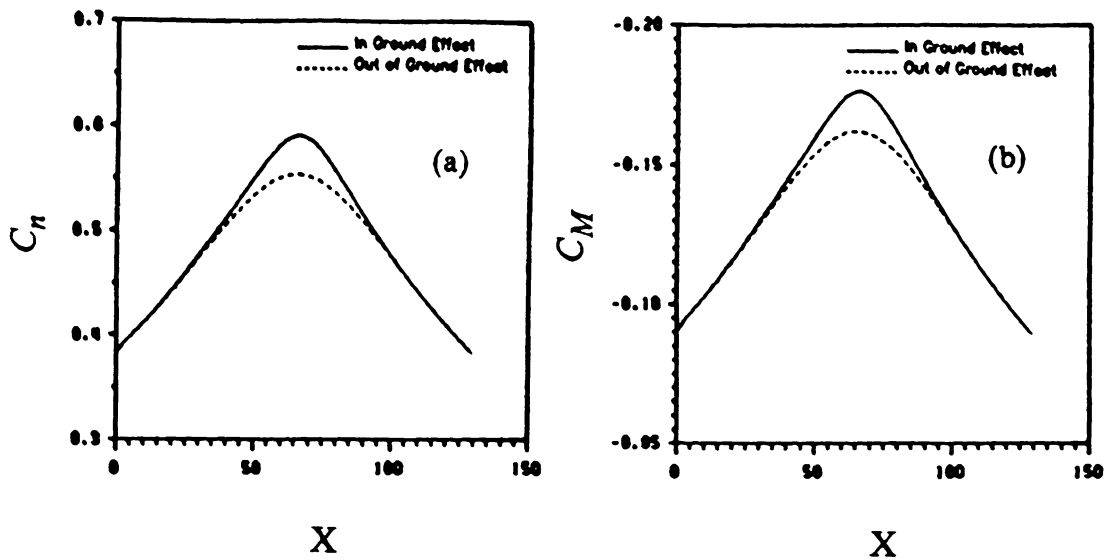


Figure 48. Computed results for a rectangular wing ($AR = 1$) flying along a sinusoidal flight path in and out of ground effects: (a) normal force and (c) pitching-moment coefficients at $\alpha = 10^\circ$ and $\gamma_0 = 25^\circ$ as functions of the horizontal ground distance. The axis of rotation passes through the leading edge.

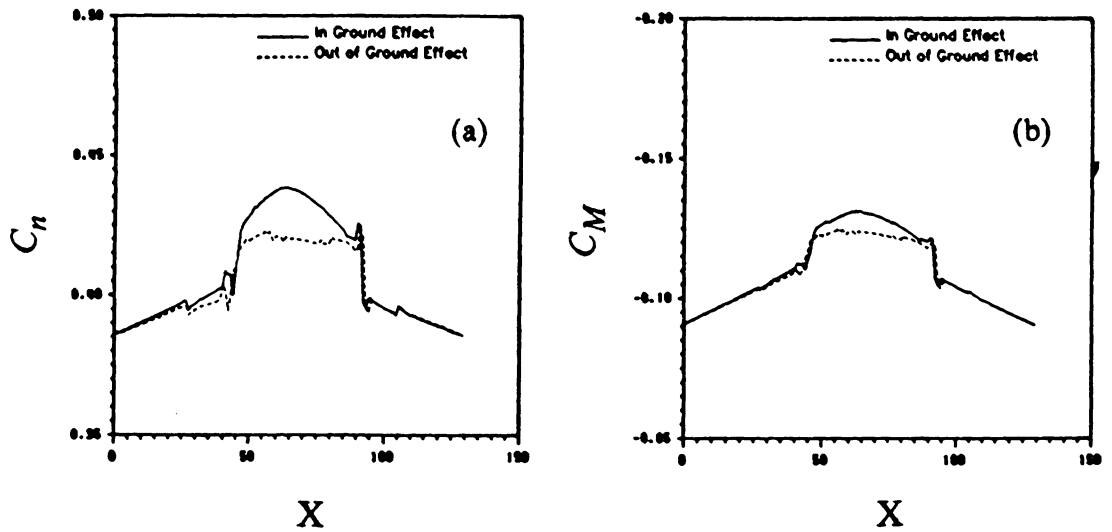


Figure 49. Computed results for a rectangular wing ($AR = 1$) flying along a sinusoidal flight path in and out of ground effects: (a) normal force and (c) pitching-moment coefficients at $\alpha = 10^\circ$ and $\gamma_0 = 25^\circ$ as functions of the horizontal ground distance. The axis of rotation passes through the mid-point of the chord.

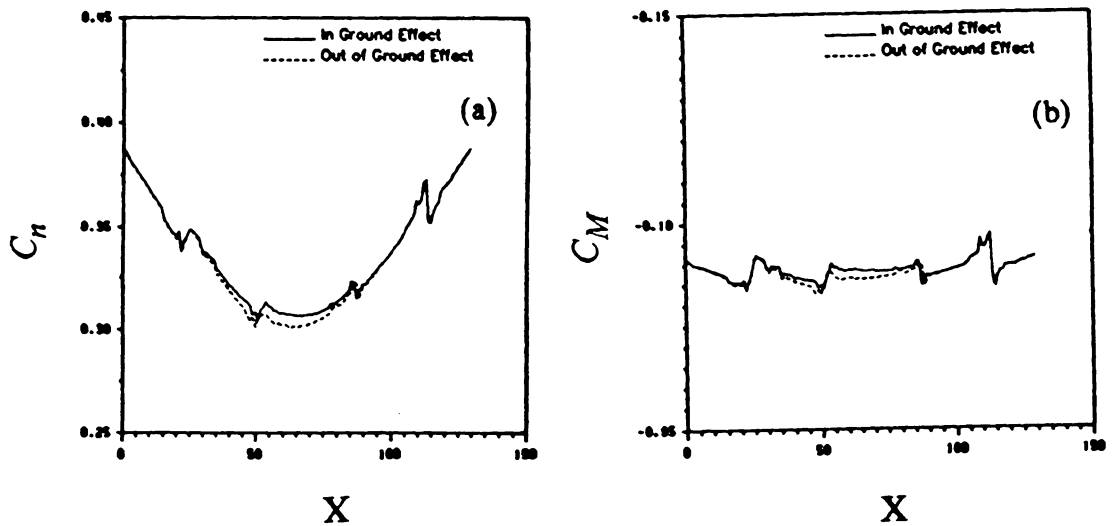


Figure 50. Computed results for a rectangular wing ($AR = 1$) flying along a sinusoidal flight path in and out of ground effects: (a) normal force and (c) pitching-moment coefficients at $\alpha = 10^\circ$ and $\gamma_0 = 25^\circ$ as functions of the horizontal ground distance. The axis of rotation passes through the trailing edge.

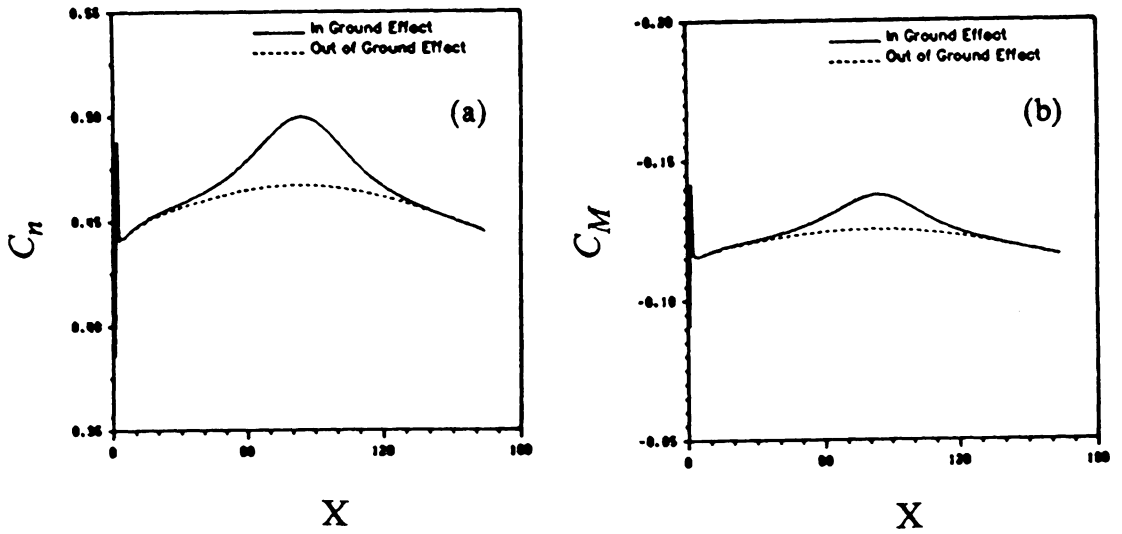


Figure 51. Computed results for a rectangular wing ($AR = 1$) flying along a parabolic flight path in and out of ground effects: (a) normal force and (c) pitching-moment coefficients at $\alpha = 10^\circ$ and $\gamma_0 = 25^\circ$ as functions of the horizontal ground distance. The axis of rotation passes through the leading edge.

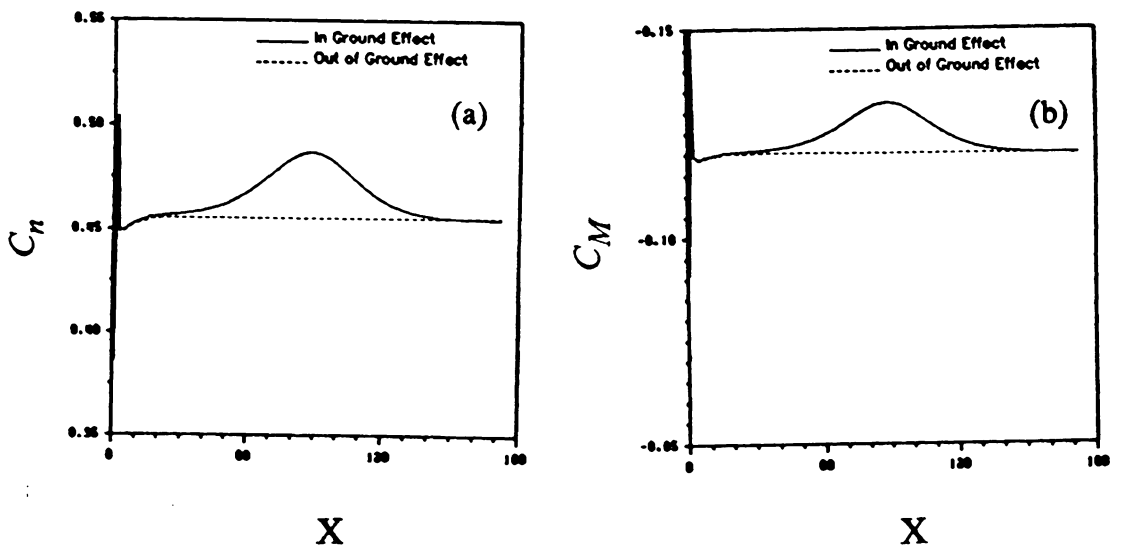


Figure 52. Computed results for a rectangular wing ($AR = 1$) flying along a circular flight path in and out of ground effects: (a) normal force and (c) pitching-moment coefficients at $\alpha = 10^\circ$ and $\gamma_0 = 25^\circ$ as functions of the horizontal ground distance. The axis of rotation passes through the leading edge.

3.11 Concluding Remarks

The aerodynamic model of chapter II has been used to investigate the steady and unsteady ground effects on a single lifting surface for different planforms. In addition, the model has been used to study the effects of cross and/or head winds and of flight-path shapes on a flat rectangular wing. The computed effect of the ground restricts the downward movement of the wake and causes it to spread. The present results show the influences of various parameters on the aerodynamic coefficients for both steady and unsteady flows. Generally, the aerodynamic coefficients increase with proximity to the ground, the greater the sink rates the greater the increases. Increasing the aspect ratio increases both the steady and unsteady ground effects for both rectangular and delta planforms. An exception is a large aspect-ratio wing (here we consider a two-dimensional wing) with large camber. Such a wing actually experiences a loss of lift and pitching moment (about the trailing edge) near the ground. The present computed results are generally in close agreement with limited exact solutions and experimental data. The present results serve to demonstrate the potential of the present approach.

In the next chapter, we couple the aerodynamic model of chapter II with the equations of motion of an aircraft and the resulting model is then coupled with a feedback-control law. The resulting model will be used to control an aircraft flying in level flight near the ground.

Chapter IV

Dynamics and Control

4.1 *General*

In chapter II, the aerodynamic model was described in detail. In chapter III, the model was shown to be capable of predicting the aerodynamic forces and moments accurately in and out of ground effect. In this chapter, we couple the equations of motion to the aerodynamic model. Then, we couple a feedback-control system to the resulting model.

The coordinate system for a second lifting surface is introduced in section 4.2. The aerodynamic model of chapter II is coupled with the equations of motion of an aircraft in section 4.3. The resulting model is coupled with a feedback-control system in section 4.4.

4.2 Coordinate System

The pitch of an airplane is controlled by its horizontal tail and/or canard. We numerically simulate this effect by introducing another lifting surface that has one degree of freedom relative to the body-fixed axes x,y,z . We attach a right-handed coordinate system to the control surface, as shown in figure 53.

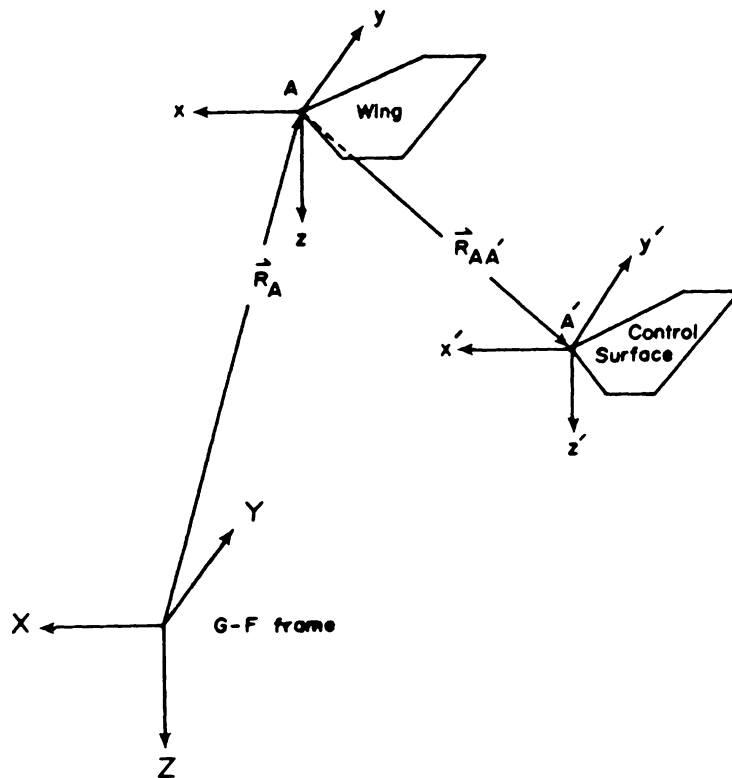


Figure 53. Coordinate systems of the wing and control surface.

The control-surface axes and their unit vectors are denoted by x', y', z' and i', j', k' , respectively. The x' - and y' -axes lie in the plane of the planform of the control surface, while the z' -axis is normal to the control surface and points downward. The x' -axis points forward. The transformation from the unit vectors of the $B-F$ frame i', j', k' to those of the $B-F$ frame i, j, k is given by the following:

$$\begin{bmatrix} \vec{i}' \\ \vec{j}' \\ \vec{k}' \end{bmatrix} = \begin{bmatrix} c\delta & 0 & -s\delta \\ 0 & 1 & 0 \\ s\delta & 0 & c\delta \end{bmatrix} \begin{bmatrix} \vec{i} \\ \vec{j} \\ \vec{k} \end{bmatrix} \quad (4.2 - 1)$$

where δ is the angle which x' makes with the x -axis, and c and s denote cosine and sine functions, respectively. The following equation

$$\begin{bmatrix} x' \\ y' \\ z' \end{bmatrix} = \begin{bmatrix} c\delta & 0 & -s\delta \\ 0 & 1 & 0 \\ s\delta & 0 & c\delta \end{bmatrix} \begin{bmatrix} x - x_{AA'} \\ y - y_{AA'} \\ z - z_{AA'} \end{bmatrix} \quad (4.2 - 2)$$

transforms the coordinates of a point in the body axes x, y, z to the body axes x', y', z' , where $x_{AA'}$, $y_{AA'}$, and $z_{AA'}$ are the coordinates of the origin of the $B-F$ x', y', z' frame in terms of those of the $B-F$ x, y, z frame. The $x_{AA'}$, $y_{AA'}$, and $z_{AA'}$ are the components of $\vec{R}_{AA'}$ (see figure 53).

In the computer code, the position of the control surface with respect to the main wing is arbitrary. The control surface can be placed either behind or in front of the main wing. Moreover, the control surface can be placed either above or below the main wing. The axis of rotation of either the main wing or the control surface can be anywhere. Moreover, both pitching and hinge moments can be taken about any axis (not necessary the axis of rotation).

The control surface was discretized into a finite number of elements. The mutual aerodynamic interference between the main wing and the control surface is predicted by the aerodynamic model of chapter II in and out of ground effects. Namely, we solve equation 2.3-15 in which N refers to the sum of elements of the main wing and the control surface. In the case of wing and tail configurations, the wake of the wing must feel the control surface as a solid surface. Similarly, in the case of wing/canard configurations, the canard wake must feel the wing as a solid surface.

In figure 54, actual computed wakes for a wing and tail configuration in and out of ground effect are shown. The tail was located above the wing chord line. In part (a), the side and top views of the wake are shown for the case far from the ground. In part (b), the side and top views of the wake are shown for the case near the ground. The horizontal line below the wing for the case near the ground shows the position of the ground; it is also included in the results for the case far from the ground for comparison. Clearly, the wake of the wing envelopes the tail. Moreover, the effect of the ground restricts the downward movement of the wake and causes it to spread.

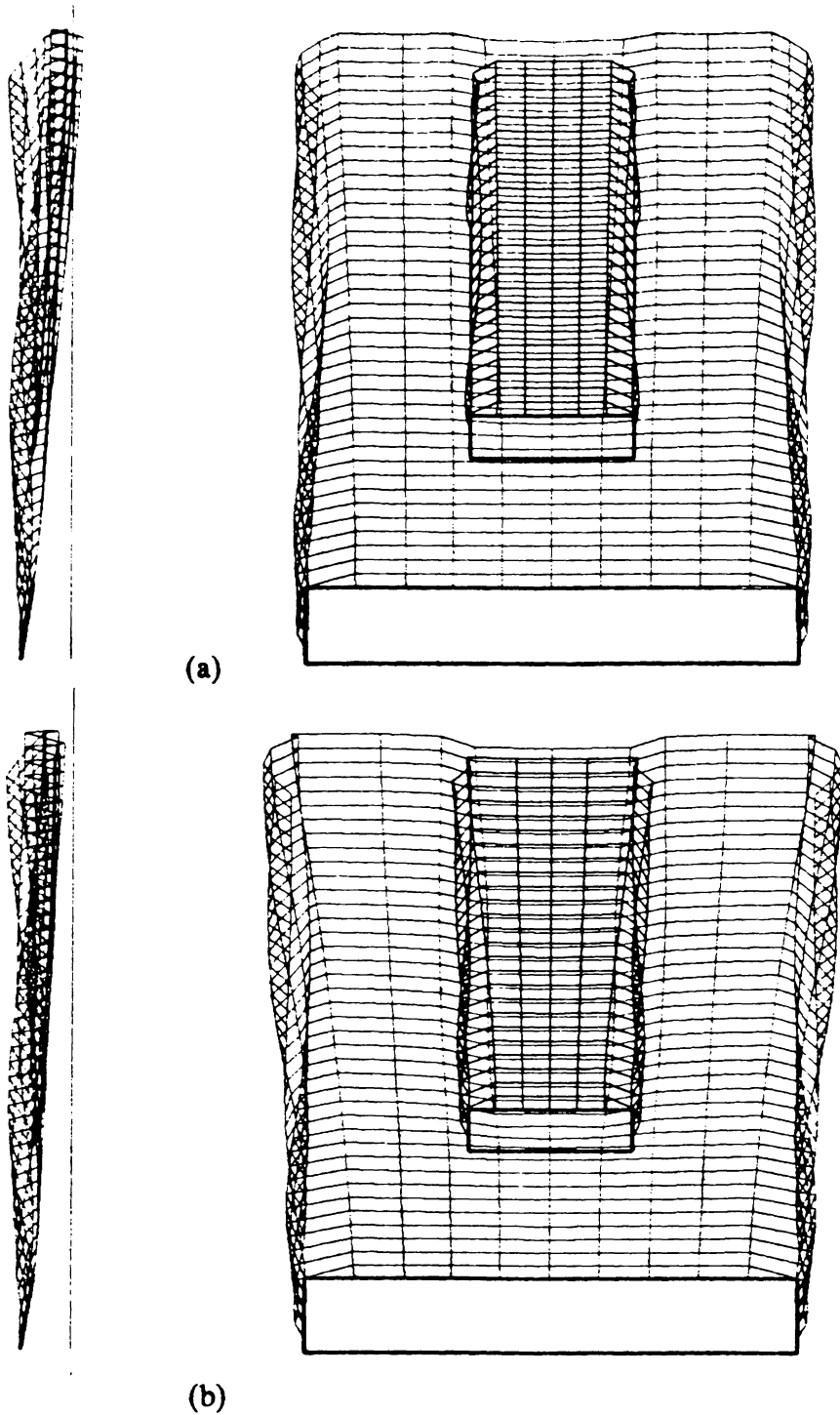


Figure 54. Actual computed wakes for a wing and tail configuration: part (a) out of ground effect and part (b) in ground effect for steady flows.

4.3 Dynamics

4.3.1 Equations of Motion

The motion of an aircraft can be divided into two independent groups. One is called longitudinal motion and the other is called lateral. Here, we limit our presentation to the longitudinal motion. That is, the aircraft can move forward, downward, upward and pitch about an axis passing through the center of mass.

The equations of motion of an aircraft (see, for example, Etkin, 1982) are given by the following:

$$(T - D) \cos \alpha + L \sin \alpha - mg \sin \theta = m(\dot{u} + \dot{\theta}w) \quad (4.3 - 1)$$

$$(T - D) \sin \alpha - L \cos \alpha + mg \cos \theta = m(\dot{w} - \dot{\theta}u) \quad (4.3 - 2)$$

$$M = I_{yy}\ddot{\theta} \quad (4.3 - 3)$$

where T is the thrust force and it is assumed to be parallel to the flight path, D is the drag force, L is the lift force, M is the pitching moment about the center of gravity, m is the mass of the aircraft, g is the acceleration of gravity, I_{yy} is the mass moment of inertia of the aircraft, α is the angle of attack, θ is the pitch angle, and u and w are the x - and z -components of velocity in B - F frame, respectively.

It is convenient to work with the equations of motion in dimensionless form. The equations of motion in dimensionless form become

$$\dot{u} = -\dot{\theta}w + C_1[(C_t - C_D) \cos \alpha + C_L \sin \alpha] - C_2 \sin \theta \quad (4.3 - 4)$$

$$\dot{w} = \dot{\theta}u + C_1[(C_t - C_D) \sin \alpha - C_L \cos \alpha] + C_2 \cos \theta \quad (4.3 - 5)$$

$$\ddot{\theta} = C_3 C_M \quad (4.3 - 6)$$

where $C_1 = \frac{\rho A_{wing}}{2m} L$, $C_2 = \frac{g}{U^2} L$ and $C_3 = \frac{\rho A_{wing} C_{rwing}}{2I_{yy}} L^2$ in which A_{wing} is the plan area of the wing, L is the characteristic length, ρ is the air density and C_{rwing} is the root chord of the wing. the dot denotes the derivative with respect to nondimensional time. The thrust, lift, drag and pitching-moment coefficients are defined as follows:

$$C_t = \frac{T}{\frac{\rho U^2 A_{wing}}{2}}, \quad C_L = \frac{L}{\frac{\rho U^2 A_{wing}}{2}}, \quad C_D = \frac{D}{\frac{\rho U^2 A_{wing}}{2}} \quad \text{and} \quad C_M = \frac{M}{\frac{\rho U^2 A_{wing} C_{wing}}{2}}$$

The initial conditions are given by the following:

$$\begin{aligned} u(t=0) = u_0 = U \cos \alpha_0, \quad w(t=0) = w_0 = U \sin \alpha_0, \\ \theta(t=0) = \theta_0 \quad \text{and} \quad \dot{\theta}(t=0) = 0 \end{aligned} \quad (4.3 - 7)$$

The variables u , w and θ can be found by solving the equations 4.3-2 to 4.3-4 with the above initial conditions. The new angle of attack, α , may be computed from the following equation:

$$\alpha = \tan^{-1} \frac{w}{u} \quad (4.3 - 8)$$

The flight-path angle, γ , may be computed from the following:

$$\gamma = \alpha - \theta \quad (4.3 - 9)$$

The position of the aircraft may be found from the following:

$$X_{A_{i+1}} = \bar{X}_{A_i} + \int_{t_i}^{t_{i+1}} V_{A_x} dt \quad \text{and} \quad Z_{A_{i+1}} = \bar{Z}_{A_i} + \int_{t_i}^{t_{i+1}} V_{A_z} dt \quad (4.3 - 10)$$

Where X_A and Z_A are the X- and Z-components of the position vector of the center of mass in terms of the *G-F* frame, respectively. V_{A_x} and V_{A_z} are the X- and Z-components of the velocity vector of the center of mass in terms of the *G-F* frame, respectively. The subscripts i and $i + 1$ refer to the present and one time step in the future, respectively.

4.3.2 Method of Solution

It was mentioned earlier that the time step employed in the aerodynamic model was chosen to be unity; consequently the Runge-Kutta method will be excluded when solving the equations of motion. As a result, we turn to predictor-corrector methods, which are highly accurate and employ integral time steps. One of the most popular predictor-corrector methods is Hamming's method. It is a fourth-order-accurate method. Carnahan et al. (1969), for example, derived this method and have written a computer code for solving second-order differential equations. In this dissertation, Hamming's method is used as found in Carnahan et al. with the exception that an iteration scheme is incorporated into the method.

Hamming's method solves a system of first-order differential equations. As a result, the equations of motion are rewritten as a system of first-order differential equations. A general system of differential equations has the following form:

$$\dot{y}_j = f_j(t, y_1, y_2, \dots, y_n) \quad \text{for } j = 1, 2, \dots, n \quad (4.4 - 1)$$

with the initial conditions

$$y_j(0) = \alpha_j \quad \text{for } j = 1, 2, \dots, n \quad (4.4 - 2)$$

where y_j , f_j and α_j are the j -components of column vectors with n components each. Hamming's method requires the solutions, y_j , and the right-hand sides, f_j , to be known at three previous time steps plus at the present time. As a result, different methods are used to generate the solution for the first three time steps. Then, Hamming's scheme is used to complete the computation process. So, it may be in order to discuss the starting procedure before presenting Hamming's method (which may be called the general method).

For the first time step, we employ Euler and modified Euler methods as predictor-corrector scheme (see Palm III, 1983). The complete algorithm is:

1. The iteration number, k , is set equal to 0.
2. The right-hand sides of equation 4.4-1, f_j , are evaluated at the present time ($t = 0$).
3. The predicted solutions, y_j^p , of equations 4.4-1 are computed using the Euler method:

$$y_j^p = y_{j,1} + f_{j,1} \Delta t \quad \text{for } j = 1, 2, \dots, n \quad (4.4 - 3)$$

where $y_{j,1} = y_j(0) = \alpha_j$, $f_{j,1} = f_j(0, y_1(0), y_2(0), \dots, y_n(0))$ and the superscript p denotes the predicted solution.

4. The table of y and f is updated; namely

$$y_{j,2} = y_{j,1} \quad \text{and} \quad f_{j,2} = f_{j,1} \quad (4.4 - 4)$$

5. The solutions of equations 4.4-1 are set equal to the predicted solutions; namely

$${}^k y_{j,1} = y_j^p \quad (4.4 - 5)$$

6. These solutions are supplied to the aerodynamic model and used to compute the aerodynamic forces and moments. These may be considered the predicted loads at the new time.

7. The right-hand sides of equations 4.4-1 are re-evaluated at the new time ($t = \Delta t$) with the new aerodynamic loads from step 6.

8. The iteration number, k , is set equal to $k + 1$

9. The modified Euler method is then used to compute the corrected solutions, ${}^k y_{j,1}$; namely

$${}^k y_{j,1} = y_{j,2} + [f_{j,1} + f_{j,2}] \frac{\Delta t}{2} \quad \text{for } j = 1, 2, \dots, n \quad (4.4 - 6)$$

where $f_{j,1} = f_j(\Delta t, {}^{k-1}y_1(\Delta t), {}^{k-1}y_2(\Delta t), \dots, {}^{k-1}y_n(\Delta t))$

10. The absolute value of the difference between the solutions at the present and previous iterations, ${}^k e_j$, is estimated as follows:

$${}^k e_j = |{}^k y_{j,1} - {}^{k-1} y_{j,1}| \quad \text{for } j = 1, 2, \dots, n \quad (4.4 - 7)$$

11. ϵ_j is checked to see if all its components are less or equal to some small user-supplied error criterion. If the condition is not satisfied the computation process is repeated starting at step 6 until the solutions converge. The above procedure is summarized by the flow chart in figure 55.

12. After the solutions converge, the time is set equal to Δt and the computer code switches to another method for finding the solutions at the second time step.

For the second time step, we use the Adams-Bashforth two-step predictor and the Adams-Moulton two-step corrector schemes (see Burden et al., 1981). The complete algorithm is:

1. The iteration number, k , is set equal to 0.
2. The right-hand sides of equation 4.4-1 are evaluated at the present time ($t = \Delta t$).
3. The predicted solutions, y_j^p , of equations 4.4-1 are computed using the Adams-Bashforth two-step predictor method:

$$y_j^p = y_{j,1} + [3f_{j,1} + f_{j,2}] \frac{\Delta t}{2} \quad \text{for } j = 1, 2, \dots, n \quad (4.4 - 8)$$

where

$$y_{j,1} = y_j(\Delta t), \quad f_{j,1} = f_j(\Delta t, y_1(\Delta t), y_2(\Delta t), \dots, y_n(\Delta t)) \quad \text{and} \quad f_{j,2} = f_j(0, y_1(0), y_2(0), \dots, y_n(0))$$

4. The table of y and f is updated; namely

$$y_{j,3} = y_{j,2}, \quad y_{j,2} = y_{j,1}, \quad f_{j,3} = f_{j,2} \quad \text{and} \quad f_{j,2} = f_{j,1} \quad (4.4 - 9)$$

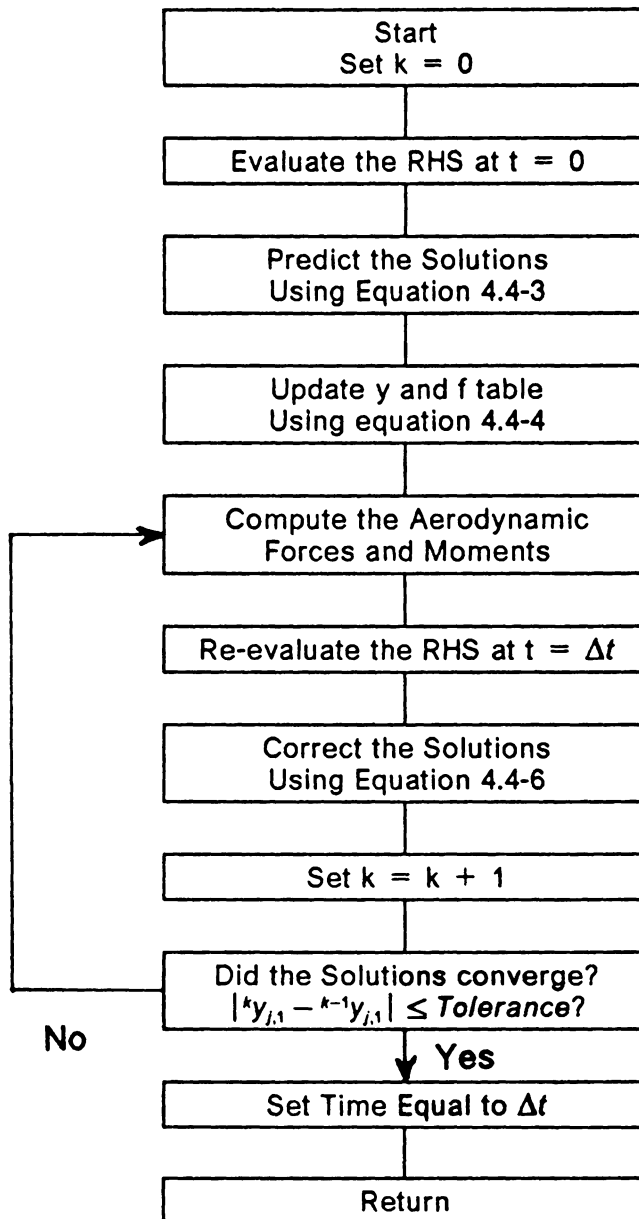


Figure 55. Flow Chart for the First-Predictor-Corrector Method

5. The solutions of equations 4.4-1 are set equal to the predicted solutions; namely

$${}^k y_{j,1} = y_j^p \quad (4.4 - 10)$$

6. These solutions are supplied to the aerodynamic model and used to compute the aerodynamic forces and moments. These may be considered the predicted loads at the new time.
7. The right-hand sides of equations 4.4-1 are re-evaluated at the new time ($t = 2\Delta t$) with the new aerodynamic loads from step 6.
8. The iteration number, k , is set equal to $k + 1$
9. The Adams-Moulton two-step corrector method is used to compute the corrected solutions, ${}^k y_{j,1}$; namely

$${}^k y_{j,1} = y_{j,2} + [5f_{j,1} + 8f_{j,2} - f_{j,3}] \frac{\Delta t}{12} \quad \text{for } j = 1, 2, \dots, n \quad (4.4 - 11)$$

where $f_{j,1} = f_j(2\Delta t, {}^{k-1}y_1(2\Delta t), {}^{k-1}y_2(2\Delta t), \dots, {}^{k-1}y_n(2\Delta t))$

10. The absolute value of the difference between the solutions at the present and previous iterations, ${}^k e_j$, is estimated as follows:

$${}^k e_j = |{}^k y_{j,1} - {}^{k-1} y_{j,1}| \quad \text{for } j = 1, 2, \dots, n \quad (4.4 - 12)$$

11. ${}^k e_j$ is checked to determine if all its components are less or equal to the error tolerance. If the condition is not satisfied the computation process is repeated starting at step 6 until the solutions converge. The above procedure can be summarized by a flow chart that is similar to the one in figure 55.
12. After the solutions converge, the time is set equal to $2\Delta t$ and the computer code switches to another method for finding the solutions at the third time step.

For the third time step, we use the Adams-Bashforth three-step predictor and the Adams-Moulton three-step corrector schemes (see Burden et al., 1981). The complete algorithm is:

1. The iteration number, k , is set equal to 0.
2. The right-hand sides of equation 4.4-1 are evaluated at the present time ($t = 2\Delta t$).
3. The predicted solutions, y_j^p , of equations 4.4-1 are computed by using the Adams-Bashforth three-step predictor method:

$$y_j^p = y_{j,1} + [23f_{j,1} - 16f_{j,2} + 5f_{j,3}] \frac{\Delta t}{12} \quad \text{for } j = 1, 2, \dots, n \quad (4.4 - 13)$$

where

$$y_{j,1} = y_j(2\Delta t), \quad f_{j,1} = f_j(2\Delta t, y_1(2\Delta t), y_2(2\Delta t), \dots, y_n(2\Delta t)),$$

$$f_{j,2} = f_j(\Delta t, y_1(\Delta t), y_2(\Delta t), \dots, y_n(\Delta t)) \quad \text{and} \quad f_{j,3} = f_j(0, y_1(0), y_2(0), \dots, y_n(0))$$

4. The table of y and f is updated; namely

$$y_{j,4} = y_{j,3}, \quad y_{j,3} = y_{j,2}, \quad y_{j,2} = y_{j,1}, \quad f_{j,4} = f_{j,3}, \quad f_{j,3} = f_{j,2} \quad \text{and} \quad f_{j,2} = f_{j,1} \quad (4.4 - 14)$$

5. The solutions are set equal to the predicted solutions; namely

$${}^k y_{j,1} = y_j^p \quad (4.4 - 15)$$

6. These solutions are supplied to the aerodynamic model and used to compute the aerodynamic forces and moments.
7. The right-hand sides of equations 4.4-1 are re-evaluated at the new time ($t = 3\Delta t$).
8. The iteration number, k , is set equal to $k + 1$
9. The Adams-Moulton three-step corrector method is used to compute the corrected solutions, ${}^k y_{j,1}$; namely

$${}^k y_{j,1} = y_{j,2} + [9f_{j,1} + 19f_{j,2} - 5f_{j,3} + f_{j,4}] \frac{\Delta t}{24} \quad \text{for } j = 1, 2, \dots, n \quad (4.4 - 16)$$

where $f_{j,1} = f_j(3\Delta t, {}^{k-1}y_1(3\Delta t), {}^{k-1}y_2(3\Delta t), \dots, {}^{k-1}y_n(3\Delta t))$

10. The absolute value of the difference between the solutions at the present and previous iterations, ${}^k e_j$, is estimated as follows:

$${}^k e_j = |{}^k y_{j,1} - {}^{k-1} y_{j,1}| \quad \text{for } j = 1, 1, \dots, n \quad (4.4 - 17)$$

11. ${}^k e_j$ is checked to determine if all its components are less or equal to the error tolerance. If the condition is not satisfied the computation process is repeated starting at step 6 until the solutions converge. The above algorithm can be summarized by a flow chart that is similar to the one in figure 55.
12. After the solutions converge, the time is set equal to $3\Delta t$ and the computer code switches to the general method for finding the solutions at the fourth and all later time steps.

For the fourth time step and beyond, we use Hamming's predictor-corrector method (see Caranhan et al., 1969). The complete algorithm is:

1. The iteration number, k , is set equal to 0.
2. The right-hand sides of equation 4.4-1 are evaluated at the present time (t_i).
3. The predicted solutions, y_j^p , of equations 4.4-1 are computed using Hamming's predictor:

$$y_j^p = y_{j,4} + \frac{4\Delta t}{3} [2f_{j,1} - f_{j,2} + 2f_{j,3}] \quad \text{for } j = 1, 2, \dots, n \quad (4.4 - 18)$$

where

$$y_{j,4} = y_j(t_i - 3\Delta t), \quad f_{j,1} = f_j(t_i, y_1(t_i), y_2(t_i), \dots, y_n(t_i)),$$

$$f_{j,1} = f_j(t_i, y_1(t_i), y_2(t_i), \dots, y_n(t_i)),$$

$$f_{j,2} = f_j(t_i - \Delta t, y_1(t_i - \Delta t), y_2(t_i - \Delta t), \dots, y_n(t_i - \Delta t))$$

and

$$f_{j,3} = f_j(t_i - 2\Delta t, y_1(t_i - 2\Delta t), y_2(t_i - 2\Delta t), \dots, y_n(t_i - 2\Delta t))$$

4. The table of y and f is updated; namely

$$y_{j,4} = y_{j,3}, \quad y_{j,3} = y_{j,2}, \quad y_{j,2} = y_{j,1}, \quad f_{j,3} = f_{j,2} \quad \text{and} \quad f_{j,2} = f_{j,1} \quad (4.4 - 19)$$

5. The predicted solutions, y_j^p , are modified by using the truncation-error estimates, $\epsilon_{j,i}$, from the previous step (see equation 4.4-24 below)

$$y_j^* = y_j^p + \frac{112}{9} te_{j,i} \quad \text{for } j = 1, 2, \dots, n \quad (4.4 - 20)$$

where * refers to the modified solutions (all the components of $te_{j,i}$ are set equal to zero the first time the general method is used).

6. The solutions of equations 4.4-1 are set equal to the modified solutions; namely

$${}^k y_{j,1} = y_j^* \quad (4.4 - 21)$$

7. These solutions are supplied to the aerodynamic model and used to compute the aerodynamic forces and moments.

8. The right-hand sides of equations 4.4-1 are re-evaluated at the new time ($t = t_i + \Delta t$).

9. The iteration number, k, is set equal to k + 1

10. Hamming's corrector is used to compute the corrected solutions, ${}^k y_{j,1}$; namely

$${}^k y_{j,1} = \frac{1}{8} [9y_{j,2} - y_{j,4} + 3\Delta t(9f_{j,1} + 19f_{j,2} - 5f_{j,3} + f_{j,4})] \quad \text{for } j = 1, 2, \dots, n \quad (4.4 - 22)$$

where $f_{j,1} = f_j(t_i + \Delta t, {}^{k-1}y_1(t_i + \Delta t), {}^{k-1}y_2(t_i + \Delta t), \dots, {}^{k-1}y_n(t_i + \Delta t))$

11. The absolute value of the difference between the solutions at the present and previous iterations, ${}^k e_j$, is estimated as follows:

$${}^k e_j = |{}^k y_{j,1} - {}^{k-1} y_{j,1}| \quad \text{for } j = 1, 2, \dots, n \quad (4.4 - 23)$$

12. ϵ_j is checked to determine if all its components are less or equal to the error tolerance. If the condition is not satisfied the computation process is repeated starting at step 7 until the solutions converge.

13. After the solutions converged, the truncation error, $\epsilon_{j,i+1}$, is estimated as follows:

$$\epsilon_{j,i+1} = \frac{9}{121} (y_{j,i+1}^k - y_j^p) \quad \text{for } j = 1, 1, \dots, n \quad (4.4 - 24)$$

14. The corrected solutions, $y_{j,i+1}^k$, are modified by using the new truncation-error estimates $\epsilon_{j,i+1}$, (see equation 4.4-24 above)

$$y_{j,i+1}^k = y_{j,i+1}^k - \epsilon_{j,i+1} \quad \text{for } j = 1, 2, \dots, n \quad (4.4 - 25)$$

15. Finally, the time is set equal to $t_i + \Delta t$. The process may be repeated for the next time step starting at step 1. The above algorithm is summarized by the flow chart in figure 56.

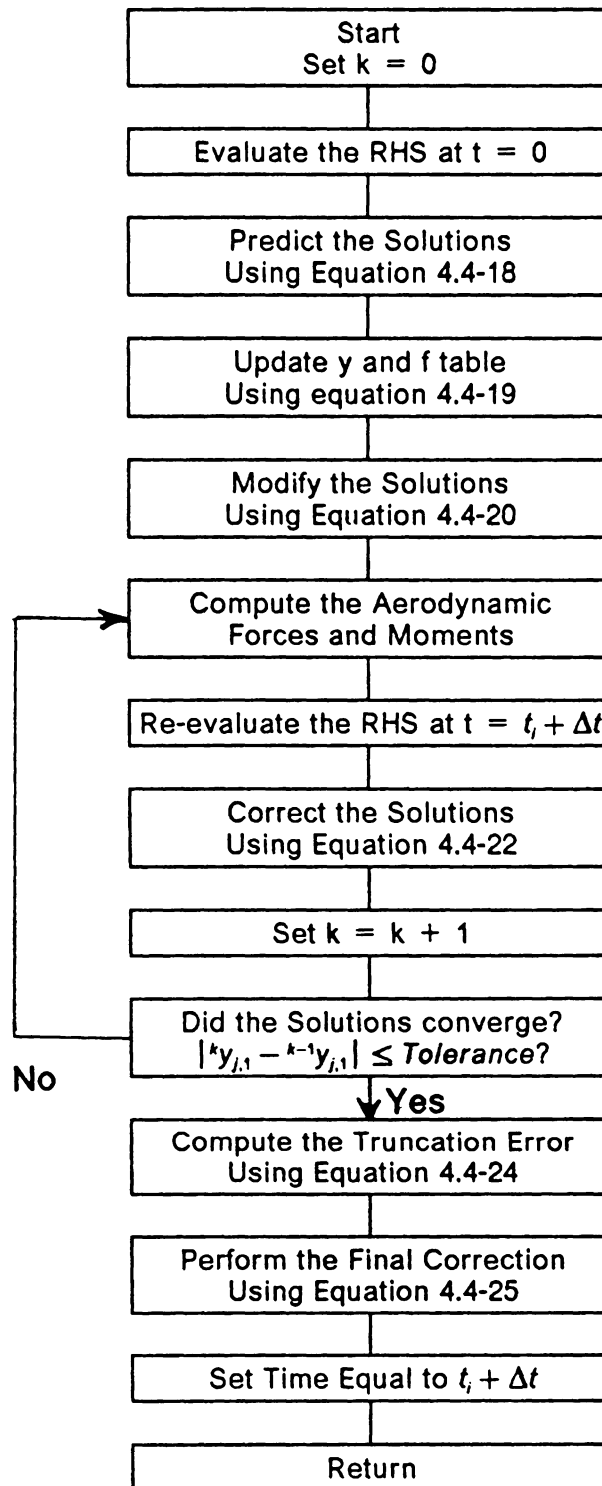


Figure 56. Flow chart for the general-predictor-corrector method

4.3.3 Aerodynamic-Dynamic model

The methods of section 4.3.1 were incorporated into the aerodynamic model of chapter II to form the aerodynamic-dynamic model. In this research, we limit consideration to only the pitch equation. The airplane is assumed to be moving at a constant speed in level flight and can only pitch about an axis that passes through the center of mass.

4.3.4 Numerical Examples

In this chapter, we simulate a wing and tail configuration that approximately resembles the Cessna 182 airplane. The physical quantities used for this simulation are given in Smetana (1984) and are shown in table 1.

Table 1. Physical quantities used for the simulation of Cessna 182 airplane taken from Smetana (1984).

ρ	$0.00205 \frac{\text{slug}}{\text{ft}^3}$
I_{yy}	1346.00000 slug-ft ²
A_{wing}	174.00000 ft ²
b_{wing}	35.83000 ft
C_{wing}	4.85627 ft
A_{tail}	38.71000 ft ²
b_{tail}	11.54000 ft
C_{tail}	3.35442 ft
Center of Gravity to Tail Quarter-Chord Position	14.60000 ft
Center of Gravity to Wing Quarter-Chord Position (Horizontal)	0.11000 ft
Center of Gravity to Wing Quarter-Chord Position (Vertical)	1.67000 ft

The wing and tail are considered to be rectangular planar lifting surfaces. The whole control surface is assumed to rotate about an axis that passes through the quarter-chord position. Accordingly, the hinge moment is taken about the quarter-chord position. The control surface was discretized into three rows in the chordwise direction. The nondimensional chordwise increment of the control surface is chosen to be one. Accordingly, the physical length of the chordwise increment of

the bound lattice, L , is 1.11814 feet. From table 1 and the value of L , we find that C_s is 0.000804.

In figure 57, the plots of the elevator-deflection angle (trim map), lift coefficient, drag coefficient and hinge-moment coefficient as functions of the pitch angle are shown at trim in and out of ground effect. By the term trim map, we mean the plot of the deflection angles of the tail, δ , as functions of the pitch angles of the main wing, θ , for zero pitching moment about an axis that passes through the center of mass of the airplane. Clearly, the effect of the ground is to lower the effectiveness of the control surface in controlling the pitch motion. Namely, for the same pitch angle, the control surface has to be deflected more near the ground which may mean that an airplane capable of being trimmed at all altitudes far from the ground cannot be trimmed near the ground because of insufficient elevator control. The effect of the ground increases the lift and drag coefficients and makes the hinge-moment coefficient less negative.

In figure 58, the plots of the pitch angle, elevator-deflection angle, pitching-moment coefficient, hinge-moment coefficient, lift coefficient and drag coefficient as functions of the dimensionless time are shown out of the ground effect. The airplane was in equilibrium when $\delta = -2^\circ$. The corresponding θ was 3.1° . The elevator-deflection angle was changed from -2° to -4° as a step change in order to change the pitch angle from 3.1° to 6.1° .

In figure 59, the plots of the pitch angle, elevator-deflection angle, pitching-moment coefficient, hinge-moment coefficient, lift coefficient and drag coefficient as functions of the dimensionless time are shown in the ground effect. The airplane was in equilibrium when $\delta = -2^\circ$. The corresponding θ was 2.3° . The elevator-deflection angle was changed from -2° to -4° as a step change in order to change the pitch angle from 2.3° to 4.6° . Similar results are shown in figure 60

when the elevator-deflection angle was changed from -2.7° to -5.4° as a step change in order to change the pitch angle from 3.1° to 6.1° . Clearly, the pitch angle responds faster and overshoots more near the ground than it does far from the ground.

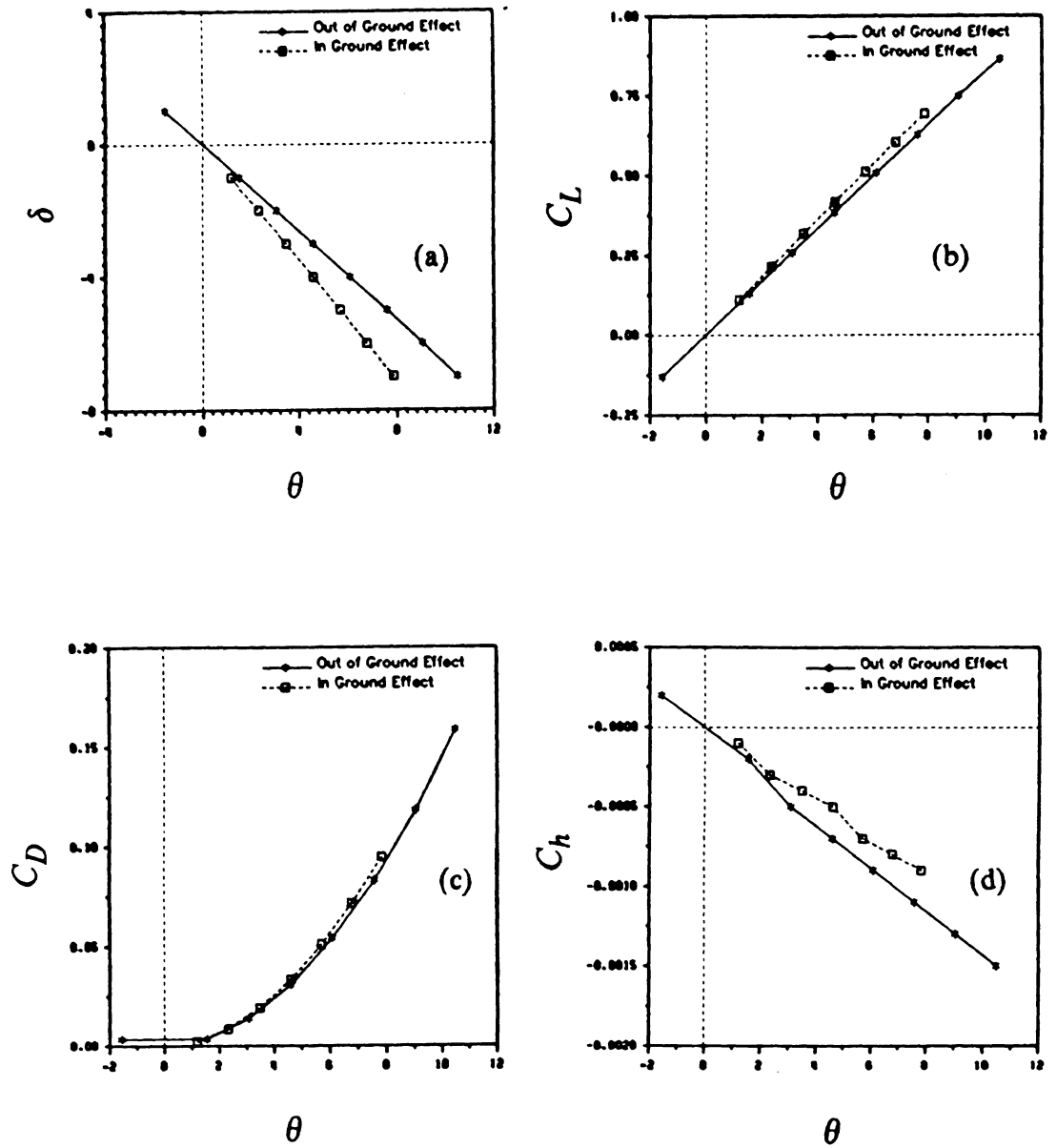


Figure 57. Aerodynamic characteristic at trim in and out of ground effect for steady flows: (a) elevator-deflection angle (trim map), (b) lift coefficient, (c) drag coefficient and (d) hinge-moment coefficient as functions of the pitch angle for zero pitching moment about the center of gravity.

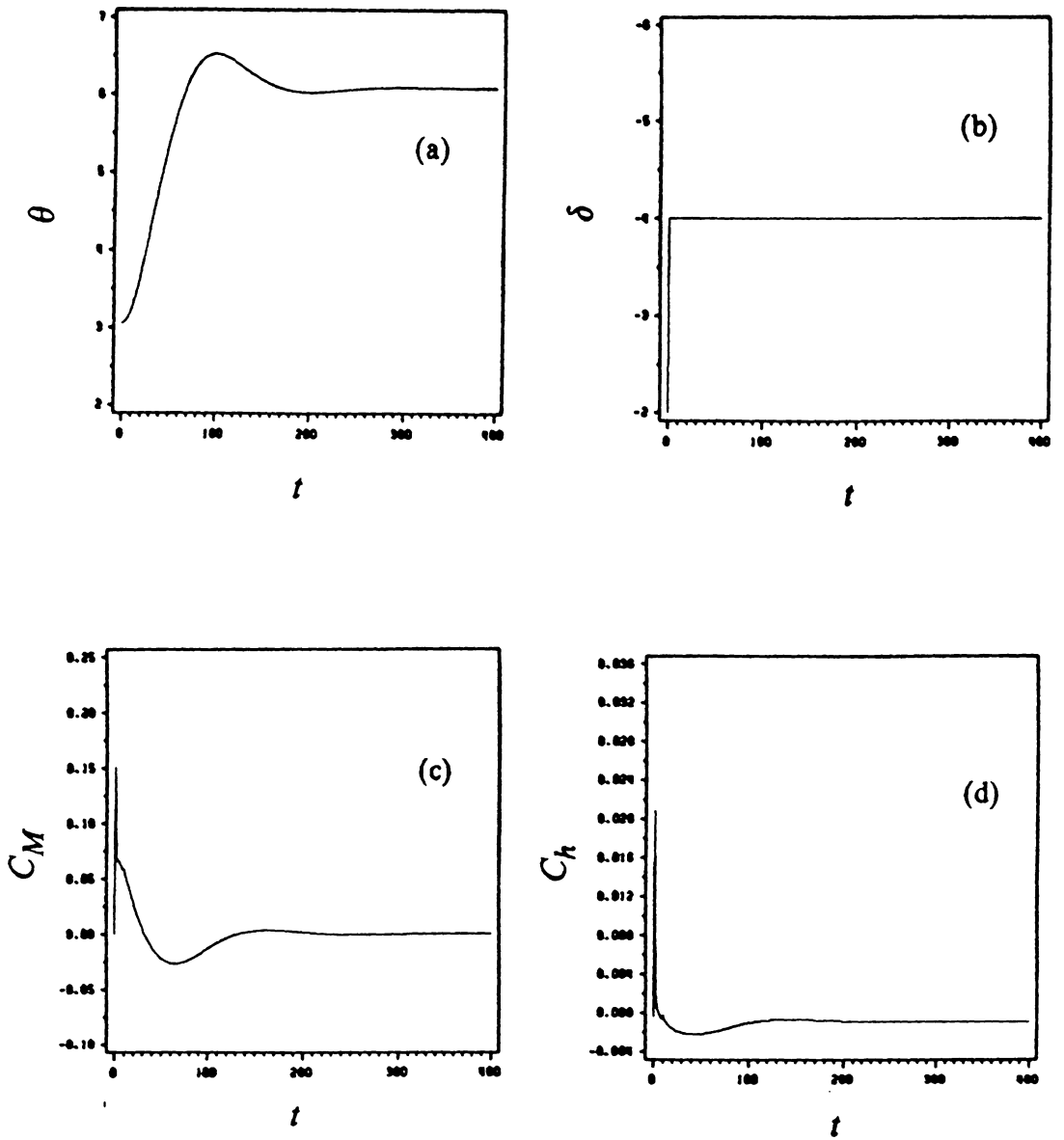


Figure 58. Pitch change out of ground effect: (a) pitch angle, (b) elevator deflection angle, (c) pitching-moment coefficient, (d) hinge-moment coefficient, (e) lift coefficient and (f) drag coefficient as functions of the dimensionless time.

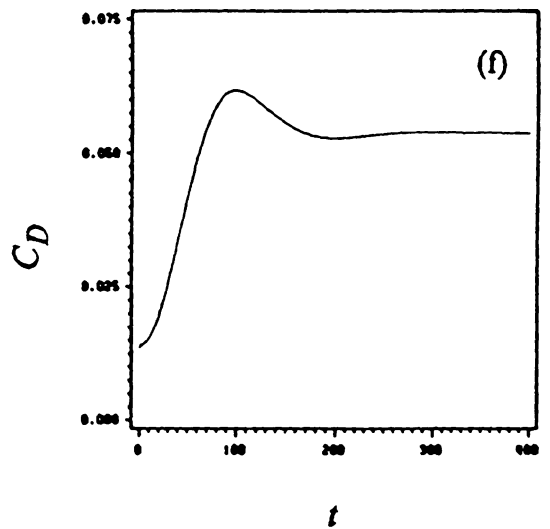
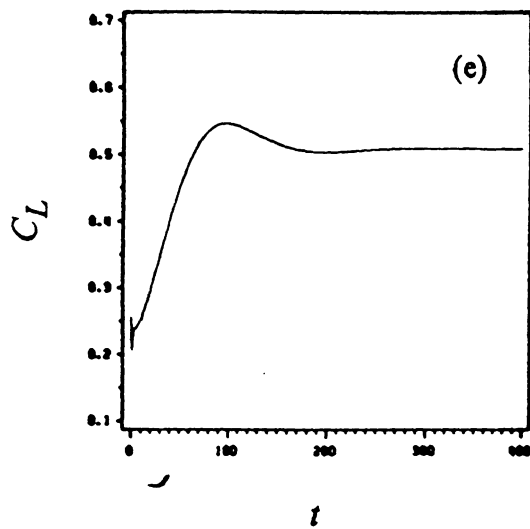


Figure 58. Continued.

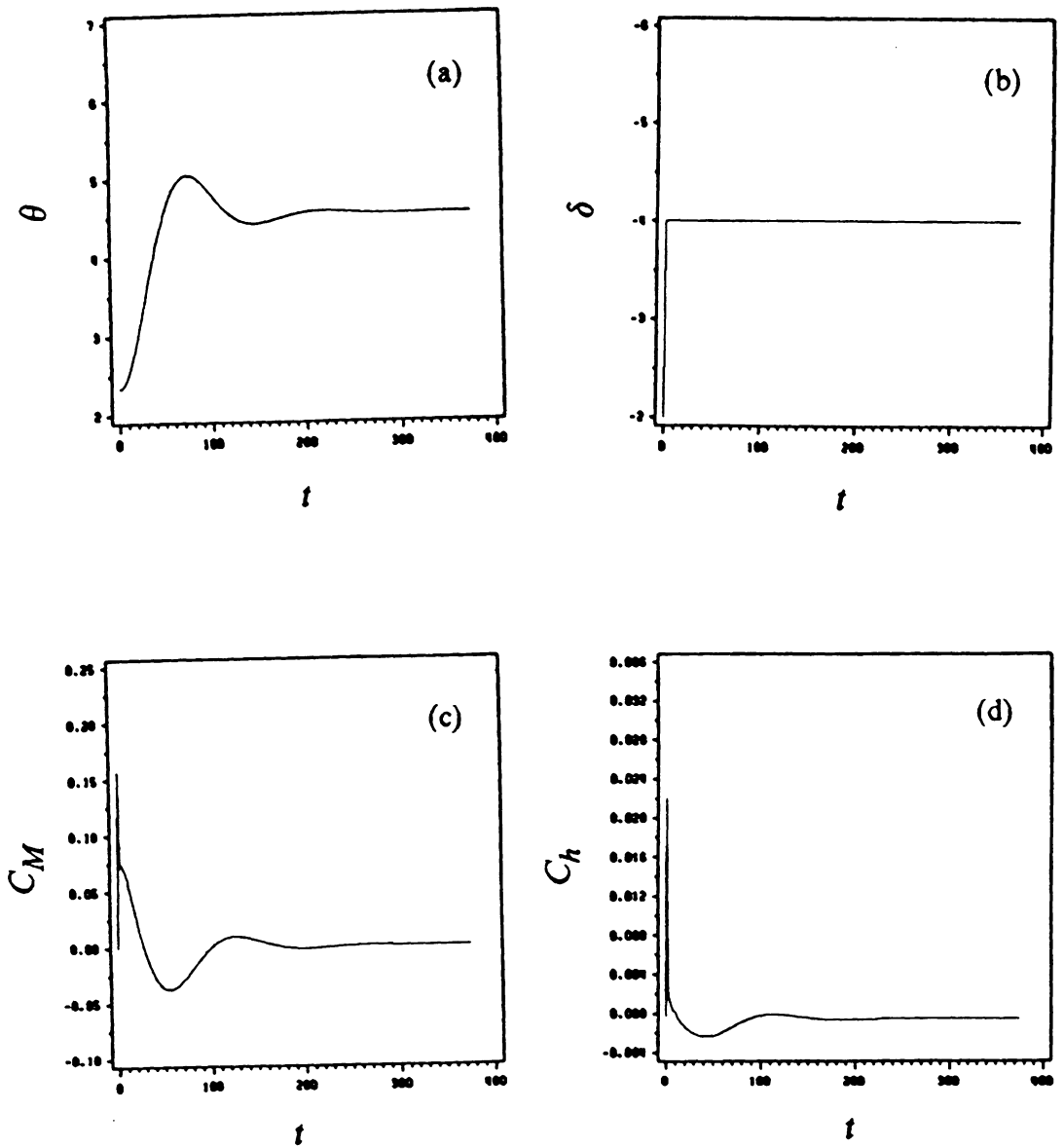


Figure 59. Pitch change in ground effect: (a) pitch angle, (b) elevator-deflection angle, (c) pitching-moment coefficient, (d) hinge-moment coefficient, (e) lift coefficient and (f) drag coefficient as functions of the dimensionless time.

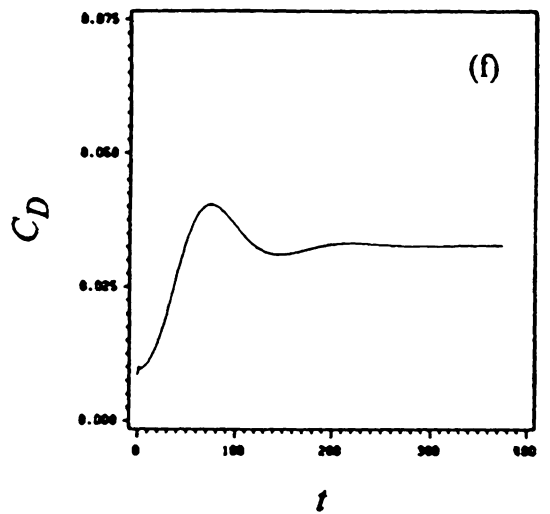
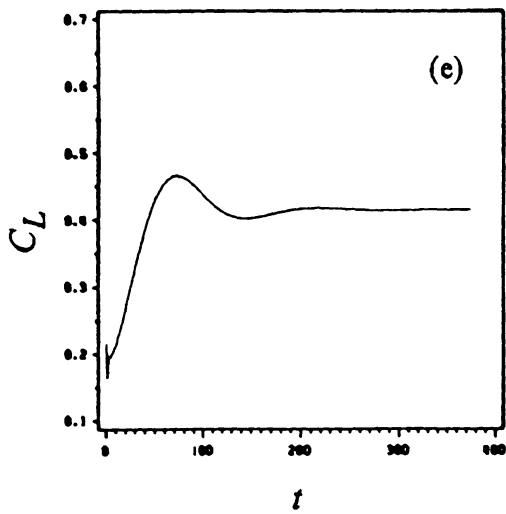


Figure 59. Continued.

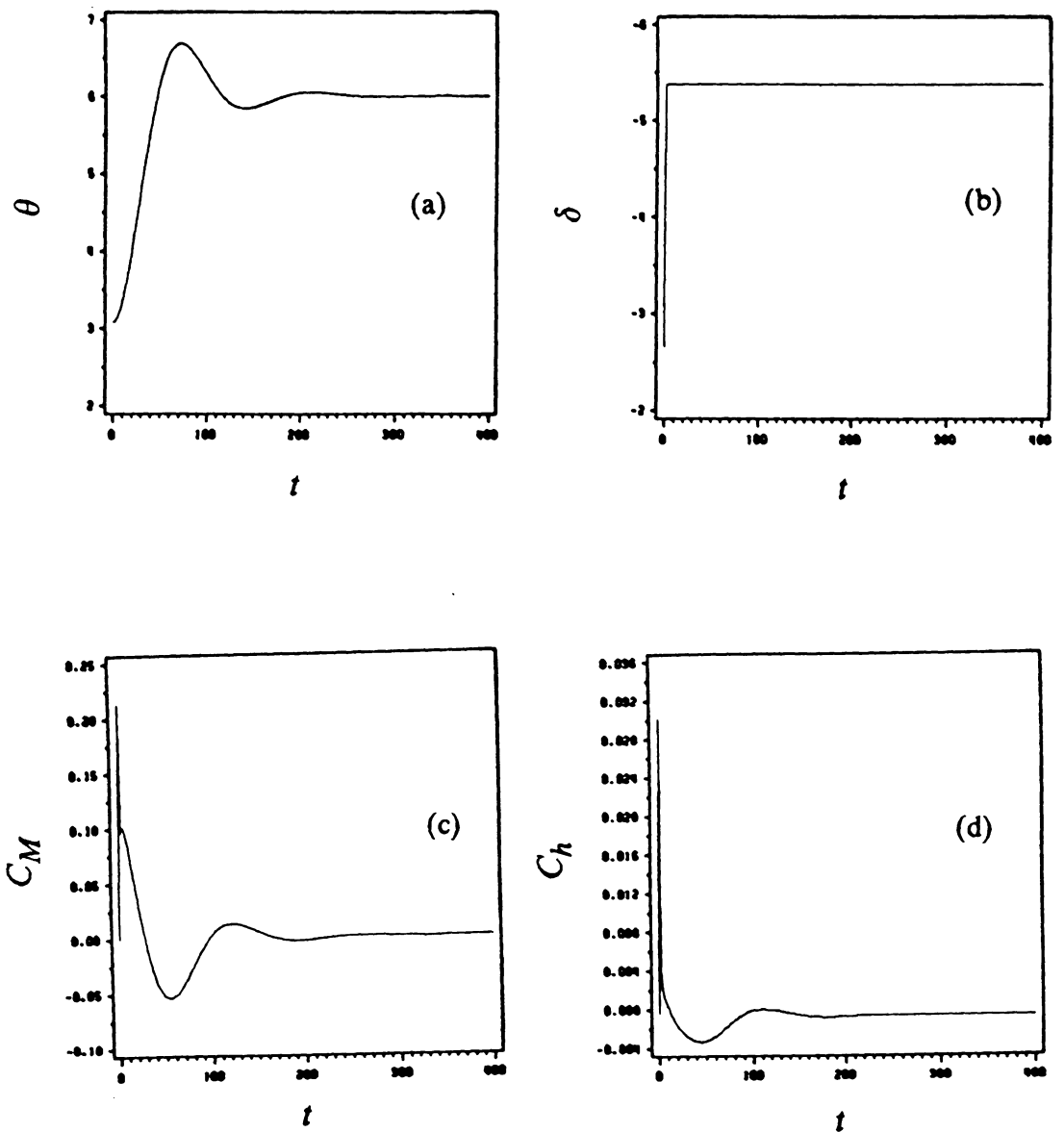


Figure 60. Pitch change in ground effect: (a) pitch angle, (b) elevator-deflection angle, (c) pitching-moment coefficient, (d) hinge-moment coefficient, (e) lift coefficient and (f) drag coefficient as functions of the dimensionless time.

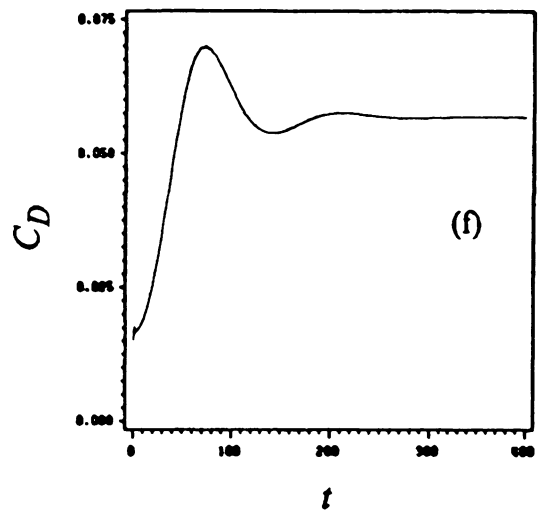
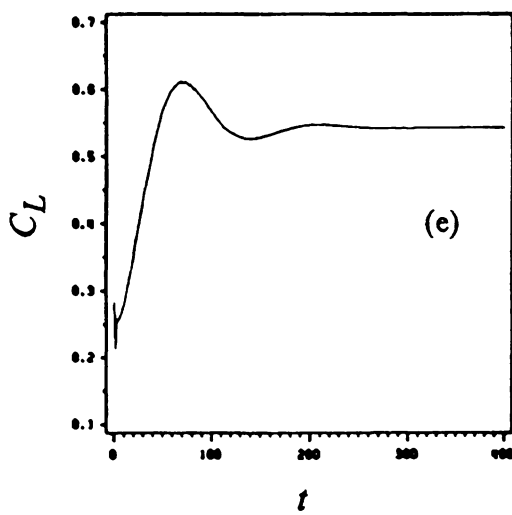


Figure 60. Continued.

4.4 Feedback Control

The ultimate goal of this research is to be able to predict the control-surface motion that will cause an aircraft to execute a prescribed maneuver. In the preceding sections, the aerodynamic model of chapter II was coupled with the equations of motion. The resulting numerical simulation (aerodynamic-dynamic model) was used to compute the trim map of a configuration that approximately resembles the Cessna 182 in and out of ground effects. In this section, we describe the addition of a feedback-control system to the aerodynamic-dynamic model.

In the aerodynamic-dynamic model, the elevator deflection, δ , was specified at the beginning of computations and kept fixed all the time. In this section, on the other hand, the elevator-deflection angle will be specified as functions of the pitch angle and its rate. As a result, the elevator-deflection angle is changing during the course of computations. In the present simulation, we confine the analysis to the control of an aircraft during a level flight. The theory can be generalized to include the control of an aircraft during landing maneuvers. We assume that the aircraft is supported at the center of gravity and moves forward at constant speed parallel to the ground. As a result, the equations of motion reduce to the pitching moment equation only. That is

$$\ddot{\theta} = C_3 C_M \quad (4.5 - 1)$$

with the initial conditions

$$\theta(0) = \theta_0 \text{ and } \dot{\theta} = 0 \quad (4.5 - 2)$$

The pitching moment coefficient, C_M , is in general a function of θ , $\dot{\theta}$, δ and $\dot{\delta}$. That is

$$C_M = C_M(\theta, \dot{\theta}, \delta, \dot{\delta}) \quad (4.5 - 3)$$

where θ and δ denote the pitch and elevator-deflection angles, respectively. The dot denotes the derivative with respect to the dimensionless time. Etkin (1982) pointed out that the autopilot and control system are fast-acting compared to the pitch response of the vehicle. As a result, we further neglect the dynamics of the elevator. That is no lag exist between the command and the elevator-deflection angle. The pitching-moment coefficient, equation 4.5-3, becomes

$$C_M = C_M(\theta, \dot{\theta}, \delta) \quad (4.5 - 4)$$

The aim is to be able to reach the final state rapidly and with small oscillation. We employ proportional and rate control laws. That is,

$$\Delta\delta = K_1\Delta\theta + \Delta\dot{\theta} \quad (4.5 - 5)$$

where $\Delta\delta = \delta - \delta_f$, $\Delta\theta = \theta - \theta_f$, and $\Delta\dot{\theta} = \dot{\theta} - \dot{\theta}_f$, in which δ_f is the final elevator deflection, θ_f is the final pitch angle, and $\dot{\theta}_f$ is the rate of the final pitch angle (zero in this dissertation). From equation 4.5-5, the elevator-deflection angle is given by

$$\delta = \delta_f + K_1(\theta - \theta_f) + K_2\dot{\theta} \quad (4.5 - 6)$$

The final elevator-deflection angle, δ_f , is computed at the beginning of the computations from the trim map. The computation is done by supplying the trim map in the form of data points to a subroutine that employs Lagrange interpolation as found in Carnahan et al. (1969). The final pitch angle, θ_f , is supplied as an input

argument to this subroutine. The subroutine returns the final elevator deflection, δ_f , that corresponds to a steady state at θ_f .

In order to obtain an estimate of the magnitudes and signs of the gains K_1 and K_2 , we linearized equation 4.5-4 using a Taylor series. Expanding C_M about the final state, we find the following

$$C_M = C_M(\theta_f, \dot{\theta}_f, \delta_f) + \frac{\partial C_M(\theta_f, \dot{\theta}_f, \delta_f)}{\partial \theta} (\theta - \theta_f) + \frac{\partial C_M(\theta_f, \dot{\theta}_f, \delta_f)}{\partial \dot{\theta}} (\dot{\theta} - \dot{\theta}_f) + \frac{\partial C_M(\theta_f, \dot{\theta}_f, \delta_f)}{\partial \delta} (\delta - \delta_f) + H.O.T \quad (4.5 - 7)$$

where H.O.T stands for the higher order terms. Equation 4.5-7 can be written as follows:

$$\Delta C_M = C_{M\theta}|_f \Delta\theta + C_{M\dot{\theta}}|_f \Delta\dot{\theta} + C_{M\delta}|_f \Delta\delta + H.O.T \quad (4.5 - 8)$$

where subscript f refers to the final state. We substitute equations 4.5-8 and 4.5-5 into equation 4.5-1. The resulting equation, after we neglect the higher order terms, is simply,

$$\Delta\ddot{\theta} = C_3 \left[(C_{M\theta}|_f + K_1 C_{M\delta}|_f) \Delta\theta + (C_{M\dot{\theta}}|_f + K_2 C_{M\delta}|_f) \Delta\dot{\theta} \right] \quad (4.5 - 9)$$

Equation 4.5-9 can be put in the following form:

$$\Delta\ddot{\theta} + 2\zeta\omega_n\Delta\dot{\theta} + \omega_n^2\Delta\theta = 0 \quad (4.5 - 10)$$

where

$$\omega_n^2 = -C_3(C_{M\theta}|_f + K_1 C_{M\delta}|_f) \quad (4.5 - 11)$$

and

$$2\zeta\omega_n = -C_3(C_{M\dot{\theta}}|_r + K_2 C_{M\delta}|_r) \quad (4.5 - 12)$$

ζ and ω_n are the damping coefficient and the frequency of oscillation, respectively.

The stability derivatives ($C_{M\theta}$, $C_{M\dot{\theta}}$, $C_{M\delta}$) have to be known before K_1 and K_2 can be evaluated. In order to compute the stability derivatives, we perturbed the wing about the final equilibrium state. That is, we let, for example, $\theta = \theta_r + \varepsilon$ with $\dot{\theta} = 0$ and $\delta = \delta_r$, and computed the pitching moment using the aerodynamic model of chapter II. $C_{M\theta}|_r$ was computed as follows:

$$C_{M\theta}|_r = \frac{C_M(\theta_r + \varepsilon, 0, \delta_r) - C_M(\theta_r, 0, \delta_r)}{(\theta_r + \varepsilon) - \theta_r} \quad (4.5 - 13)$$

Similarly, $C_{M\dot{\theta}}|_r$ and $C_{M\delta}|_r$ are computed. Table 2 shows the stability derivatives for various ε . In table 2, $\theta_r = 6.1^\circ$, $\dot{\theta}_r = 0$ and $\delta = -4$. Clearly, the effect of the perturbation parameter is weak.

Table 2. The stability derivatives

$\varepsilon, ^\circ$	$C_{M\theta} _r$	$C_{M\dot{\theta}} _r$	$C_{M\delta} _r$
0.1	-1.7241	-37.1824	-2.5715
-0.1	-1.7231	-36.9628	-2.5722
1.0	-1.7059	-40.7438	-2.5753
-1.0	-1.7206	-38.6121	-2.5688

The derivatives $C_{M\theta}|_r$, $C_{M\dot{\theta}}|_r$ and $C_{M\delta}|_r$ were chosen to be -1.72, -38.0 and -2.57, respectively. When these values and $C_3 = 0.000804$ are substituted into equations 4.5-11 and 4.5-12, those equations become

$$\omega_n^2 = 0.000804(2.72 + 2.57K_1) \quad (4.5 - 14)$$

and

$$2\zeta\omega_n = 0.000804(38.0 + 2.57K_2) \quad (4.5 - 15)$$

The gains K_1 and K_2 are computed from equations 4.5-14 and 4.5-15 by specifying the damping coefficient and the frequency of oscillation. The damping coefficient should be between 0.5 and 0.8 in order for the control surface to respond fast. The frequency of oscillation is on the order of 3 rad/sec. In figure 61, the plots of the pitch angle, elevator-deflection angle, pitching-moment coefficient, hinge-moment coefficient, lift coefficient and drag coefficient as functions of the dimensionless time are shown out of the ground effect for various feedback gains. The elevator-deflection angle was changed from -2° to -4° in order to change the pitch angle from 3.1° to 6.1° . Clearly, of the feedback gains considered, the best are $K_1 = 0.15$ and $K_2 = 13.06$. The response is fast with little overshoot. These dimensionless gains are used for the following plots.

In figure 62, the plots of the pitch angle, elevator-deflection angle, pitching-moment coefficient, hinge-moment coefficient, lift coefficient and drag coefficient as functions of the dimensionless time are shown for an airplane out of the ground effect. The elevator-deflection angle was changed from -2° to -4° in order to change the pitch angle from 3.1° to 6.1° . Similar results are shown in figure 63 when the elevator-deflection angle was changed from -2° to -3.3° in order to change the pitch angle from 3.1° to 5° .

In figure 64, the plots of the pitch angle, elevator-deflection angle, pitching-moment coefficient, hinge-moment coefficient, lift coefficient and drag coefficient as functions of the dimensionless time are shown in ground effect. The elevator-deflection angle was changed from -2° to -4° in order to change the pitch angle from 2.3° to 4.6° . Similar results are shown in figure 65 when the elevator-deflection angle was changed from -2.7° to -5.4° in

order to change the pitch angle from 3.1° to 6.1° . Clearly, the pitch angle responds fast and overshoots more near the ground than it does far from the ground.

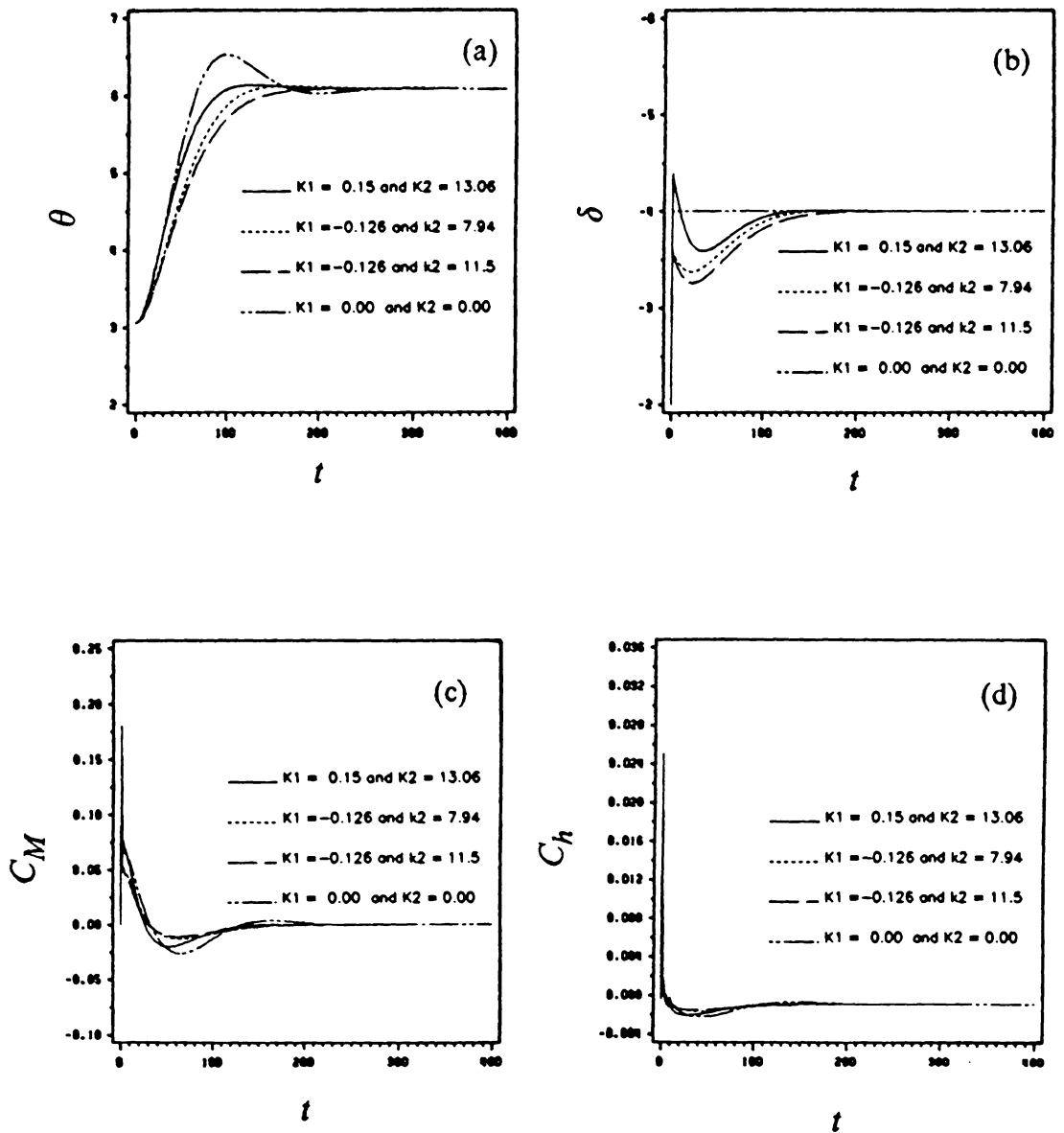


Figure 61. Pitch change out of ground effect for various gains of the feedback-control system: (a) pitch angle, (b) elevator-deflection angle, (c) pitching-moment coefficient, (d) hinge-moment coefficient, (e) lift coefficient and (f) drag coefficient as functions of the dimensionless time.

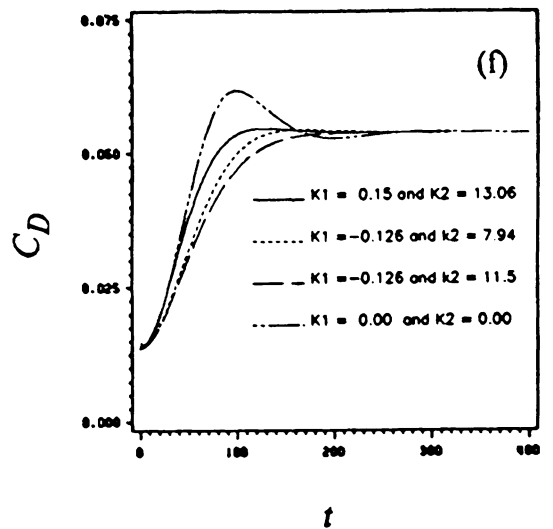
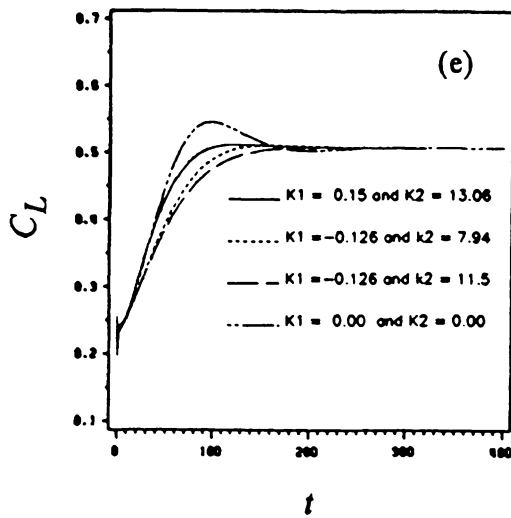


Figure 61. Continued.

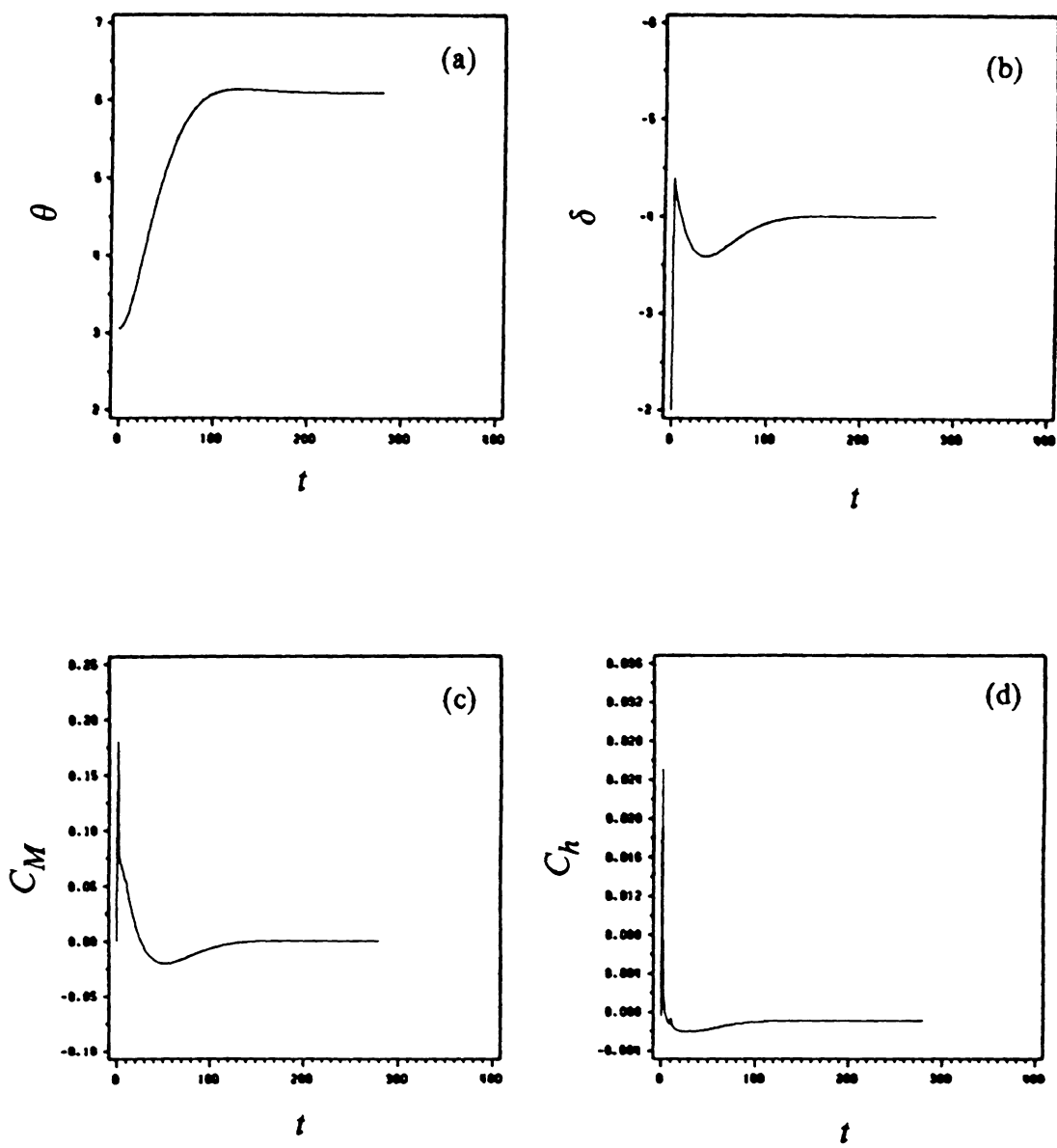


Figure 62. Pitch change with feedback control out of ground effect: (a) pitch angle, (b) elevator-deflection angle, (c) pitching-moment coefficient, (d) hinge-moment coefficient, (e) lift coefficient and (f) drag coefficient as functions of the dimensionless time.

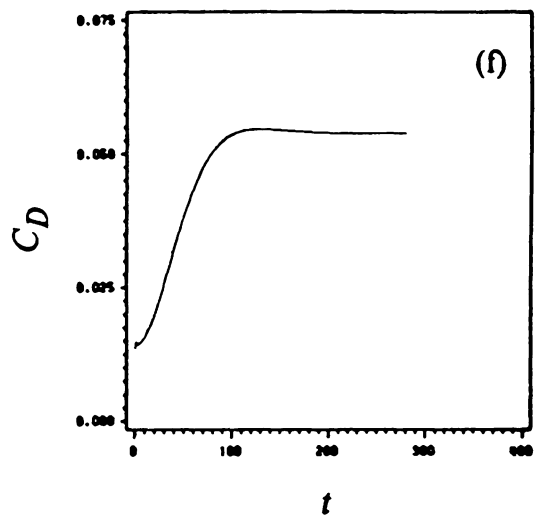
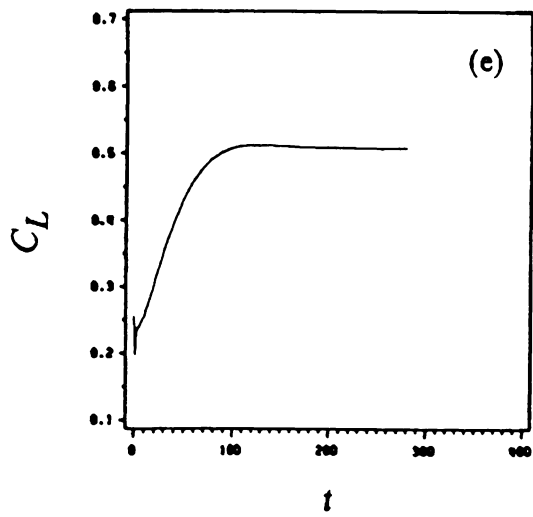


Figure 62. Continued.

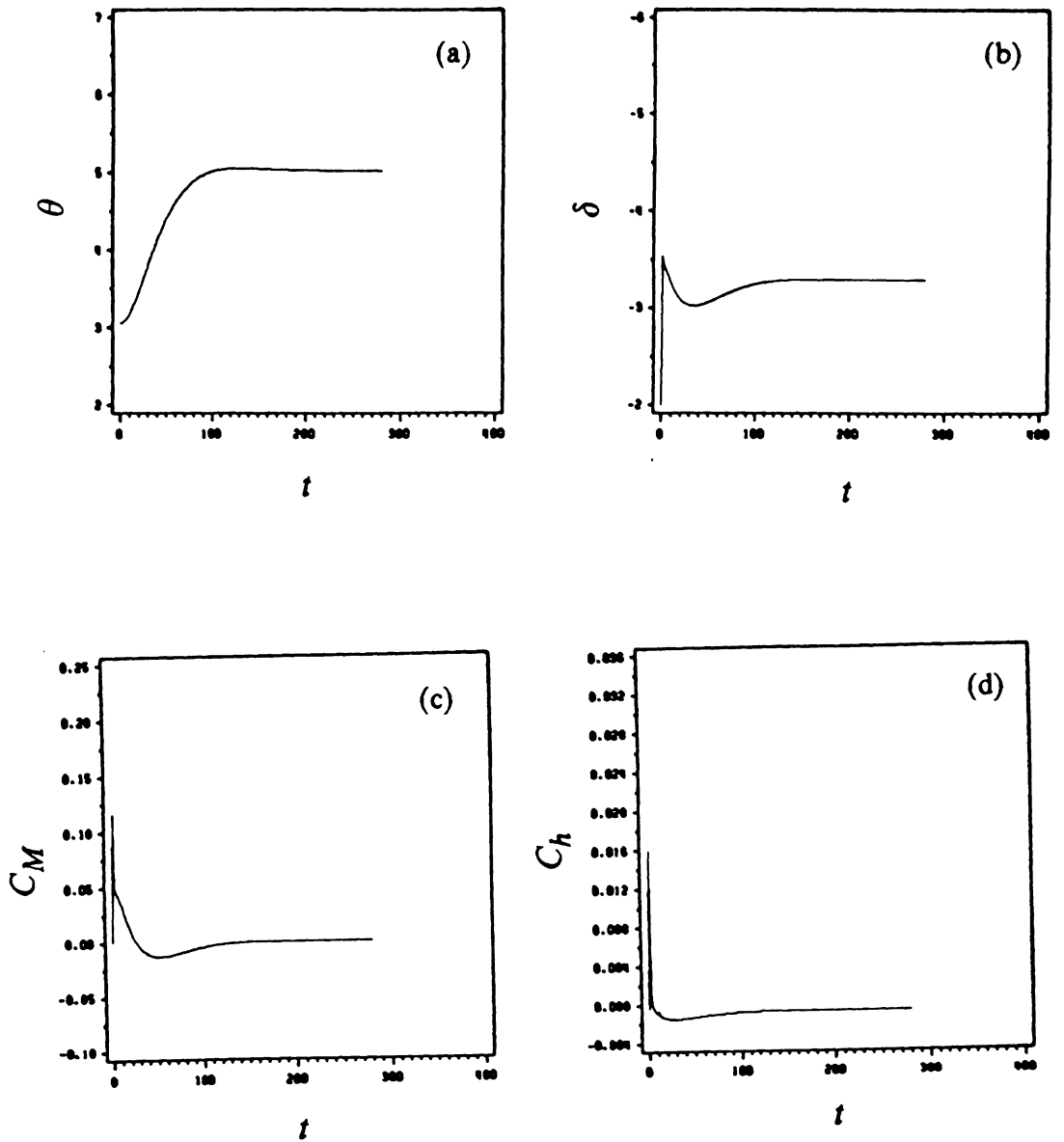


Figure 63. Pitch change with feedback control out of ground effect: (a) pitch angle, (b) elevator-deflection angle, (c) pitching-moment coefficient, (d) hinge-moment coefficient, (e) lift coefficient and (f) drag coefficient as functions of the dimensionless time.

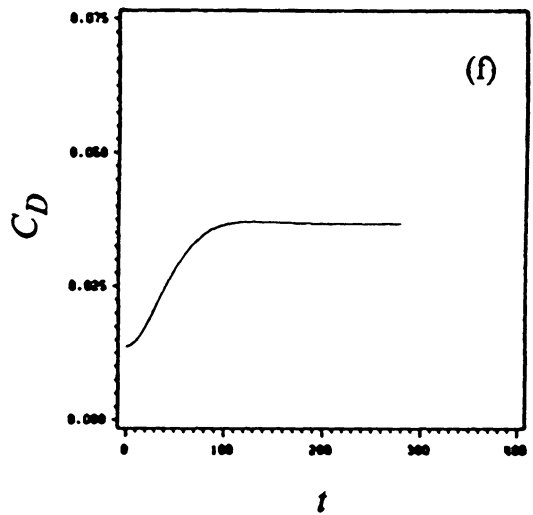
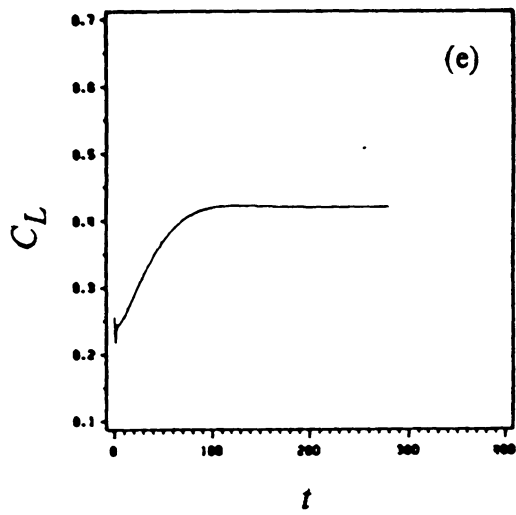


Figure 63. Continued.

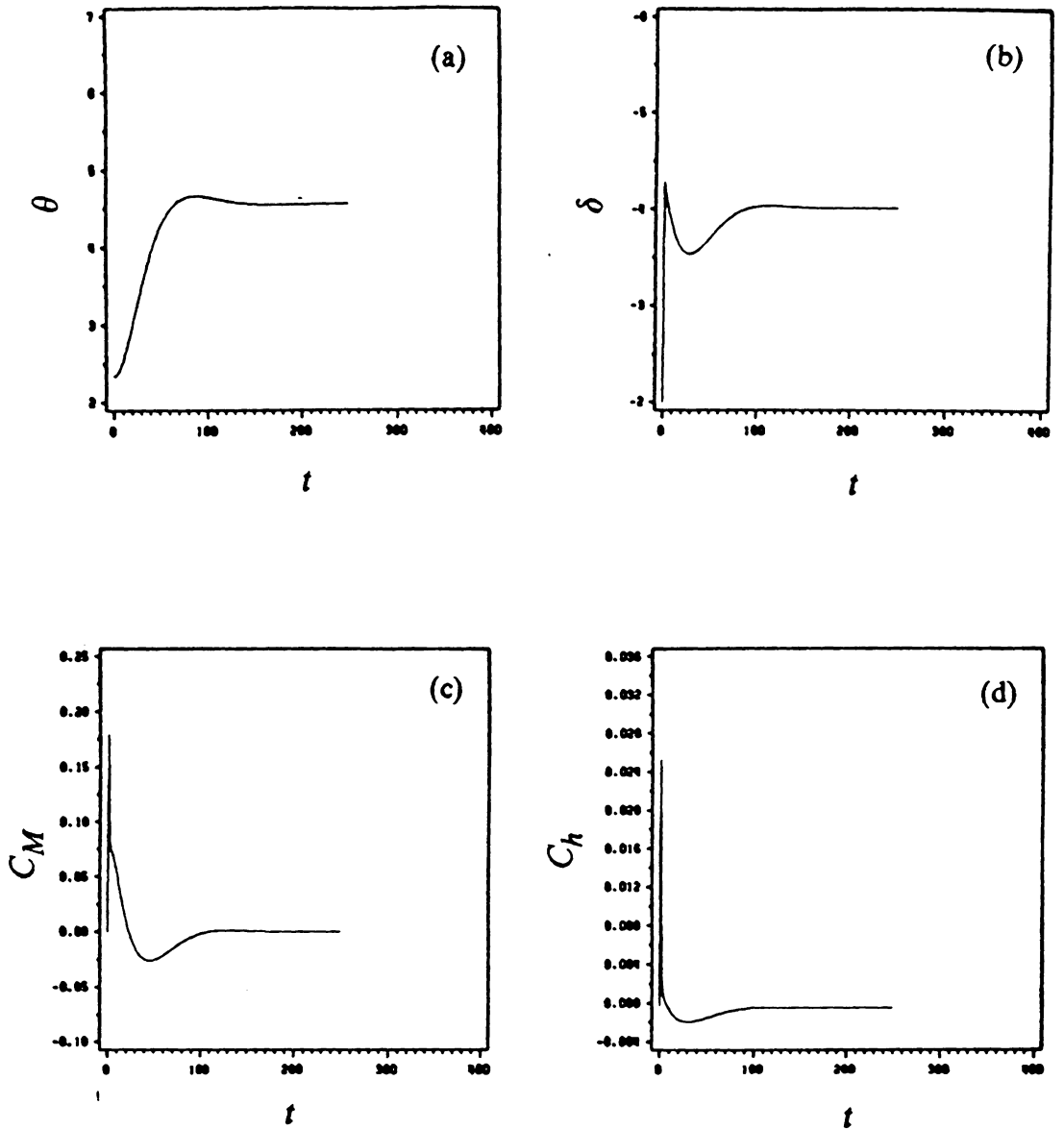


Figure 64. Pitch change with feedback control in ground effect: (a) pitch angle, (b) elevator-deflection angle, (c) pitching-moment coefficient, (d) hinge-moment coefficient, (e) lift coefficient and (f) drag coefficient as functions of the dimensionless time.

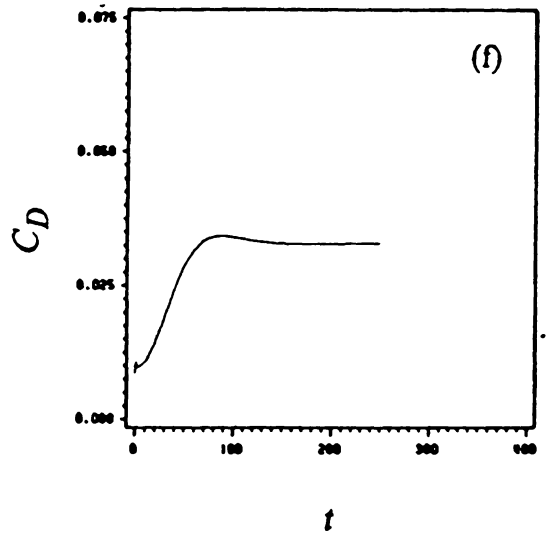
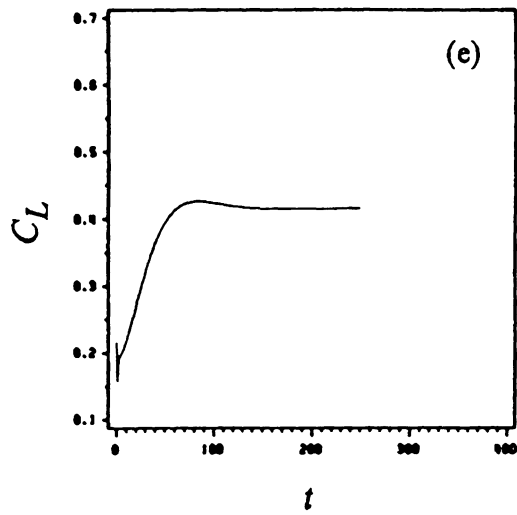


Figure 64. Continued.

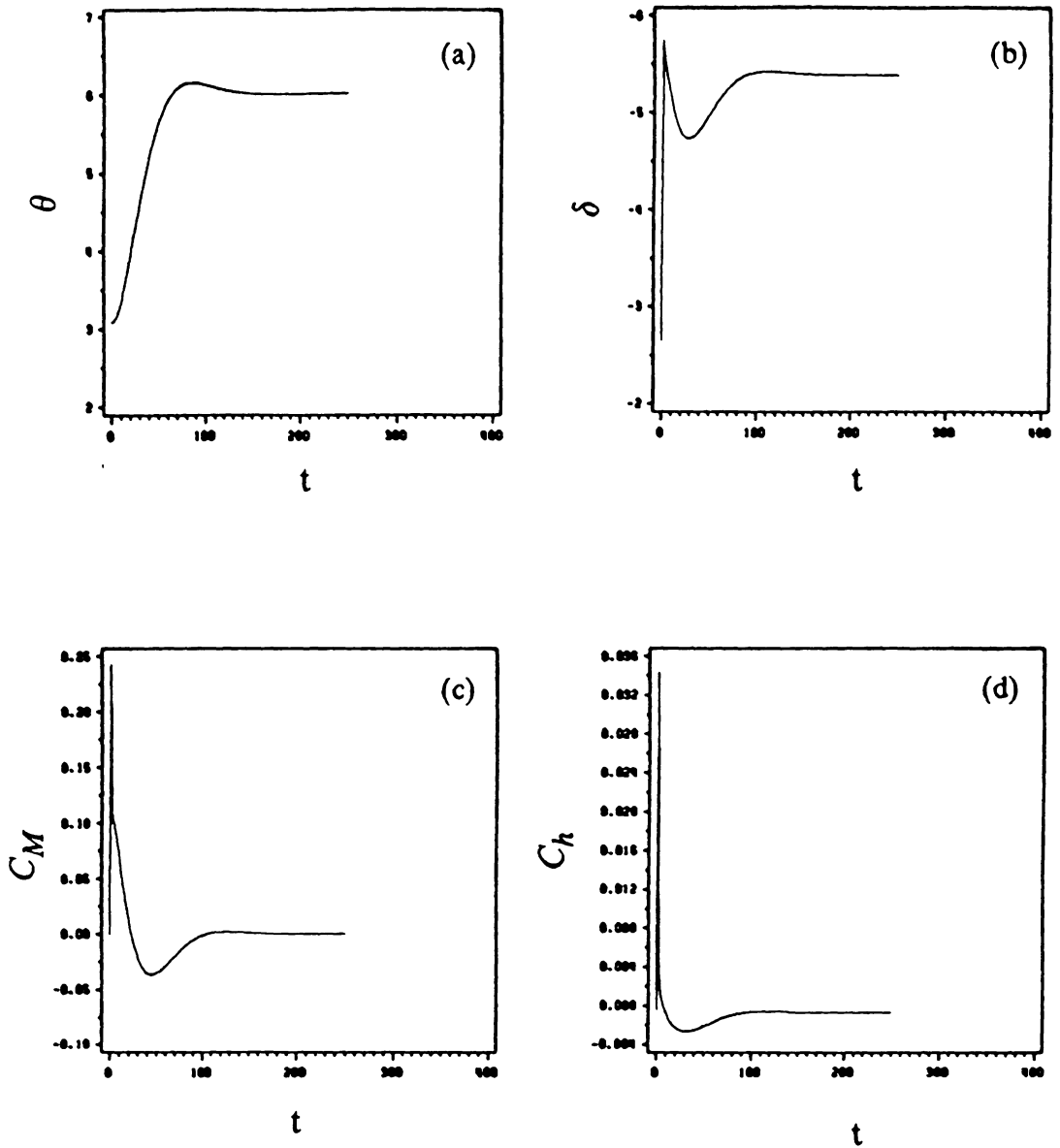


Figure 65. Pitch change with feedback control in ground effect: (a) pitch angle, (b) elevator-deflection angle, (c) pitching-moment coefficient, (d) hinge-moment coefficient, (e) lift coefficient and (f) drag coefficient as functions of the dimensionless time.

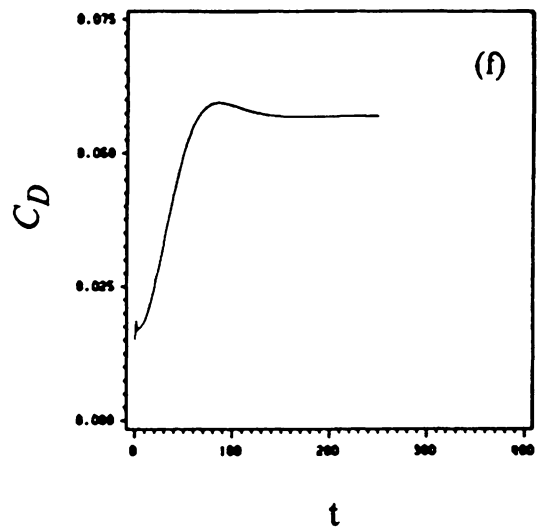
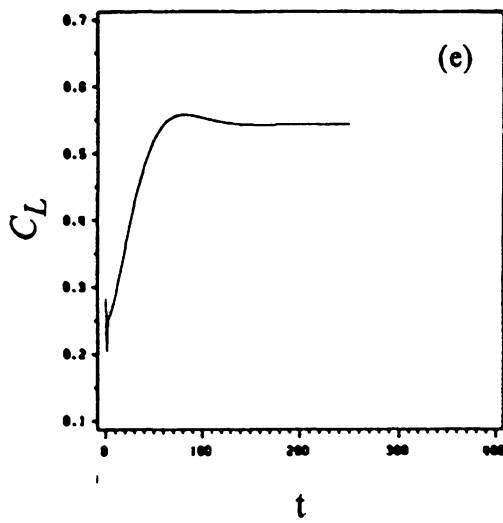


Figure 65. Continued.

Chapter V

Conclusions and Recommendations

A general nonlinear unsteady numerical simulation of control of an aircraft in and out of ground effect is developed. The development occurred in three stages:

1. A general aerodynamic model of closely coupled lifting surfaces in ground effect was developed.
2. The aerodynamic model was coupled with the equations of motion to simulate aerodynamic-dynamic interactions.
3. The aerodynamic-dynamic model was coupled with a feedback system to predict the response of an aircraft to control inputs both in and out of ground effect.

The aerodynamic model is based on the general unsteady vortex-lattice method and the method of images. It is not restricted by planform, angle of attack, sink rate, dihedral angle, twist, camber, etc. as long as stall or vortex bursting does not occur. The aerodynamic model provides the wakes adjoining the wing tips and trailing edges of rectangular wings and the

leading and trailing edges of delta wings. It has the versatility needed to model steady and unsteady aerodynamic interference among multiple closely coupled lifting surfaces and fully accounts for the mutual interference of trailing wakes and downstream lifting surfaces. Furthermore, the present model can be used to simulate any prescribed flare and to model the effects of cross and/or head winds near the ground.

The aerodynamic model was used to study the steady and unsteady ground effects on lifting surfaces of different planforms. The ground restricts the downward movement of the wake and causes it spread. The present results show the influences of various parameters on the aerodynamic coefficients for both steady and unsteady flows. Generally, the present technique predicts higher aerodynamic coefficients near the ground for the unsteady cases than for the steady ones; the greater the sink rates, the stronger the effects. Increasing the aspect ratio increases both the steady and unsteady ground effects for both rectangular and delta planforms. An exception is a large aspect-ratio wing (here we consider a two-dimensional wing) with large camber. Such a wing actually experiences a loss of lift and pitching moment (about the trailing edge) near the ground.

The present computed results are generally in close agreement with limited exact solutions and experimental data, and they serve to demonstrate the potential of the present approach. The present study demonstrates the importance of including unsteady ground effects when analyzing the performance of an airplane during a landing maneuver. Furthermore, it also points out the necessity, in the future, of developing wind-tunnel techniques for studying the unsteady ground effects.

In the aerodynamic-dynamic simulation, the equations of motion were solved by Hamming's predictor-corrector method. This method requires the solutions to be known at four previous time steps. As a result, different predictor-corrector methods were employed to generate solutions at the start of the motion. Here, we are computing a final steady-state solution, and hence it is essential to have good accuracy at all times. In an earlier numerical simulation of wing rock, an arbitrary initial disturbance was introduced; hence, it was not necessary to compute the solution accurately at the first three or four time steps. In the

present simulation, the equations of motion for the aircraft and for the flowing air and the equations describing the control system are integrated simultaneously and interactively. The aircraft, its control system, and the air stream are considered a single dynamic system. At any instant, the aerodynamic loads are computed by considering the motions of the aircraft and its control surfaces at that instant by considering the recent histories of these motions. The history resides in the wakes of the various lifting surfaces. The aerodynamic-dynamic model was used to study a wing and tail configuration that approximately resembles a Cessna 182 airplane. It was found that the effect of the ground lowers the effectiveness of the elevator in controlling the pitch motion. Namely, for the same pitch angle, the control surface has to be deflected more near the ground than far from the ground. Consequently, it is possible that an airplane capable of being trimmed at an altitude far from the ground could be difficult to trim near the ground because of insufficient elevator control. The effect of the ground increases the lift and drag coefficients and makes the hinge-moment coefficient less negative. The pitch angle responds faster and overshoots more near the ground than it does far from the ground.

We used proportional and rate laws. One set of gains was used in and out of ground effect. It was found that the pitch angle responds faster and overshoots more near the ground than it does far from the ground. The present results demonstrate the feasibility of using the current simulation for more complicated motions. As a result, the present simulation should be extended to simulate the control of an aircraft during a landing maneuver by considering at least three degrees of freedom.

References

- Abercrombie, J. M., "The Lift of High Circulation Wings in Ground Effect," M. S. Thesis, Saint Louis University, Saint Louis, Missouri, 1967.
- Bagley, J. A., "The Pressure Distribution on Two-Dimensional Wings near the Ground," A.R.C Reports and Memorandum no. 3238, 1961.
- Baker, P. A., Schweikhard, W. G., and Young, W. R., "Flight-Evaluation of Ground Effect on Several Low-Aspect-Ratio Airplanes," NASA TN D-6053, Oct. 1970.
- Bartlett, G. E. and Vidal, R. J., "Experimental Investigation of Influence of Edge Shape on the Aerodynamic Characteristics of Low Aspect Ratio Wings at Low Speeds," Journal of the Aeronautical Sciences, Vol. 22, August 1955, pp. 517-533 and 588.
- Blakelock, J. H., *Automatic Control of Aircraft and Missiles*, John Wiley and Sons, Inc., New York, New York, 1965.
- Burden, R. L., Faires, J. D. and Reynolds, A. C., *Numerical Analysis*, Prindle, Weber and Schmidt, Boston, Massachusetts, 1981.
- Buell, D. A. and Tinning, B. E., "Ground Effects on the Longitudinal Characteristics of Two Models with Wings Having Low Aspect Ratio and Pointed Tips," NACA TN 4044, 1957.
- Carnahan, B., Luther, H. A. and Wilkes, J. O., *Applied Numerical Methods*, John Wiley and sons, New York, New York, 1969.
- Carter, A. W., "Effect of Ground Proximity on the Aerodynamic Characteristics of Aspect-Ratio-1 Aerofoils with and without End Plates," NASA TN D-970, Oct. 1961.
- Chang, R. C., "An Experimental Investigation of Dynamic Ground Effect," Ph.D. Dissertation, Department of Aerospace Engineering, University of Kansas, Lawrence, Kansas, April 1985.
- Chang, R. C. and Muirhead, V. U., "Investigation of Dynamic Ground Effect," NASA CP-2462, Proceedings of the 1985 NASA Ground Effects Workshop.

- Chang, R. C. and Muirhead, V. U., "Effect of Sink Rate on Ground Effect of Low-Aspect-Ratio Wings," *Journal of Aircraft*, Vol. 24, March 1987, pp. 176-180.
- Chen, Y.-S. and Schweikhard, W. G., "Dynamic Ground Effects on a Two-Dimensional Flat Plate," *Journal of Aircraft*, Vol. 22, July 1985, pp. 638-640.
- Choliasmeons, C. J., "An Experimental Investigation and Theoretical Analysis of the Ground Effect on the Lift of a Wing with and without Boundary Layer Control," M. S. Thesis, University of Kansas, Lawrence, Kansas, May 1962.
- Elzebda, J. M., "Two-Degree-of-Freedom Subsonic Wing Rock and Nonlinear Aerodynamic Interference," Ph. D. Dissertation, Department of Engineering Science and Mechanics, Virginia Polytechnic Institute State University, Blacksburg, Virginia, Dec. 1986.
- Er-El, J. and Weihs, D., "Ground Effect on Slender Wings at Moderate and High Angle of Attack," *Journal of Aircraft*, Vol. 23, May 1986, pp. 357-358.
- Etkin, B., *Dynamics of Flight-Stability and Control*, John Wiley and Sons, N. Y., N. Y., Second Edition, 1982.
- Fink, M. P. and Lastinger, J. L., "Aerodynamic Characteristics of Low-Aspect-Ratio Wings in Close Proximity to the Ground," NASA TN D-926, July 1961.
- Fox, C. H., Jr., "Prediction of Lift and Drag for Slender Sharp-Edge Delta Wings in Ground Proximity," NASA TN D-4891, 1969.
- Fox, C. H., Jr., "An Analytic Method for Predicting the Lift and Drag for Slender Sharp-Edge Delta Wings in Ground Proximity," M. S. Thesis, Virginia Polytechnic Institute, Blacksburg, Virginia, March 1969.
- Gersten, k., "Calculation of the Aerodynamic Characteristics of Wings of Finite Span Near the Ground," R.A.E, Library Translation No. 1054, Dec. 1963.
- Gratzer, L. B. and Mahal, A. S., "Ground Effects in STOL Operation," *Journal of Aircraft*, Vol. 9, March 1972, pp. 236-242.
- Green, A. E., "The Forces Acting on a Circular-Arc Aerofoil in a Stream Bounded by a Plane Wall," *Proceedings London Mathematical Society*, Vol. 46, 1940, pp. 19-54.
- Green, A. E., "The Two-Dimensional Aerofoil in a Bounded Stream," *Quarterly Journal of Mathematics*, Vol. 18, 1947, pp. 167-177.
- Havelock, T. H., "The Lift and Moment on a Flat Plate in a Stream of Finite Width," *Proceedings of the Royal Society of London, Series A*, 166, 1938, pp. 178-196.
- Karamcheti, k., *Principles of Ideal-Fluid Aerodynamics*, Robert E. Krieger Publishing Company, Malabar, Florida, 1980.
- Katz, J., "Calculation of the Aerodynamic Forces on Automotive Lifting Surfaces," *Journal of Fluids Engineering*, Vol. 107, Dec. 1985, pp. 438-443.
- Katz, J. and Levin, D., "Measurements of Ground Effect for Delta Wings," *Journal of Aircraft*, Vol. 21, June 1984, pp. 441-443.
- Kemp, W. B., Jr., Lockwood, V. E., and Philips, W. P., "Ground Effects Related to Landing of Airplanes with Low-Aspect-Ratio Wings," NASA TN D-3583, 1966.

- Kobayakawa, M. and Maeda, H., "Gust Response of a Wing Near the Ground Through the Lifting-Surface Theory," *Journal of Aircraft*, Vol. 15, Aug. 1978, pp. 520-525.
- Kohlman, D. L. and Glett, C., "A Theoretical Method of Determining the Ground Effect on Lift and Pitching Moment for Wings of Arbitrary Planform," Boeing Document D3-1861, Oct. 1958.
- Konstadinopoulos, P., "A Vortex-Lattice Method for General Unsteady Subsonic Aerodynamics," M. S. Thesis, Department of Engineering Science and Mechanics, Virginia Polytechnic Institute and State University, Blacksburg, Virginia, July 1981.
- Konstadinopoulos, P., "Numerical Simulation of the Subsonic Wing-Rock Phenomenon," Ph.D. Dissertation, Department of Engineering Science and Mechanics, Virginia Polytechnic Institute and State University, Blacksburg, Virginia, March 1984.
- Konstadinopoulos, P., Thrasher, D. F., Mook, D. T., Nayfeh, A. H., and Watson, L., "A Vortex-Lattice for General Unsteady Aerodynamics," *Journal of Aircraft*, Vol. 22, Jan. 1985, pp. 43-49.
- Licher, R. M., "Increase in Lift for Two- and Three-Dimensional Wings Near the Ground," Douglas Aircraft, Santa Monica Division, Report No. SM-22615, Oct. 1956.
- Maskew, B., "On the Influence of Camber and Non-Planar Vortex Wake on Aerofoil Characteristics in Ground Effect," ARC Current Paper 1264, 1971.
- McRuer, D., Ashkenas, I. and Graham, D., *Aircraft Dynamics and Automatic Control*, Princeton University Press, Princeton, New Jersey, 1973.
- Mracek, C. P., "A Vortex-Panel Method for Potential Flows with Applications to Dynamics and Control," Ph.D. Dissertation, Department of Engineering Science and Mechanics, Virginia Polytechnic Institute and State University, Blacksburg, Virginia, August 1988.
- Nuhait, A. O. and Mook, D. T., "Numerical Simulation of wings in Steady and Unsteady Ground Effects," AIAA Paper No. 88-2546, June 1988.
- Palm, W. J., III, "Modeling, Analysis and Control of Dynamic Systems," John Wiley and Sons, New York, New York, 1983.
- Pistolesi, E., "Ground Effect-Theory and Practice," NACA TM 828, 1935.
- Plotkin, A. and Kennel, C. G., "Thickness-Induced Lift on a Thin Airfoil in Ground Effect," *AIAA Journal*, Vol. 9, 1981, pp.1484-1486.
- Reid, E. G., "A Full-Scale Investigation of Ground Effect," NACA TN 265, 1927.
- Rolls, L. S. and Koenig, D. G., "Flight-Measured Ground Effect on a Low-Aspect-Ratio Ogee Wing Including a Comparison with Wind-Tunnel Results," NASA TND-3431, 1966.
- Rosenhead, L., "The Lift on a Flat Plate Between Parallel Walls," *Proceedings of the Royal Society of London, Series A132*, 1931, pp. 127-152.
- Saunders, G. H., "Aerodynamic Characteristics of Wings in Ground Proximity," M. S. Thesis, Massachusetts Institute of Technology, Cambridge, Massachusetts, 1963.
- Saunders, G. H., "Aerodynamic Characteristics of Wings in Ground Proximity," *Canadian Aeronautics and Space Journal*, 1965, pp. 185-192.

- Schlichting, H. and Truckenbrodt, E., *Aerodynamics of the Airplane*, McGraw-Hill International Book Company, 1979.
- Smetana, F. O., *Computer Assisted Analysis of Aircraft Performance Stability and Control*, McGraw-Hill Book Company, New York, New York, 1984.
- Steven, V. C., "The Ground Effect of a Power-Lift STOL Aircraft During Landing Approach," NASA CP-2462, Proceedings of the 1985 NASA Ground Effect Workshop.
- Tan, C. H. and Plotkin, A., "Lifting-Line Solution for Symmetrical Thin Wing in Ground Effect," AIAA Journal, Vol. 24, 1985, pp. 1493-1494.
- Tani, I., "On the Effect of the Ground upon the Lift of a Monoplane Wing," The Journal the Aeron. Res. Inst., Tokyo Imperial Univ., Report No. 96, Aug. 1932. (As reported in Pistolesi (1935)).
- Tani, I., Taims, M., and Simidu, S., "The Effect of Ground on the Aerodynamic Characteristics of Monoplane Wing," Report No. 156 (Vol. XIII, 2), Aero. Res. Inst., Tokyo Imperial Univ., Sept. 1937. (As reported in Wetmore and Turner (1940)).
- Tani, I., Itokawa, H., and Taims, M., "Further Studies of the Ground Effect on the Aerodynamic Characteristics of an Airplane with Special Reference to Tail Moment," Report No. 158 (Vol. XIII, 4), Aero. Res. Inst., Tokyo Imperial Univ., Nov. 1937. (As reported in Wetmore and Turner (1940)).
- Thomas, F., "Aerodynamic Properties of Sweep-back and Delta Wings Near the Ground," R.A.E. Library Translation No. 882, March 1960.
- Tomotika, S., Hasimoto, Z., and Urano, K., "The Forces Acting on Aerofoil of Approximate Joukowski Type in a Stream Bounded by a Plane Wall," Quart. Journ. Mech. and Applied Math., Vol. 4, 1951a, pp. 289-307.
- Tomotika, S., Nagamiya, T., and Takenouti, Y., "The Lift on a Flat Plate Placed Near a Plane Wall, with Special Reference to the Effect of the Ground Upon the Lift of a Monoplane Aerofoil," Aeron. Res. Inst., Tokyo Imperial Univ., Report NO. 97, Aug. 1933. (As reported in Pistolesi (1935)).
- Tomotika, S., Tamada, K., and Umemoto, H., "The Lift and Moment Acting on a Circular-Arc Aerofoil in a Stream Bounded by a Plane Wall," Quarterly Journal of Mechanics and Applied mathematics, Vol. 4, 1951b, pp. 1-22.
- Tonnies, E., "Effect of the Ground on an Airplane Flying Close to it," NACA TM 674, 1932.
- Tuck, E. O., "Hydrodynamic Problems of Ships in Restricted Waters," In Annual Review of Fluid Mechanics, (ed. Van Dyke, M.), Vol. 10, 1978, pp. 33-44.
- Vinh, L.-S., Edwards, J. W., Seidel, D. A. and Batina, J. T., "Transonic Stability and Control of Aircraft Using CFD Methods," AIAA Paper No. 88-4374, August 1988.
- Wetmore, J. W. and Turner, L. I., Jr., "Determination of Ground Effect from Tests of a Glider in Towed Flight," NACA Report No. 645, 1940.
- Wentz, W. H., "Wind-Tunnel Investigations of Vortex Breakdown on Slender Sharp-Edge Wing," Ph. D. Dissertation, University of Kansas, 1968.
- Wieselsberger, C., "Wing Resistance Near the Ground," NACA TM 77, 1922.

Appendix A

Orientation of the Lifting Surface

The 3-2-1 Euler set of rotations is used to describe the orientation of the B-F axes relative to those of the G-F frame. The wing is imagined first to be oriented so that its axes (the B-F axes) are parallel to OXYZ. The wing is in the position $Ax_1y_1z_1$, as shown in figure 3 (taken from Etkin, 1982). As a result, the unit vectors along these axes are related, to those in the G-F reference frame by the following:

$$\vec{i}_1 = \vec{I}$$

$$\vec{j}_1 = \vec{J}$$

$$\vec{k}_1 = \vec{K}$$

Or in matrix form,

$$\begin{bmatrix} \vec{i}_1 \\ \vec{j}_1 \\ \vec{k}_1 \end{bmatrix} = [I] \begin{bmatrix} \vec{I} \\ \vec{J} \\ \vec{K} \end{bmatrix} \quad (\text{A.1})$$

where

$$[I] = \begin{bmatrix} 1 & 0 & 0 \\ 0 & 1 & 0 \\ 0 & 0 & 1 \end{bmatrix}$$

Then, a rotation ψ about Az_1 carries the axes to $Ax_2y_2z_2$, as shown in figure A.1. The base vectors along the $Ax_2y_2z_2$ and $Ax_1y_1z_1$ axes are related by the following:

$$\vec{i}_2 = \cos \psi \vec{i}_1 + \sin \psi \vec{j}_1$$

$$\vec{j}_2 = -\sin \psi \vec{i}_1 + \cos \psi \vec{j}_1$$

$$\vec{k}_2 = \vec{k}_1$$

Or in matrix form,

$$\begin{bmatrix} \vec{i}_2 \\ \vec{j}_2 \\ \vec{k}_2 \end{bmatrix} = [R_3(\psi)] \begin{bmatrix} \vec{i}_1 \\ \vec{j}_1 \\ \vec{k}_1 \end{bmatrix} \quad (\text{A.2})$$

where

$$[R_3(\psi)] = \begin{bmatrix} c\psi & s\psi & 0 \\ -s\psi & c\psi & 0 \\ 0 & 0 & 1 \end{bmatrix}$$

in which c and s denote the cosine and sine functions, respectively.

Then, a rotation θ about Ay_2 brings the axes to $Ax_3y_3z_3$, as shown in figure A.1. The unit vectors along the $Ax_3y_3z_3$ and $Ax_2y_2z_2$ axes are related by the following:

$$\vec{i}_3 = \cos \theta \vec{i}_2 - \sin \theta \vec{k}_2$$

$$\vec{j}_3 = \vec{j}_2$$

$$\vec{k}_3 = \sin \theta \vec{i}_2 + \cos \theta \vec{k}_2$$

Or in matrix form,

$$\begin{bmatrix} \vec{i}_3 \\ \vec{j}_3 \\ \vec{k}_3 \end{bmatrix} = [R_2(\theta)] \begin{bmatrix} \vec{i}_2 \\ \vec{j}_2 \\ \vec{k}_2 \end{bmatrix} \quad (\text{A.3})$$

where

$$[R_2(\theta)] = \begin{bmatrix} c\theta & 0 & -s\theta \\ 0 & 1 & 0 \\ s\theta & 0 & c\theta \end{bmatrix}$$

Finally, a rotation ϕ about Ax_3 , brings the axes to their final position $Axyz$, as shown in figure A.1. The base vectors along the $Axyz$ and $Ax_3y_3z_3$ axes are related by the following:

$$\vec{i} = \vec{i}_3$$

$$\vec{j} = \cos \phi \vec{j}_3 + \sin \phi \vec{k}_3$$

$$\vec{k} = -\sin \phi \vec{j}_3 + \cos \phi \vec{k}_3$$

Or in matrix form,

$$\begin{bmatrix} \vec{i} \\ \vec{j} \\ \vec{k} \end{bmatrix} = [R_1(\phi)] \begin{bmatrix} \vec{i}_3 \\ \vec{j}_3 \\ \vec{k}_3 \end{bmatrix} \quad (\text{A.4})$$

where

$$[R_1(\phi)] = \begin{bmatrix} 1 & 0 & 0 \\ 0 & c\phi & s\phi \\ 0 & -s\phi & c\phi \end{bmatrix}$$

Combining equations (A.1) to (A.4) yields the following result

$$\begin{bmatrix} \vec{i} \\ \vec{j} \\ \vec{k} \end{bmatrix} = [I(\phi)][R_3(\phi)][R_2(\phi)][R_1(\phi)] \begin{bmatrix} \vec{I} \\ \vec{J} \\ \vec{K} \end{bmatrix}$$

which reduces to

$$\begin{bmatrix} \vec{i} \\ \vec{j} \\ \vec{k} \end{bmatrix} = [R] \begin{bmatrix} \vec{I} \\ \vec{J} \\ \vec{K} \end{bmatrix} \quad (\text{A.5})$$

where

$$[R] = \begin{bmatrix} c\theta c\psi & c\theta s\psi & -s\theta \\ s\phi s\theta c\psi - c\phi s\psi & s\phi s\theta s\psi + c\phi c\psi & s\phi c\theta \\ c\phi s\theta c\psi + s\phi s\psi & c\phi s\theta s\psi - s\phi c\psi & c\phi c\theta \end{bmatrix}$$

and in which c and s denote the cosine and sine functions, respectively. Equation (A.5) expresses the unit vectors along the B-F axes in terms of those along the G-F axes. In order to express the unit vectors along the G-F axes in terms of those along the B-F axes, Equation (A.5) is inverted to yield

$$\begin{bmatrix} \vec{i} \\ \vec{j} \\ \vec{k} \end{bmatrix} = [R]^{-1} \begin{bmatrix} \vec{i} \\ \vec{j} \\ \vec{k} \end{bmatrix} \quad (\text{A.6})$$

Because $[R]$ is an orthonormal transformation, its inverse, $[R]^{-1}$, is equal to its transpose, $[R]^T$. Hence, equation (A.5) becomes simply

$$\begin{bmatrix} \vec{i} \\ \vec{j} \\ \vec{k} \end{bmatrix} = [R]^T \begin{bmatrix} \vec{i} \\ \vec{j} \\ \vec{k} \end{bmatrix} \quad (\text{A.7})$$

The angular velocity, $\vec{\omega}$, is expressed in terms of the derivatives of the Euler angles as follows:

$$\begin{aligned} \vec{\omega} &= \omega_x \vec{i} + \omega_y \vec{j} + \omega_z \vec{k} \\ &= \dot{\psi} \vec{k}_1 + \dot{\theta} \vec{j}_2 + \dot{\phi} \vec{i}_3 \end{aligned} \quad (\text{A.8})$$

From equation (A.2)

$$\vec{k}_1 = \vec{k}_2 \quad (\text{A.9})$$

And from equation (A.3)

$$\vec{k}_2 = -\sin \theta \vec{i}_3 + \cos \theta \vec{k}_3 \quad (\text{A.10})$$

$$\vec{j}_2 = \vec{j}_3 \quad (\text{A.11})$$

And from equation (A.4)

$$\vec{i}_3 = \vec{i} \quad (\text{A.12})$$

$$\vec{j}_3 = \cos \phi \vec{j} - \sin \phi \vec{k} \quad (\text{A.13})$$

$$\vec{k}_3 = \sin \phi \vec{j} + \cos \phi \vec{k} \quad (\text{A.14})$$

Now equations (A.9) to (A.14) yield

$$\vec{i}_3 = \vec{i} \quad (\text{A.15})$$

$$\vec{j}_2 = \cos \phi \vec{j} - \sin \phi \vec{k} \quad (\text{A.16})$$

$$\vec{k}_1 = -\sin \theta \vec{i} + \cos \theta \sin \phi \vec{j} + \cos \theta \cos \phi \vec{k} \quad (\text{A.17})$$

Equations (A.15) to (A.17) are substituted into equation (A.8) to yield:

$$\vec{\omega} = [C] \begin{bmatrix} \dot{\phi} \\ \dot{\theta} \\ \dot{\psi} \end{bmatrix} \quad (\text{A.18})$$

where

$$[C] = \begin{bmatrix} 1 & 0 & -s\theta \\ 0 & c\phi & s\phi c\theta \\ 0 & -s\phi & c\phi c\theta \end{bmatrix}$$

Equation (A.18) expresses the angular velocity in terms of the Euler angles and their derivatives. In order to express the derivative of the Euler angles in terms of the angular velocity, equation (A.18) is inverted as follow

$$\begin{bmatrix} \dot{\phi} \\ \dot{\theta} \\ \dot{\psi} \end{bmatrix} = [C]^{-1} \begin{bmatrix} \omega_x \\ \omega_y \\ \omega_z \end{bmatrix} \quad (\text{A.19})$$

where $[C]^{-1}$ is the inverse of $[C]$. It is derived using the Gauss-Jordan method as follow

$$[C | I] = \left[\begin{array}{ccc|ccc} 1 & 0 & -s\theta & 1 & 0 & 0 \\ 0 & c\phi & s\phi c\theta & 0 & 1 & 0 \\ 0 & -s\phi & c\phi c\theta & 0 & 0 & 1 \end{array} \right] \rightarrow$$

Multiplying the second row by $\frac{s\phi}{c\phi}$ then adding it to the third row yields the following:

$$\left[\begin{array}{ccc|ccc} 1 & 0 & -s\theta & 1 & 0 & 0 \\ 0 & c\phi & s\phi c\theta & 0 & 1 & 0 \\ 0 & 0 & \frac{c\theta}{c\phi} & 0 & \frac{s\phi}{c\phi} & 1 \end{array} \right] \rightarrow$$

Multiplying the second row by $\frac{1}{c\phi}$ yields the following:

$$\left[\begin{array}{ccc|ccc} 1 & 0 & -s\theta & 1 & 0 & 0 \\ 0 & 1 & \frac{s\phi c\theta}{c\phi} & 0 & \frac{1}{c\phi} & 0 \\ 0 & 0 & \frac{c\theta}{c\phi} & 0 & \frac{s\phi}{c\phi} & 1 \end{array} \right] \rightarrow$$

Multiplying the third row by $-s\phi$ then adding it to the second row yields the following:

$$\left[\begin{array}{ccc|ccc} 1 & 0 & -s\theta & 1 & 0 & 0 \\ 0 & 1 & 0 & 0 & \frac{1-s^2\phi}{c\phi} & -s\phi \\ 0 & 0 & \frac{c\theta}{c\phi} & 0 & \frac{s\phi}{c\phi} & 1 \end{array} \right] \rightarrow$$

Multiplying the third row by $\frac{c\phi}{c\theta}$ yields the following:

$$\left[\begin{array}{ccc|ccc} 1 & 0 & -s\theta & 1 & 0 & 0 \\ 0 & 1 & 0 & 0 & c\phi & -s\phi \\ 0 & 0 & 1 & 0 & \frac{s\phi}{c\theta} & \frac{c\phi}{c\theta} \end{array} \right] \rightarrow$$

Multiplying the third row by $s\theta$ then adding it to the first row yields the following:

$$\left[\begin{array}{ccc|ccc} 1 & 0 & 0 & 1 & \frac{s\phi s\theta}{c\theta} & \frac{c\phi s\theta}{c\theta} \\ 0 & 1 & 0 & 0 & c\phi & -s\phi \\ 0 & 0 & 1 & 0 & \frac{s\phi}{c\theta} & \frac{c\phi}{c\theta} \end{array} \right] = [I | C^{-1}]$$

Therefore, the inverse of the $[C]$ matrix is

$$[C]^{-1} = \begin{bmatrix} 1 & \frac{s\phi s\theta}{c\theta} & \frac{c\phi s\theta}{c\theta} \\ 0 & c\phi & -s\phi \\ 0 & \frac{s\phi}{c\theta} & \frac{c\phi}{c\theta} \end{bmatrix}$$

Appendix B

Velocity Induced by a Straight Vortex Segment

The subroutine used to compute the velocity induced by a straight vortex segment is presented next.

```

SUBROUTINE VEL(X1,Y1,Z1,X2,Y2,Z2,XP,YP,ZP,VX,VY,VZ,CUTOFF)
IMPLICIT REAL*8(A,H,O-Z), INTEGER(I-N)
C***
C    == LETS DEFINE OMEGA
C***
OMX = X2 - X1
OMY = Y2 - Y1
OMZ = Z2 - Z1
C***
C    == COMPUTE MAGNITUDE OF OMEGA TO THE FOURTH POWER.
C    == THEN MULTIPLY BY CUTOFF
C***
OMMAG2 = OMX*OMX + OMY*OMY + OMZ*OMZ
OMMAG4 = OMMAG2*OMMAG2
C    = CUTOFF*OMMAG4
C***
C    == THE CUTOFF WAS SQUARED ONCE AT THE BEGINNING OF COMPUTATION
C    == IN ORDER TO REDUCE THE EXECUTION TIME
c***
C    == DEFINE R1
C***
R1X = XP - X1
R1Y = YP - Y1
R1Z = ZP - Z1
C***
C    == DEFINE R2
C***
R2X = XP - X2
R2Y = YP - Y2
R2Z = ZP - Z2
C***
```

```

      OMYR1Z = OMY*R1Z
      OMZR1Y = OMZ*R1Y
C***
      OMZR1X = OMZ*R1X
      OMXR1Z = OMX*R1Z
C***
      OMXR1Y = OMX*R1Y
      OMYR1X = OMY*R1X
C***
      OMXR1X = OMX*R1X
      OMYR1Y = OMY*R1Y
      OMZR1Z = OMZ*R1Z
C***
      OMXR2X = OMX*R2X
      OMYR2Y = OMY*R2Y
      OMZR2Z = OMZ*R2Z
C***
      R1X2 = R1X*R1X
      R1Y2 = R1Y*R1Y
      R1Z2 = R1Z*R1Z
C***
      R2X2 = R2X*R2X
      R2Y2 = R2Y*R2Y
      R2Z2 = R2Z*R2Z
C***
C      == DEFINE : (VECTOR F) = (VECTOR OMEGA)CROSS(VECTOR R1)
C***
      FX = OMYR1Z - OMZR1Y
      FY = OMZR1X - OMXR1Z
      FZ = OMXR1Y - OMYR1X
C***
      FX2 = FX*FX
      FY2 = FY*FY
      FZ2 = FZ*FZ
C***
C      == COMPUTE THE SQUARE MAGNITUDE OF ( VECTOR F )
C***
      FMAG2 = FX2 + FY2 + FZ2
C***
C      == CHECK IF FMAG2 IS TOO SMALL
C***
      IF( FMAG2 .GE. C )THEN
C***
C      == COMPUTE THE MAGNITUDE OF BOTH VECTORS R1 AND R2
C***
      R1MAG = SQRT( R1X2 + R1Y2 + R1Z2 )
      R2MAG = SQRT( R2X2 + R2Y2 + R2Z2 )
C***
C      == DEFINE G1= ( OMEGA VECTOR )*( VECTOR R1 )/R1MAG

```

```

C      == AND   G2= ( OMEGA VECTOR )*( VECTOR R2 )/R2MAG
C****
      G1 = ( OMXR1X + OMYR1Y + OMZR1Z )/R1MAG
      G2 = ( OMXR2X + OMYR2Y + OMZR2Z )/R2MAG
C****
C      == DEFINE FACTOR
C****
      FAC = ( G1 - G2 )/FMAG2
C****
C      == COMPUTE VELOCITY
C****
      VX = FAC*FX
      VY = FAC*FY
      VZ = FAC*FZ
C****
      ELSE
C****
      VX = 0.D0
      VY = 0.D0
      VZ = 0.D0
C****
      ENDIF
C****
C      THIS SECTION COMPUTES THE CONTRIBUTION FROM THE PORT SIDE FOR
C      SYMMETRIC FLOW
C****
      Y1M =- Y1
      Y2M =- Y2
C****
      OMXM = - OMX
      OMYM =  OMY
      OMZM = - OMZ
C****
      R1XM = XP - X2
      R1YM = YP - Y2M
      R1ZM = ZP - Z2
C****
      R2XM = XP - X1
      R2YM = YP - Y1M
      R2ZM = ZP - Z1
C****
      YMR1ZM =  OMYM*R1ZM
      ZMR1YM =  OMZM*R1YM
C****
      ZMR1XM =  OMZM*R1XM
      XMR1ZM =  OMXM*R1ZM
C****
      XMR1YM =  OMXM*R1YM
      YMR1XM =  OMYM*R1XM
C****

```

```

XMR1XM = OMXM*R1XM
YMR1YM = OMYM*R1YM
ZMR1ZM = OMZM*R1ZM
C***
XMR2XM = OMXM*R2XM
YMR2YM = OMYM*R2YM
ZMR2ZM = OMZM*R2ZM
C***
R1XM2 = R1XM*R1XM
R1YM2 = R1YM*R1YM
R1ZM2 = R1ZM*R1ZM
C***
R2XM2 = R2XM*R2XM
R2YM2 = R2YM*R2YM
R2ZM2 = R2ZM*R2ZM
C***
FXM = YMR1ZM - ZMR1YM
FYM = ZMR1XM - XMR1ZM
FZM = XMR1YM - YMR1XM
FXM2 = FXM*FXM
FYM2 = FYM*FYM
FZM2 = FZM*FZM
C***
FMMAG2 = FXM2 + FYM2 + FZM2
C***
IF( FMMAG2 .GE. C )THEN
C***
R1MMAG = DSQRT( R1XM2 + R1YM2 + R1ZM2 )
R2MMAG = DSQRT( R2XM2 + R2YM2 + R2ZM2 )
C***
G1M = ( XMR1XM + YMR1YM + ZMR1ZM)/R1MMAG
G2M = ( XMR2XM + YMR2YM + ZMR2ZM )/R2MMAG
C***
FACM = ( G1M - G2M )/FMMAG2
C***
VX = VX + FACM*FXM
VY = VY + FACM*FYM
VZ = VZ + FACM*FZM
C***
ELSE
C***
ENDIF
C***
C RETURN
C == THIS SECTION COMPUTES THE GROUND EFFECT
C***
Z1M = -Z1
Z2M = -Z2
C***

```

```

OMZM = -OMZ
C***
R1ZM = ZP - Z1M
R2ZM = ZP - Z2M
C***
YMR1ZM = OMY*R1ZM
ZMR1Y = - OMZR1Y
C***
ZMR1X = - OMZR1X
XMR1ZM = OMX*R1ZM
C***
ZMR1ZM = OMZM*R1ZM
ZMR2ZM = OMZM*R2ZM
C***
R1ZM2 = R1ZM*R1ZM
R2ZM2 = R2ZM*R2ZM
C***
FXM = YMR1ZM - ZMR1Y
FYM = ZMR1X - XMR1ZM
FXM2 = FXM*FXM
FYM2 = FYM*FYM
C***
FMMAG2 = FXM2 + FYM2 + FZ2
C***
IF( FMMAG2 .GE. C )THEN
C***
R1MMAG = SQRT( R1X2 + R1Y2 + R1ZM2 )
R2MMAG = SQRT( R2X2 + R2Y2 + R2ZM2 )
C***
G1M = ( OMXR1X + OMYR1Y + ZMR1ZM )/R1MMAG
G2M = ( OMXR2X + OMYR2Y + ZMR2ZM )/R2MMAG
C***
FACM = ( G1M - G2M )/FMMAG2
C***
VX = VX - FACM*FXM
VY = VY - FACM*FYM
VZ = VZ - FACM*FZ
C***
ELSE
C***
ENDIF
C***
C THIS SECTION COMPUTES THE CONTRIBUTION FROM THE PORT SIDE FOR
C SYMMETRIC FLOW IN GROUND EFFECT
C***
OMZM = OMZ
C***
R1ZM = ZP - Z2M
R2ZM = ZP - Z1M
C***

```

```

      YMR1ZM = OMYM*R1ZM
      ZMR1YM =- ZMR1YM
C***
      ZMR1XM =- ZMR1XM
      XMR1ZM = OMXM*R1ZM
C***
      ZMR1ZM = OMZM*R1ZM
      ZMR2ZM = OMZM*R2ZM
C***
      R1ZM2 = R1ZM*R1ZM
      R2ZM2 = R2ZM*R2ZM
C***
      FXM = YMR1ZM - ZMR1YM
      FYM = ZMR1XM - XMR1ZM
      FXM2 = FXM*FXM
      FYM2 = FYM*FYM
C***
      FMMAG2 = FXM2 + FYM2 + FZM2
C***
      IF( FMMAG2 .GE. C )THEN
C***
      R1MMAG = DSQRT( R1XM2 + R1YM2 + R1ZM2 )
      R2MMAG = DSQRT( R2XM2 + R2YM2 + R2ZM2 )
C***
      G1M = ( XMR1XM + YMR1YM + ZMR1ZM )/R1MMAG
      G2M = ( XMR2XM + YMR2YM + ZMR2ZM )/R2MMAG
C***
      FACM = ( G1M - G2M )/FMMAG2
C***
      VX = VX - FACM*FXM
      VY = VY - FACM*FYM
      VZ = VZ - FACM*FZM
C***
      ELSE
      ENDIF
C***
C***
      RETURN
      END

```

**The vita has been removed from
the scanned document**